Universidad Carlos III de Madrid
www.uc3m.es

TESIS DOCTORAL

On the design of solar external receivers

Autor:

María de los Reyes Rodríguez Sánchez

Director/es:

Domingo Santana Santana

Carolina Marugan Cruz

Tutor:

Domingo Santana Santana

DEPARTAMENTO DE INGENIERÍA TÉRMICA Y DE FLUIDOS

Leganés, Septiembre 2,015

Universidad Carlos III de Madrid
www.uc3m.es

TESIS DOCTORAL

ON THE DESIGN OF SOLAR EXTERNAL RECEIVERS

Autor: ***María de los Reyes Rodríguez Sánchez***

Director/es: **Domingo Santana Santana**
Carolina Marugan Cruz

Firma del Tribunal Calificador:

Firma

Presidente:

Vocal:

Secretario:

Calificación:

Leganés, 29 de Septiembre de 2015

Tesis Doctoral

ON THE DESIGN OF SOLAR EXTERNAL RECEIVERS

Autor
María de los Reyes Rodríguez Sánchez

Director
Domingo Santana Santana
Co-directora
Carolina Marugán Cruz

DEPARTAMENTO DE INGENIERÍA TÉRMICA Y DE FLUIDOS

Leganés (Madrid), Septiembre 2015

Tesis doctoral

ON THE DESIGN OF SOLAR EXTERNAL RECEIVERS

Autor: María de los Reyes Rodríguez Sánchez

Director de Tesis: Domingo Santana Santana
Co-directora de Tesis: Carolina Marugán Cruz

Firma del Tribunal Calificador:

Firma

Presidente: D.

Secretario: D.

Vocal: D.

Calificación:

Leganés (Madrid), 29 de Septiembre de 2015

DEPARTAMENTO DE INGENIERÍA TÉRMICA Y DE FLUIDOS
Escuela Politécnica Superior

ON THE DESIGN OF SOLAR EXTERNAL RECEIVERS

Autor
María de los Reyes Rodríguez Sánchez

Director de Tesis
Domingo Santana Santana
Co-directora de Tesis
Carolina Marugán Cruz

Leganés (Madrid), Septiembre 2015

No te rindas, por favor no cedas,aunque
el frío queme, aunque el miedo muerda,
aunque el sol se esconda, y se calle el viento,
aún hay fuego en tu alma, aún hay vida
en tus sueños. Porque la vida es tuya y
tuyo también el deseo, porque cada día es
un comienzo nuevo, porque esta es la hora
y el mejor momento, porque no estás solo,
¡porque yo te quiero!

...

Mario Benedetti

En dos palabras puedo resumir cuanto
he aprendido acerca de la vida:
Sigue adelante.

...

Robert Frost

Abstract

Solar external receivers with molten salt as heat transfer fluid are the most critical subsystem of a Solar Power Tower (SPT). Receiver tubes work under extreme conditions due to the high incident solar flux and the potentially corrosive environments. These demanding conditions of operation usually produce the failure of the receiver by stress corrosion cracking. The unsteady solar flux and the large size of the heliostat field and the receiver make very complicated accurate measurement of the spatial heat flux on the receiver tubes. Hence, modelling accurately the solar flux onto the receiver and the heat transfer in the tubes is required.

This PhD thesis consists in the development and validation of several thermal models of external receivers to improve the estimation of the temperature distribution on the receiver tubes and the thermal efficiency. The application of the models has enabled to establish the guidelines for the accurate and safety design of the external receivers. In this thesis there are presented two simplified and two-dimensional models. The first model assumes homogeneous heat flux in the tubes, while the other assumes homogeneous temperature. The main characteristic of the models is that they consider circumferential and axial distribution of the temperature in the receiver tubes. In addition, they take into account the main heat exchange mechanisms, as well as the temperature dependence of the thermo-mechanical properties of tube materials and heat transfer fluid.

Firstly, the SPT operation modes and weakness were analysed. Subsequently, the viability of installing a system to reduce the parasitic energy consumption of the SPT was studied. This system, named Potential Energy Recovery System (PERS), recovers the potential energy from the downcomer of the receiver. The PERS was included in the models of two different actual SPT resulting in important energy savings in both plants.

The simplified models were validated with CFD simulations, other simplified models, and experimental data. Regarding the CFD, the accuracy of the results is similar, but the simplified models proposed here have a significant lower computational cost, which is a notable advantage for the pre-design of the receiver where many geometrical parameters must be analysed. Regarding experimental data, given the inlet temperature of the heat transfer fluid, the

direct normal irradiance, and an approximation of the aiming strategy of the heliostat field, the results obtained for the outlet temperature of the salt and the mass flow rate in the receiver are very close. Comparing with previous simplified models the thermal efficiency obtained is around 10% lower than in previous studies. The key of this difference is the thermal resistance for the heat transfer process related to the fluid and the tube material. It was also seen that the Biot number is large, and therefore the circumferential temperature must be taken into account for proper receiver efficiency estimation.

In addition, different receiver geometries were analysed to find the optimum receiver design. It was determined that the most restrictive variables are the mechanical stresses and the film temperature. Regarding the receiver flow path, the best option is to implement two symmetrical paths that in the north hemisphere go from north - to - south of the receiver assuring the peak flux far from southern panels.

Finally, the feasibility of employing SPT that uses supercritical or ultra-supercritical power blocks was analysed using the developed thermal models. However, the increase of the power block efficiency implies higher heat losses in the receiver. Therefore, the new generation of SPT will be only advisable when the cost of materials and systems decrease considerably.

Resumen

Los receptores solares de sales fundidas son el subsistema más crítico de las centrales termosolares tipo torre. Estos receptores están sometidos a unas condiciones de trabajo extremas, destacando la gran concentración de flujo solar incidente y un ambiente de trabajo potencialmente corrosivo. Estas condiciones tan exigentes suelen producir roturas en el receptor por corrosión bajo tensión. Además debido a la gran inestabilidad del flujo solar y a las grandes dimensiones tanto del receptor como de los heliostatos es muy complicado determinar de forma precisa la distribución espacial del flujo de calor sobre los tubos del receptor, resultando imprescindible el modelado del flujo de calor sobre el receptor y la transferencia de calor en sus tubos.

Esta tesis doctoral se basa en el desarrollo y validación de varios modelos térmicos de receptores centrales que intentan mejorar la estimación de la distribución de temperatura en los tubos del receptor y su eficiencia térmica global. Mediante la aplicación de estos modelos se han establecido las pautas para el diceño de receptores que aseguran un funcionamiento fiable del mismo. Los modelos térmicos dessarrollados son simplificados y bidimensionales, uno de ellos asume flujo de calor constante en los tubos y el otro temperatura constante. La característica principal de estos modelos bidimensionales es que tienen en cuenta las variaciones circunferenciales y axiales de temperatura en los tubos del receptor. Además, estos modelos aunque sencillos y rápidos tienen en cuenta los principales mecanismos de intercambio de calor, y que las propiedades termomecánicas de materiales y del fluido caloportador dependen de la temperatura.

En primer lugar se estudió el funcionamiento de las centrales solares de torre, analizando sus fortalezas y debilidades. Surge así la idea de evaluar la viabilidad de implantar un sistema que reduzca su auto-consumo energético. Este sistema, denominado PERS, consiste en recuperar la energía potencial del fluido caliente que baja del receptor a los tanques de almacenamiento. El PERS se ha incluido en el modelo de dos centrales solares de torre diferentes, y en ambos casos se han encontrado unos importantes ahorros energéticos.

Los modelos simplificados desarrollados han sido validados con CFD, otros modelos simplificados y datos experimentales. Con respecto a las simulaciones CFD los resultados obtenidos son del mismo orden pero con una notable reducción del coste computacional, lo que significa una ventaja notable para el

pre-diseño de los receptores centrales, donde son analizados numerosos parámetros geométricos. Comparando con los escasos datos experimentales publicados, conocidas la temperatura de entrada del fluido de trabajo, la irradiación solar directa y una aproximación de la estrategia de apuntamiento del campo de heliostatos, se han obtenido unos flujos másicos y unas temperaturas de salida del fluido muy similares a los experimentales. Para completar el estudio, se han comparado nuestros modelos con otros modelos simplificados de la bibliografía. En este caso la eficiencia térmica del receptor obtenida es alrededor de un 10% menor a los obtenidos previamente. La clave de esta diferencia es la resistencia térmica en el proceso de transferencia de calor, relacionada tanto con el fluido como con el material de los tubos. Además se ha visto que el número de Biot es elevado, y por lo tanto las variaciones circunferenciales de temperatura deben tenerse en cuenta para estimar la eficiencia térmica del receptor correctamente.

En esta tesis se han analizado diferentes geometrías del receptor bajo diversos modos de funcionamiento en orden de encontrar un diceño óptimo. Se ha determinado que las variables más restrictivas para el diseño del receptor son el estrés mecánico y la temperatura de película. En cuanto a los canales de flujo, en el hemisferio norte la mejor opción es implementar dos canales simétricos que circulen de norte a sur, asegurando que el pico de densidad solar se encuentre lejos de la zona de salida del receptor, lado sur.

Finalmente, la posibilidad de utilizar una nueva generación de centrales solares tipo torre que emplee bloques de potencia supercríticos y ultra-supercríticos ha sido analizada con el empleo de los modelos simplificados previamente desarrollados. Sin embargo, el aumento de eficiencia en el bloque de potencia implica mayores temperaturas y pérdidas de calor en el receptor. Por lo tanto, esta nueva generación de centrales de torre solo será recomendada cuando los precios de los materiales y de los sistemas supercríticos desciendan considerablemente.

Contents

List of Figures

List of Tables

CHAPTER
ONE

General introduction

Contents

1.1 Motivation

Solar power tower plants are one of the most promising renewable energy for electric generation. One of the main advantages of SPT systems is the large heat storage capability, which allows these systems to generate electric power with continuity and stability. Other interesting characteristic is the high level of power that is able to produce, up to 100 MWe.

In the recent years the first commercial plants with molten salt as heat transfer fluid have been built and in this moment numerous projects are under development. However, there is still a challenging issue with respect to central receivers. The main problem associated with the heat exchange in the

receiver is the high temperature gradient at the receiver surface and the transient thermal processes that may lead to local hot spots, and consequently, degradation or failure of the receiver. Therefore, the receiver temperature distribution must be carefully controlled. However, the scarcity of experimental data makes necessary to develop thermal models to understand the operation modes and optimize the receiver design.

In this regard the goal of this PhD thesis is to develop a thermal model of the external receivers capable of predict the thermal efficiency and the temperature distribution of the receiver. It is a simplified 2-D thermal model that takes into account the most important heat transfer mechanisms, the temperature dependence of the material and fluid properties, and also the circumferential and axial variations of the temperature along the tubes. In addition, it takes into account thermal, mechanical, and hydrodynamic limitations of the receiver.

The main advantage of the model presented in this dissertation is low computational cost with respect to CFD models, maintaining similar accuracy of the results. It allows to modify a huge quantity of parameters, to define the receiver geometry, with low computational cost and time.

1.2 Background

Environmental problems and limited fossil fuel resources require new sustainable electricity generation options. Concentrating solar power (CSP) technology is an important alternative for providing clean and renewable electricity generation in the present and future. CSP is similar to small-medium size conventional power plants (Pitz-Paal & Milow, 2005). However, CSP utilizes the heat of the sun, unrestricted and daily available energy source, that allows to reduce the greenhouse gas emissions in approximately 1 kg for each kW of electricity generated.

Besides CSP can be integrated with large thermal storage systems to store a part of the concentrated energy during the sunny days and to generate electricity in cloudy days or even at nights. CSP has also the possibility of hybridization with fossil fuels to make the plant increase its availability and to follow the energy demand the 24 hours of the day (Zhang & Cacères, 2013). The easy manage and the capacity to be adapted to the electric market demand makes CSP the most interesting technology among the renewable technologies and competitive with the fossil fuel power plants (Seia & SolarPACES, 2001).

Currently, there are four CSP technologies, which are parabolic trough tech-

nology (PTC), linear Fresnel collector (LFC), Stirling/dish systems (SDC), and solar tower power (SPT) also known as central receiver technology (eSolar *et al.*, 2008). The parabolic trough collector and the linear Fresnel collector are known as line focus technologies because they concentrate the sun radiation along the focal length of the collector; while the Stirling and the solar tower power technologies are namely point focus technologies because the concentrate the sun radiation on one point at the top of the tower or in the middle of the parabolic dish.

Line focus technologies concentrates the solar radiation about 100 times, reaching temperatures in the heat transfer fluid (HTF) of 400-550 °C (**?**). At this temperature interval the steam produced is at moderate quality. Point focus technologies concentrate the solar radiation about 1000 times, heating the HTF at 600-1000 °C, two times the temperature reached in line focus technique (Richter & Short, 2009). That difference makes point focus technique more efficient, due to reduce the land usage and the most effective cost per KWh, although line focus technologies are technically less difficult than point focus techniques, see Table 1.1

Table 1.1: Main characteristics of the different CSP technologies (Pitz-Paal & Milow, 2005; Pavlović & Pantić, 2012; Re, 2012; Ausra, 2014; Beerbaum & Weinrebe, 2000; Gil & Cabeza, 2010).

	Technology	Collector	Receiver							
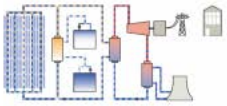	PTC	Parabolic trough	Linear receiver (tubes)							
			T[°C]				LEC [€/kWhe]			
			393				0.172			
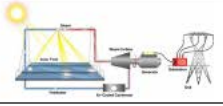	LFC	Parabolic trough	Linear receiver (tubes)							
			T[°C]				LEC [€/kWhe]			
			411				0.162			
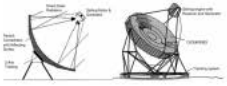	SDC	Parabolic dish	Cavity receiver with tube bundle							
			T[°C]				LEC [€/kWhe]			
			800				0.193			
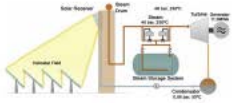	SPT	Heliostat field	External molten salt		Saturated steam receiver		Volumetric atmospheric air receiver		Pressurized air receiver	
			T[°C]	LEC	T[°C]	LEC	T[°C]	LEC	T[°C]	LEC
			565	0.155	250	0.169	750	0.179	1000	0.139

Among all solar technologies parabolic trough is the most technically and commercially proven (95.7% of the total operational CSP projects), allowing the lowest cost and low economic risk. However, there is a trend to employing other CSP technologies of larger scale; then for projects under development the solar power tower technology has reached the 71.43% compared to 28.57% for parabolic trough technology (Dhyia Aidroos & Saeed Obaid, 2015), reaching powers of 110 MWe and 17.5 hours of thermal energy storage, Atacama project (NREL, 2011). All of this motivates the study of solar power tower in this PhD thesis.

1.2.1 Heat transfer fluids

One of the most critical element for storing and transferring thermal energy in CSP is the heat transfer fluid. Since a large amount of HTF is required to operate a CSP plant, it is necessary to minimize the cost of the HTF and maximizing the plant efficiency. The wished characteristics of the HTF include: low melting point, high boiling point, thermal stability, low vapour pressure at high temperature, low corrosion of the materials that contain it, low viscosity, high thermal conductivity, high heat capacity for energy storage, and low cost Pacio & Wetzel (2013). Vignarooban & Kannan (2015) classified the principal HTFs in six main groups:

- **Air and other gases**: This heat transfer fluid can be obtain cost-free from the atmosphere, however it is not pure and can produce oxidation and depositions. It could reach very high temperatures although usually needs high pressure. It has very low dynamic viscosity having good flow properties inside the pipes. Nevertheless, air has low thermal conductivity that makes difficult the heating in the receiver, by the contrary it heat transfer to the steam is very efficient. SPT with air are being widely investigated, but it has a long way to go before reaching its maturity.

- **Water/steam**: It is used as both HTF and working fluid in the turbine, and then there is not necessary the evaporator train. The main problem is the scarcity of water in the regions where the plants are usually located. Its properties are well established and good for the heat exchange in the receiver, however the storage of the steam is complicated as has demonstrated the two hours of thermal storage of Khi Solar One of Abengoa (Abengoa, 2014). In addition, at high temperatures it is corrosive in contact with metal alloys and stainless steels.

- **Thermal oils**: These oils are thermally stable only up to 400 °C, then they cannot be used in high temperature and highly efficient solar thermal systems. Another issue is that are expensive, their price varies from 3 to 5 $/kg. As happens with the water they have good thermal properties for the heat exchange, but their heat capacities are low to be used as thermal energy storage. Different thermal oils are being investigated in order to achieve higher temperatures without decomposition of the oil.

- **Organics**: They present a good heat transfer performance, low viscosity, and long service life. They are particularly recommended for indirect liquid phase process heating at medium temperatures, due to they are not stable up to 400 °C.

- **Molten salt**: It has thermal stability at temperatures up to 600 °C. Also have properties comparable with the water at high temperature, including similar viscosity and low vapour pressure. Another advantage is their capability for thermal energy storage. However, nitrate salt production is restricted and its price is around 1$/kg. To reduce the price of this HTF the most employed salt is a binary mixture out of eutectic composed by 60wt% $NaNO_3$ and 40wt % KNO_3. The problem of this salt is the relative high melting point 223 °C, and their high corrosive nature to metal alloys at temperatures up to 650 °C. In addition, the molten salt is a liquid with high capillarity.

- **Liquid metals**: They have not been used in commercial applications, but they have several promising properties to be used as heat transport fluid due to the high thermal conductivity and their wide applicable temperature range. However,heat capacities of liquids metals are relatively low to be used as thermal energy storage media. Also, liquid metals are highly reactive fluid that make more difficult the storage system design to assure safe operation of the system (Hering & Wetzel, 2012). In addition, their price is relative high compared with molten-salt.

Although there are numerous advances in air receivers, they have not still been used for high power levels. Therefore, the molten salt is the heat transfer fluid studied in this dissertation.

1.2.2 Materials

Stainless steels and nickel based alloys are the typical materials of CSP tubes and tanks, and their stability in contact with the HTF is very important for the longevity of the CSP, then the combination material-HTF must be studied in detail. When those materials form part of the concentrator are subjected to extreme working conditions, their outer surface intercepts high solar flux radiation while their inner surface is in contact to HTF. Then, the stress corrosion cracking (SCC) problems due to fatigue and thermal stress must be considered. The most typical materials used in CSP are listed above.

- **Stainless steel 316**: it is the cheapest material, around 2.5-5 $/kg (Alibaba, 2015), and it was used in Solar Two project Pacheco (2002). Its thermal and mechanical properties are adequate. However, after approximately three years of operation, when the receiver was disassembled numerous problems due to the corrosion was seen in the receiver tubes.

- **Inconel alloy 625**: this material has been extensively used in the industry and has the best mechanical and thermal properties, but the high temperature vessel code ASME (2011) does not recommend to use this material at film temperatures higher than 600 °C. Its price rounds 20-25 $/kg (Alibaba, 2015).

- **Incoloy 800H**: it was used in Solar One project and in a Sandia salt receiver tests (Kolb, 2011). Bradshaw (1987) established with several test that the maximum film temperature of alloy 800H in 630 °C. However, the mechanical properties of Incoloy 800H are slightly worse than for alloy 625, and it is more expensive, around 30-60 $/kg (Alibaba, 2015).

- **Haynes 230**: it is promoted to become in an important candidate material for solar tower receivers, its properties are not as good than the Inconel 625 properties, but it can work at temperatures up to 650 °C thanks to the percentage of tungsten in its composition. McConohy & Kruizenga (2014) test the Haynes 230 at film temperature of 680 °C and they concluded that it could be used at this temperature despite the elevated corrosion rate. The main disadvantage of this material is the elevated cost, around 40-80 $/kg (Alibaba, 2015).

In addition, receiver tubes usually are coated with a high temperature paint that increases its efficiency. The standard is to use Pyromark 2500. It is

relatively inexpensive, easy to apply. Pyromark 2500 has a solar absoptance around 0.96 (Ho *et al.*, 2013). However, with a thermal emittance of 0.87 it suffers drom large thermal losses during high temperature operation. It also showed significant degradation at temperature higher than 700 °C when operated in atmospheric air causing a decline in receiver performance (Ho & Iverson, 2014).

1.3 Molten-salt solar power towers

Tower power technology is considered a more recent technology than parabolic trough. Molten salt solar receiver systems have been studied since 1976, and were first implemented in 1983 with Themis demonstration plant (Bezian, 1986), this plant of 2.5 MW produced electricity during three years. In 1996 after a failed steam solar power tower, Sandia National laboratories started to operate the demonstration plant Solar Two, a 10 MWe plant with 3 h of thermal storage capacity (Pacheco, 2002). In mid of 2005 SENER and CIEMAT joined forces to develop a receiver more efficient than Solar Two receiver, and in 2006 a prototype was tested in Plataforma solar de Almeria (Schiel & Geyer, 1988). Based on the last receiver design, Torresol Energy built in Spain the first commercial tower power plant in 2009. The plant is known as Solar Tres or Gemasolar and produces 19.9 MWe with 15 hours of storage (Torresol, 2010). The success of this plant stablished the SPT technology, and since then there are several large scale projects worldwide. For example, in October of 2013, SolarReserve started to build in Nevada the commercial project Crescent Dunes, which operated for first time in 2015 with 110 MWe power generation and 10 hours of storage (NREL, 2011). Currently, Atacama solar plant is under construction, it will be a 110 MWe power plant with 17.5 hours of thermal energy storage capacity. Molten salt technology represents nowadays the most cost-effective technology for stand-alone electricity generation, thanks to the elevated thermal energy storage capacity (Dhyia Aidroos & Saeed Obaid, 2015).

Molten-salt solar power tower use a field of distributed mirrors - heliostats - that individually track the sun and focus the sunlight on the top of a tower by concentrating the sunlight 600-1,000 times, they achieve temperatures up to 600 °C. The solar energy is absorbed by a working fluid and then used to generate steam to power a conventional turbine. The receiver system is the door for which the energy passes from the field collector to the thermal electric cycle, it represents therefore, the core of the SPT and its performance directly affects

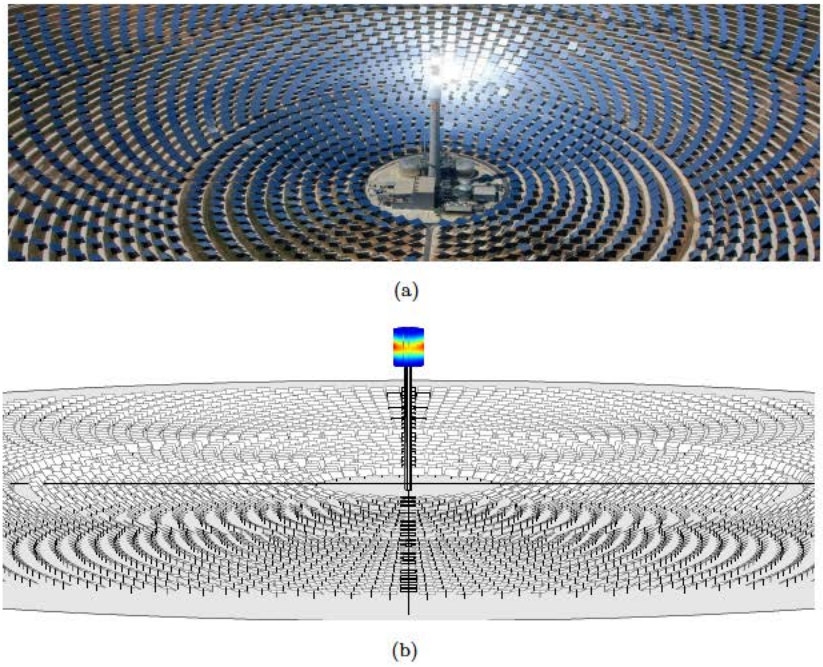

(a)

(b)

Figure 1.1: a) Aerial view of Gemasolar SPT (Sener, 2015). b) Simulation scheme of the same power plant.

to the plant production (Hefni & Soler, 2015). The three main subsystems of a solar power plant have been explained above.

A distinguishing feature of concentrating solar power among other renewable technologies is its ability to include thermal energy storage at the point of power generation to handle the intermittencies of solar availability. The thermal storage is not mandatory in the receiver plants, but also has been explained due to its importance in the dispachability of the plant and in the levelized cost of the energy.

1.3.1 Heliostat field

The heliostats are flat or slightly concave mirrors that follow the sun in a two axis tracking. In function of the arrangement of the heliostats with respect the receiver, there are two different heliostat field configurations. If the receiver is vertical plane or if it is enclosed in a cavity the heliostats must be located in

the north of the receiver, north field. However, if the receiver is cylindrical the heliostat field must be located around the tower, circular field.

The aim of these configurations, together with interlard between heliostat rows, is to reduce the blocking and shading effects of the heliostats in order to improve the optical efficiency and hence reduce the solar field cost. Although the operation of the heliostat field is simple, and does not represent significant problems the design of the heliostat field is critical. It represents around 45% of the total cost of the SPT (Price, 2003).

However, it cannot be studied alone, due to the receiver size and its limitations affect the heliostat calculations. Then receiver and heliostat fields must be studied togheter to maximize the outfit thermal efficiency and minimize the heliostat field costs.

For 2020 the SunShot goals are to reach the following technical targets of heliostat field subsystems (DOE, 2015).

- Cost < 75 \$/m2
- Optical error < 3 mrad
- Sustain wind speed > 85 mph
- Lifetime > 30 years

1.3.2 External receiver

The external central receiver is placed at the top of a tower, configured as a 360° cylindrical tubular receiver. The vertical thin-walled tubes are arranged in panels. Depending on the flow path configuration the molten salt can enter by one or two panels, using a combination of up-flow and down-flow panels.

The receiver is not extremely expensive compared with the total cost of the plant, around 17% (Singer *et al.*, 2014). However, is the most critical element due to the extreme working conditions. It receives high incident solar flux in the external face of the tubes while in the internal side there is a corrosive environment. Therefore, to assure the life of the receivers is one of the most important goal in the design of SPT. Figure 1.2 shows the Solar Two receiver after the three years of operation. It can be seen the high fatigue at which it was subjected.

The design of this kind of receiver is not easy due to the instability of the solar flux and the large size of heliostats and receiver make extremely difficult

Figure 1.2: Solar Two receiver after the three years of operation (DOE & Sandia, 1998).

to determine the spatial heat flux distribution on the receiver tubes. Hence, the exact control of the temperature distribution is even harder.

The target to fulfil for receiver subsystems proposed by SunShot and ASTRI are the following (DOE, 2015):

DOE (2015).

- Heat transfer fluid exit temperature from the receiver > 650 °C
- Thermal efficiency $> 90\%$
- Lifetime $>$ 10,000 cycles
- Cost < 150 \$/kW$_{th}$

1.3.3 Power block

The power block of this kind of plants is usually formed by a Rankine turbine. The cycle is very similar to traditional one. However, the boiler is substituted by an evaporator train. This evaporator has problems with the thermal stresses, especially in transient regime. In addition, the tubes which contain the molten salt have to be permanent controlled to avoid tube crack.

For power blocks the main goals to reach in 2020 are (DOE, 2015):

- High temperature power cycles
- Net cycle efficiency $> 50\%$

- Dry cooled
- Cost $<$ 1,200 \$/kWe

1.3.4 Thermal storage

SPT usually include a storage system formed by two tanks at the bottom of the tower. One of the tanks contains the cold salt (290 °C) that flows through the receiver, whereas the other tank collect the hot salts that flows from the receiver (565 °C).

Despite of the high corrosive ambient, the storage tanks usually are built of stainless steel to reduce cost. They have a large size due they have the feed pumps inside. Both tanks have to be insulated in order to avoid heat losses to the ambient. Inside of the tank usually there are mechanisms to avoid stratification of the salt.

Small storage capability of a SPT is to control the power block during small sun transitory periods. However, high storage capability pretends to reduce the levelized cost of the energy, and it is an economical function. Then, a large storage capability depends on the electricity price and on the country energy regulations. For example, in a market which buys every the renewable energy is convenient more time of storage, but in places in which the energy is only bought in peaks hours low storage capability is necessary.

The SunShot Initiative funds research and development on sensible, latent, and thermochemical energy storage to achieve the following technical targets of thermal energy storage subsystems (DOE, 2015):

- Improve heat transfer and thermal energy storage media
- Thermal energy storage cost $<$ 15\$/kWh$_{th}$
- Exergetic efficiency $>$ 95%
- Material degradation due to corrosion $<$ 15 μm/year.

1.4 Limits of operation

The main limits of operation of a SPT are given by the external receiver. In this section the main limits that have to be estimated and controlled are exposed. They will have to be taken into account for the receiver design.

- Solar peak flux: to avoid overheat and damage the tube material it must not overpass 1.2 MW/m^2, hence the aiming strategy must be carefully controlled.

- Internal convective transfer coefficient: to assure an appropriate convective heat transfer between the salt and the tube wall the flow regime must be turbulent , Re>4000, (Petukhov, 1970). It homogenises the bulk temperature, and avoids tube overheating.

- Pressure stress: to avoid failure of the tubes it has to be under the limits specified in the ASME norm (ASME, 2011). Note that the pressure stress is related with the pressure inside the tubes, then it decreases with the tube thickness.

- Thermal stress: it is related with the mechanical properties of the tube materials (ASME, 2011), it must be lower than 33% of the ultimate tensile strength (UTS) of each material. Elevated values cause damages by fatigue and cracking. Diminishing the tube thickness the thermal stresses are also reduced.

- Film temperature: it depends of the tube material, but it is around 600-650 °C. High film temperature produces tube corrosion and changes in the material properties.

- Pressure drop: it must be as minimum as possible to reduce the feed pump consumption and the parasitic power of the SPT. It is not recommended values higher than 20 bars.

1.5 Scope of the thesis

In the previous sections the importance of the receiver in solar power tower has been stated. In addition, it has been highlighted the extreme work conditions of the receiver, the difficulty of measure the input data of this system, and the necessity of develop models that estimate its efficiency and its temperature distribution. This motivates the following key objectives of the present PhD thesis.

- Demonstration of the viability of a potential energy recovery system that reduces the parasitic energy consumption of the SPT.

- Development of a thermal model to estimate the thermal efficiency and the temperature distribution of the solar external receivers.
- Demonstration of the importance of the circumferential variations in the temperature distribution on the receiver to properly estimate the thermal efficiency of an external receiver.
- Use the thermal model to provide the guidelines for the proper design of the solar external receivers given the heliostat field.
- Study of the viability of a next generation of molten salt SPT with supercritical power blocks. To increase the vapour quality will be necessary to elevate the outlet temperature of the molten salt of the receiver.

1.6 Outline of the thesis

This PhD thesis presents the guidelines for designing a solar external receiver that assures the safety operation of the plant and maximizes its thermal efficiency. The studies performed during this time have been ordered to give a logical order to the thesis. It has been organize in 8 chapters. Chapters 2 to 7 have been written as independent self-contained articles with their own abstract, introduction, notation and bibliography.

This dissertation starts with the analysis of the molten salt SPT in order to find its weakness. In this way, Chapter 2 presents a new system that reduces the levelized cost of the SPT by means of the potential energy recovery of the hot molten salt downs from the receiver.

It has been observed that the receiver is the most critical system of the plant due to their extreme operating conditions. So, to assure a safe operation of the SPT the receiver has to be studied in detail. In Chapter 3 of this dissertation, a 2-D simplified thermal model for the external receivers has been developed. The main characteristics of this simplified model is that it considers circumferential and axial variations of the temperature in the receiver tubes, but also the main heat exchange mechanisms, and properties variations of the materials involved. In addition, the model has been compared with CFD simulations. The main advantage compared to CFD models is the computational cost with similarity of the results.

In Chapter 4 the model has been compared with experimental data and other simplified models. Several differences in the calculation of the receiver efficiency have found and explained in this fourth Chapter.

The aim of the receiver model is to stablish the guidelines for design solar external receivers, and then in Chapter 5 different geometries of external solar receiver has been simulated in order to stablish the most influent variables for the receiver design. In that decision thermal, mechanical, and hydrodynamic factors have been taken into account.

In Chapter 6 the flow pattern configuration of the receiver has been analyzed using the developed thermal model. This study it has done once the heliostat field of the SPT has been defined and included a whole year of receiver operation.

Chapter 7 includes a cost reduction and receiver design optimization in order to study the viability of a new generation of molten salt SPT operating with supercritical and ultra-supercritical Rankine power blocks.

Finally the conclusions obtained from this doctoral thesis are summarized in Chapter 8.

Nomenclature

CSP	Concentrated solar power
HTF	Heat transfer fluid
LEC	Levelized energy cost
LFC	Linear Fresnel colector
PTC	Parabolic trough colector
SCC	Stress corrosion cracking
SDC	Solar dish concentrator
SPT	Solar power tower
UTS	Ultimate tensile strength

References

Abengoa 2014 Khi Solar One. *Tech. Rep.*. Abengoa, Upington (South-Africa).

Alibaba 2015 Alibaba Group www.alibaba.com/product-detail/high-temperature-alloy-inconel-625-seamless_1988810062.html?s=p.

ASME 2011 ASME Boiler and Pressure Vessel Code, Section II - Materials. *Tech. Rep.*. American Society of Mechanical Engineers, New York.

Ausra 2014 www.ausra.com/technology.

Beerbaum, S. & Weinrebe, G. 2000 Solar thermal power generation in India - a techno-economic analysis. *Renewable Energy* 21 (2), 153–174.

Bezian, J.J. 1986 Themis solar power plant firs evaluation results. In *Biennial Congress of the International Solar Energy Society* (ed. Intersol Eighty Five), pp. 1408–1412. Elsevier.

Bradshaw, R.W. 1987 Thermal Convection Loop Study of the Corrosion of Incoloy 800 in Molten $NaNO_3$-KNO_3. *Corrosion-Nace* 43 (3), 173–178.

Dhyia Aidroos, B.; Hasimah Abdul, R.; Wan Zaidi Wan O; & Saeed Obaid, F. 2015 Historical development of concentrating solar power technologies to generate clean electricity efficiently - A review. *Renewable and Sustainable Energy Reviews* 41, 996–1027.

DOE 2015 CSP component research and development. energy.gov/eere/sunshot/csp-component-research-and-development.

DOE, NREL; & Sandia 1998 Solar Two. *Tech. Rep.*. http://www.nrel.gov/docs/fy99osti/24643.pdf, Bradshow, California.

eSolar, Brightsource & Abengoa 2008 Solar Thermal technology on an industry scale. *Tech. Rep.*. eSolar, Brightsource, Abengoa Solar.

Gil, A.; Medrano, M.; Martorell I.; Lázaro A.; Dolado P.; Zalba B. & Cabeza, L.F. 2010 State of the art on high temperature thermal energy storage for power generation. Part 1 - Concepts, materials and modellization. *Renewable and Sustainable Energy Reviews* 14 (1), 31–55.

Hefni, B. & Soler, R. 2015 Dynamic Multi-configuration Model of a 145 MWe Concentrated Solar Power Plant with the ThermoSysPro Library (Tower Receiver, Molten Salt Storage and Steam Generator). *Energy Procedia* 69, 1249–1258.

Hering, W.; Stieglitz, R. & Wetzel, T. 2012 Application of liquid metals for solar energy systems. In *EPJ Web of Conferences*, , vol. 33, p. 03003.

Ho, C.K. & Iverson, B.D. 2014 Review of high-temperature central receiver designs for concentrating solar power. *Renewable and Sustainable Energy Reviews* 29, 835–846.

Ho, C.K., Roderick Mahoney, A., Ambrosini, A., Bencomo, M., Hall, A. & Lambert, T.N. 2013 Characterization of Pyromark 2500 Paint for High-Temperature Solar Receivers. *Journal of Solar Energy Engineering* 136 (1), 4.

Kolb, G.J. 2011 An Evaluation of Possible Next-Generation High-Temperature Molten-Salt Power Towers. *Tech. Rep.* December. Sandia National Laboratories, Alburquerque and Livermore, SAND20011-9320.

McConohy, G. & Kruizenga, A. 2014 Molten nitrate salts at 600 and 680 °C: Thermophysical property changes and corrosion of high-temperature nickel alloys. *Solar Energy* 103, 242–252.

NREL 2011 http://www.nrel.gov/csp/solarpaces/by_project.cfm.

Pacheco, J.E. 2002 Final Test and Evaluation Results from the Solar Two Project. *Tech. Rep.* January. Sandia National Laboratories, Albuquerque, SAND2002-0120.

Pacio, J. & Wetzel, T. 2013 Assessment of liquid metal technology status and research paths for their use as efficient heat transfer fluids in solar central receiver systems. *Solar Energy* 93, 11–22.

Pavlović, T.M.; Radonjić, I.S.; Milosavljević D D. & Pantić, L.S. 2012 A review of concentrating solar power plants in the world and their potential use in Serbia. *Renewable and Sustainable Energy Reviews* 16 (6), 3891–3902.

Petukhov, B.S. 1970 *Heat Transfer and Friction in Turbulent Pipe Flow with Variable Physical Properties*, , vol. 6. Moscow (USSR).

Pitz-Paal, R.; Dersch, J. & Milow, B. 2005 European concentrated solar thermal road-mapping. *Tech. Rep.*. ECOSTAR, WP3 Deliverable N7, Cologne, (Germany) SES6-CT-2003-502578.

Price, H. 2003 Assessment of Parabolic Trough and Power Tower Solar Technology Cost and Performance Forecasts. *Tech. Rep.* October. NREL, Chicago.

Re, Munichc 2012 http://www.munichre.com/en/group/focus/climate-change.

Richter, C.; Teske, S. & Short, R. 2009 Concentrating solar power global outlook 09 - why renewable energy is hot. *Tech. Rep.*. Greenpeace International, SolarPACES, ESTELA, Amsterdam.

Schiel, W.J.C. & Geyer, M.A. 1988 Testing an external sodium receiver up to heat fluxes of 2.5 MW/m^2: Results and conclusions from the IEA-SSPS high flux experiment conducted at the central receiver system of the Plataforma Solar de Almeria (Spain). *Solar Energy* 41 (3), 255–265.

Seia & SolarPACES 2001 Concentrating solar power : Energy from mirrors. *Tech. Rep.*. U.S. Department of energy (DOE), Washington, DOE/GO-102001-1147.

Sener 2015 Gemasolar view.

Singer, Cs., Giuliano, S. & Buck, R. 2014 Assessment of Improved Molten Salt Solar Tower Plants. *Energy Procedia* 49, 1553–1562.

Torresol 2010 Torresol Energy: Gemasolar. www.torresolenergy.com/TORRESOL/gemasolar-plant/en.

Vignarooban, K.; Xu, X.; Arvay A.; Hsu K. & Kannan, A.M. 2015 Heat transfer fluids for concentrating solar power systems - A review. *Applied Energy* 146, 383–396.

Zhang, H.L.; Baeyens, J.; Degrève J. & Cacères, G. 2013 Concentrated solar power plants: Review and design methodology. *Renewable and Sustainable Energy Reviews* 22, 466–481.

CHAPTER

TWO

Components and operation modes of molten salt solar power towers

Contents

Scientific Contributions

- R. Wiesenberg, M.R. Rodríguez-Sánchez, E. Serrano, J. Villa, H. Barroso, D. Rayo, A. Ruano, D. Santana. PERS: Potential Energy Recovery System. Proceedings of SolarPaces, Marrakech, Morocco (2012).

- M.R. Rodríguez-Sánchez, A. Sánchez-González, C. Marugán-Cruz, D. Santana. Saving assessment using the PERS in solar power towers. Energy Conversion and Management, 87 (2014) 810-819.

2.1 Abstract

The improvement of the solar power tower using solar salt is one of the main goals of researchers. Any method or invention to improve the efficiency of this technology contributes to promote the renewable energies. The use of a Potential Energy Recovery System (PERS) in two different solar power tower plants of 20 and 100 MW has been analysed.

The PERS is formed, at least, by one turbine, located at the hot salt pipe coming from the receiver. The turbine is engaged to the shaft of the feed pump, which raises the heat transfer fluid from the cold tank to the receiver. It reduces the parasitic power consumption of the plant, and increases its global efficiency.

Different PERS configurations have been modelled. Based on an energetic and economic analysis, the optimal configuration is a geometrical similar turbine of three times the volume flow rate of one feed pump. The PERS has been proven to be a cost reductive and clean tool. For a 100 MW power plant of 30-year lifetime the investment cost is 1.26 M$ and the annual cash flow is 0.89 M$, while for a plant of 20 MW these values are 0.26 M$ and 0.19 M$, respectively.

2.2 Introduction

In recent years there is a resurgent interest in concentrating solar power technologies with storage. One of the most promising technologies is the Solar Power Tower (SPT), due to its high availability and dispatchability. Industry and laboratory research efforts are now focusing on optimizing SPT. Precisely, there are numerous SPT around the world used for research: NSTTF (New Mexico), PSA (Spain), Julich Solar Tower (Germany), CSIRO (Australia), or Thèmis (France) are some examples (Blanco *et al.*, 2010; Hoffschmidt *et al.*, 2012; Lovegrove & Stein, 2012).

The central receiver concept is based on a field of individually sun-tracking mirrors, which reflect the incident solar radiation to a receiver at the top of a tower. This way, the direct radiation is concentrated in the receiver allowing it to reach high solar flux. Typically, 75% to 90% of the reflected energy is absorbed and transferred to a working fluid, which is pumped up the tower (Benammar *et al.*, 2014; Jianfeng *et al.*, 2010; Lata *et al.*, 2008; Yang & Fan, 2012; Huang & Xu, 2014).

SPT usually include a cold storage tank and a hot storage tank at the bottom

of the tower, which provide and collect the fluid that flows through the receiver. The heat transfer fluid (HTF) is pumped from the cold tank to the top of the tower, flowing through the receiver. And then, the hot HTF is collected in the hot tank or is sending to the evaporation train, that usually is a super-critical Rankine cycle (McGovern & Smith, 2012). In the receiver outlet, the HTF has high mechanical energy, sum of its kinetic energy and of its potential energy, result of the height of the tower.

Due to the high pressure at the hot tank inlet, it is necessary to laminate the flow to avoid overpressure in the hot tank and possible damages in the storage system. A passive system of plates that produces the necessary pressure drop has been traditionally employed. The energy dissipated by pressure drop is an energy sink.

In order to improve the SPT efficiency several actions have been recommended by Kolb & Gary (2011): optimize the heliostat field layout, optimize the receiver design (Rodríguez-Sánchez & Santana, 2014), increase the plant availability, improve the power block, and/or improve the energy balance.

It has been proved that the electrical power required by the SPT to generate solar electricity (parasitic power) is relatively high, at least 10% of the energy produced (Kolb & Gary, 2011). This parasitic power consumption can be divided in the three main blocks of the SPT: the heliostat field with the tracking system, the receiver with the salt-circulation and the receiver feed pumps, and the power system with the steam-circulation, booster and condenser pumps. The only system susceptible to recover part of its consumed power is the molten salt pumps that feed the receiver. In addition, the mayor parasitic power of the plant is consumed by these pumps.

Therefore, this study is focused on the improvement of the energy balance of SPT, by means of the implementation of a system that allows the recovery of the potential energy of the hot HTF that comes from the receiver. The studied Potential Energy Recovery System (PERS) is formed at least by a turbine that substitutes the current passive system of energy dissipation, which avoids damages in the hot tank. This turbine would be connecting to the shaft of the feed pump to save a significant part of the energy used to pump the HTF to the receiver. This way, the parasitic power consumption of the thermal power plant will be reduced, improving the performance and the economic profit.

In this chapter two different sizes of SPT have been studied; one plant has a power forecast generation of 100 MW, and the other one of 20 MW. Both plants use molten salt as HTF. To complete the study, different PERS configurations

have been analysed to find the optimal PERS design for each plant.

Firstly, the SPT studied and theirs heliostat fields have been defined. Then, the hourly mass flow rate at the receiver has been estimated by the annual solar irradiation data. The power necessary to raise the HTF to the receiver and the power recovered by the PERS can be evaluated from the intersection of the pump/turbine characteristic curve, provided by the manufacturers, and the system resistance curve, calculated from the mass flow rate at the receiver.

2.3 Potential Energy Recovery System (PERS) description

The PERS is a system formed at least by a radial or an axial turbine on the hot salt pipe coming from the receiver, close to the bottom of the tower (see Figure 2.1). The aim of the PERS is to reduce the parasitic power consumption of SPT, recovering the potential energy from the HTF that usually is wasted, and then increasing the energy balance of the SPT. The PERS can be used in SPT working with different HTF, except for those with direct steam generation.

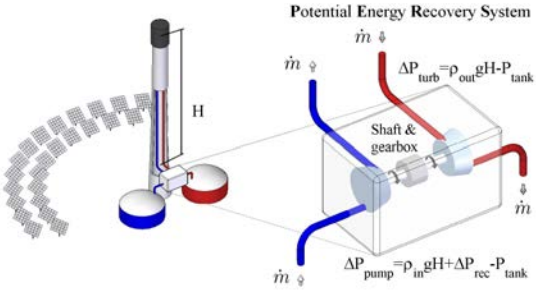

Figure 2.1: PERS scheme and location in a solar power tower plant.

The PERS can work in parallel to the traditional dissipative passive system or substitute it. The PERS may be disconnected by a valve if there is the risk of damaging the SPT or if there is low process profitability. A SPT could have more than one PERS operating in parallel.

The present chapter is focused on the mechanical configuration of the PERS (Serrano *et al.*, 2011), see Figure 2.2(a). In this configuration, the fluid is conducted through the PERS turbine, transforming the energy of the fluid into mechanical energy. That energy is transmitted through a driving belt, which

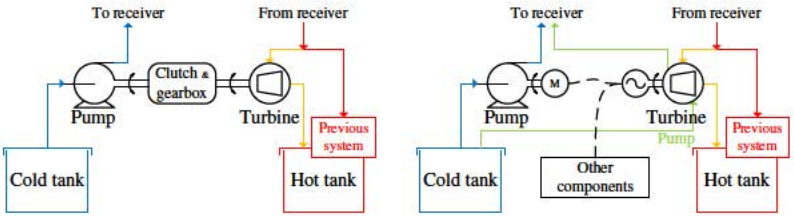

Figure 2.2: Block diagram of PERS. a) mechanical configuration. b) electrical configuration, Serrano *et al.* (2011).

joins mechanically the PERS turbine with the drive shaft of the feed pump.

The different pump and turbine revolutions can be adjusted using a gear box. Also, a clutch could be installed between pump and turbine to allow the system to engage or disengage, guaranteeing the correct operation in parallel. The mechanical transmission performance between the turbine and the pump is assumed to be 0.98 (Tenerelli, 2000).

Other possibilities of the PERS should not be rejected, for example the electrical configuration, see Figure 2.2(b). In this configuration the turbine revolutions must be adapted to a generator speed in order to produce electrical energy; that energy could be used by the different components that form the SPT. The energy transformation performance for this configuration is assumed to be 0.85 (Tenerelli, 2000). In emergency situations this configuration of PERS may reverse the usual operation process. The generator could converse into motor producing enough energy to pump the HTF from the PERS turbine to the receiver, green line of Figure 2.2(b).

2.4 Cases studied

The plants analysed are Gemasolar (Torresol, 2010), located in Seville, Spain, which is in operation since 2011; and Crescent Dunes (SolarReserve, 2014), located in Nevada, USA, and currently under construction. Table 2.1 collects the main parameters of each heliostat field configuration and receiver dimensions.

Crescent Dunes as well as Gemasolar use molten salt as HTF in a cylindrical external receiver. In both plant the solar salt enters into the receiver at 290

°C and leaves at 565 °C. However, Crescent Dunes generates four times more electrical power than Gemasolar. It is possible by larger surface of mirrors and receiver, and higher tower. In both cases, the receivers are formed by 16 panels, divided in two flow paths. The receiver efficiencies have been calculated following Benammar *et al.* (2014) and Rodríguez-Sánchez & Santana (2014).

Table 2.1: Main design parameters for Crescent Dunes and Gemasolar (Rodríguez-Sánchez & Santana, 2014; Trabish, 2013; Burgaleta *et al.*, 2009; Lata *et al.*, 2010; Golden, 2015).

Parameters	**Crescent Dunes**	**Gemasolar**
Latitude [°]	38.24	37.56
Land inclination [°]	0	0
Electricity Generation [GWh/year]	485	110
Number of heliostats [-]	10,300	2,650
Heliostat width [m]	11.28	10.76
Heliostat height [m]	10.36	10.76
Field boundary radius [m]	1,380	732
North shift of the boundary [m]	240	179
Tower optical height [m]	180	120
Receiver height [m]	20	10.5
Receiver diameter [m]	17.6	8.5
Receiver panel width [m]	3.5	1.499
Internal tube diameter [m]	0.042	0.033
Number of tubes per panel [-]	76	41
Receiver efficiency [-]	0.76	0.772

Crescent Dunes and Gemasolar heliostat fields follow a radial staggered arrangement, except in the inner zone of Gemasolar which is cornfield. Based on scaled images the radius of each row has been gathered and along with the number of heliostats per row, both heliostat fields have been generated in Matla®. Following the methodology by Augsburger (2013), only the heliostats inside a boundary circle, whose center is shifted to the north of the tower base, remains in the field. Radius and north shift of boundary circle for the selected fields can be examined in Table 2.1 and the resulting fields are shown in Figure 2.3; note the difference in land surface occupied by each field.

The heliostat efficiency, η_{hel}, is the product of loss factors affecting its optical

performance (Benammar *et al.*, 2014):

$$\eta_{hel} = ref \cdot cos(\beta)\eta_{at}\eta_{s\&b}\eta_{sp} \tag{2.1}$$

Where ref is the reflectivity of the mirrors defined as a constant whose value is 0.88 Noone *et al.* (2012); $cos(\beta)$ is the angle between the heliostat normal and the solar radiation direction, which has been computed using the sun position correlation reported in Duffie & Beckman (1991). The atmospheric attenuation losses, η_{at}, depend on the distance of the heliostat and the receiver, S, and are calculated following Schmitz & Pitz-Paal (2006):

$$\eta_{at} = \begin{cases} 0.99321 - 0.0001176S + 1.97 \cdot 10^{-8}S^2 & S \leq 1,000\text{m} \\ \\ \exp(-0.0001106S) & S > 1,000\text{m} \end{cases} \tag{2.2}$$

The shadowing and blocking factor, $\eta_{s\&b}$, has been computed by means of parallel projection of the neighbour heliostats (Collado & Guallar, 2012). Initially fourteen neighbour heliostats are assigned to each heliostat, even though this number is halved neglecting those heliostats behind the plane of the object heliostat.

Finally, the spillage or intercept factor, η_{sp}, is the fraction of reflected solar flux intercepted by the receiver. This factor has been obtained using the methodology described by Sánchez-González & Santana (2015). Such method is based in the projection of the flux density distribution from the image plane into the receiver surfaces, considering several aiming points as did Besarati *et al.* (2014). Further details about flux model for external receiver can be found in Sánchez-González & Santana (2015).

Given a heliostat field composed of N_{hel} heliostats, the hourly efficiency of the field, η_{field}, is:

$$\eta_{field} = \frac{\sum_{hel=1}^{N_{hel}} \eta_{hel}}{N_{hel}} \tag{2.3}$$

To avoid a great computational cost in the calculation of the optical efficiency, the methodology proposed by Wagner (2008) have been used. Wagner (2008) shown that the optimal sample days, equally spaced between the solar declination angle. Thus, the representative Julian day numbers are 172 (summer solstice), 218, 238, 256, 272, 290, 310, and 355 (winter solstice). To

calculate the optical efficiency of the field during a whole year, each hourly efficiency has been interpolated from those representative days. This methodology is also used by the free software SAM (Solar Advisor Model)distributed by NREL (Golden, 2015).

2.4.1 Field calculation

Firstly, the efficiency of each heliostat for Crescent Dunes and Gemasolar fields has been computed during the sun hours of the 8 representative days. It has been taking into account that the sun hours are different depending on the number of Julian day and on the location of the plant; it means that the sun hours are function of the elevation and azimuthal angles of the sun. A SPT does not work if the sun elevation angle is lower than 15° (Collado & Guallar, 2013). Then, the sun hours vary from 6 h to 18 h in summer until from 10 h to 14 h in winter.

For both plants the annual average efficiency of each heliostat has been estimated from the 8 representative days; it is shown in Figure 2.3. It can be seen that in both fields the heliostats with maximum efficiency are in the north and close to the tower. The range of heliostat efficiencies is similar in either plant. Since, Crescent Dunes has a larger number of heliostats; the field efficiency obtained for Crescent Dunes is lower, as it can be observed in Figure 2.4 that represents the hourly field efficiency of the 8 representative days. Furthermore, for both plants the efficiency of the field is around 5% higher in summer than in winter.

2.5 Energy balance using the PERS

The feed pump system is compounded by several centrifugal high-pressure vertical pumps working in parallel. In both studied plants the drive system consists of three pumps plus one reserve pump, all them are equal and their operational limit is defined by the maximum mass flow rate at the receiver divided by three. To calculate the power consumed by the pumping system it is necessary to know the characteristic curves of the pump, given by the manufacturer, and the resistance curve of the system. To calculate the resistance curve of the system, it is necessary to previously calculate the hourly mass flow rate at the receiver, $\dot{m}_{HTF}$, and the hourly pump head, H.

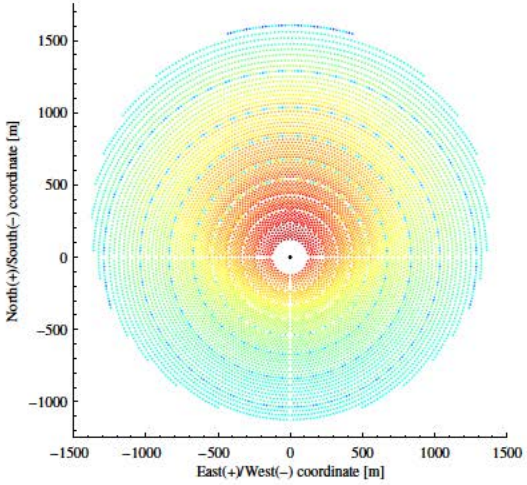

(a)

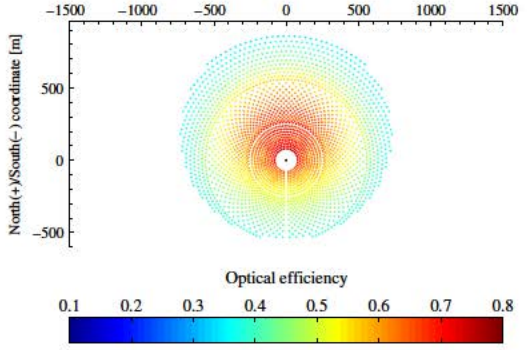

(b)

Figure 2.3: Heliostat annual average efficiency. a) Crescent Dunes. b) Gemasolar.

2.5.1 Mass flow rate

The hourly mass flow rate is estimated by means of an energy balance between the solar power absorbed by the HTF at the receiver (Equation 2.4) and the mandatory increase of the temperature of the solar salt at the receiver (Equation

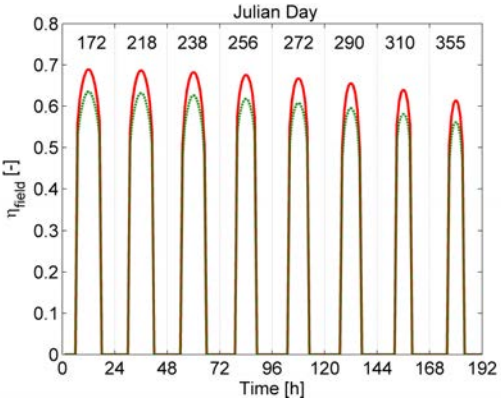

Figure 2.4: Hourly efficiency of the heliostat fields for the 8 representative days. Crescent Dunes (dot green line), Gemasolar (solid red line).

2.5).

$$E_{HTF} = DNI\eta_{field}N_{hel}A_{hel}\eta_{rec} \tag{2.4}$$

$$\dot{m}_{HTF} = \frac{E_{HTF}}{Cp(T_{out} - T_{in})} \tag{2.5}$$

Where DNI is the hourly direct normal irradiance obtained from **?**, A_{hel} represents the surface of one heliostat, η_{rec} corresponds to the receiver efficiency due to the heat losses, it has been assumed that η_{rec} is constant during the whole year, and its value has been obtained from a previous work (Rodríguez-Sánchez & Santana, 2014), T_{in} and T_{out} represent the inlet and outlet temperature of the molten salt at the receiver, 290 °C and 565 °C, respectively. Cp corresponds to the specific heat of the salt for an outlet - inlet average temperature obtained from Zavoico (2001), and whose value is 1,516.5 J/kgK.

Figure 2.5 shows the mass flow rate variation with time along the 8 representative days, using Equation 2.5. It can be seen that the mass flow rate in the receiver is strongly dependant on DNI; the chosen data of DNI are a five year prorated data. Therefore, the mass flow rate of the receiver has numerous variations along the year. However, the mass flow rate is higher in summer than in winter. The maximum mass flow rate for Gemasolar is around 335 kg/s

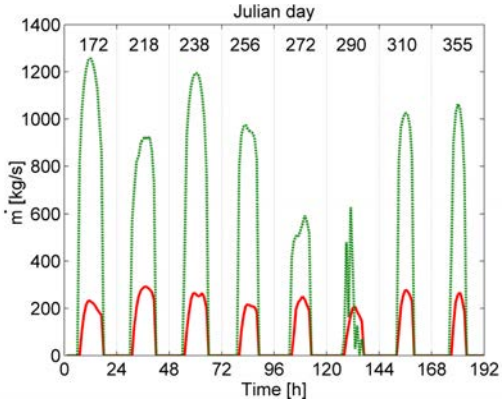

Figure 2.5: Mass flow rate for the 8 representative days. Crescent Dunes (dot green line), Gemasolar (solid red line).

(695 m^3/h), while in Crescent Dunes it is four times higher, around 1,280 kg/s (2,662 m^3/h).

These plants are designed for the maximum mass flow rate obtained. The operation process is as follows: when the mass flow rate is below one third of the maximum flow rate only one pump is working, for medium mass flow rate a second pump also operates, and only when the mass flow rate exceeds two thirds of the design point (maximum mass flow rate) the three pumps work in parallel. In both plants, the solar system operates at least 320 days per year, being the estimated time of operation for one pump at least 3,150 hours, for two pumps simultaneously working 2,550 hours, and for three pumps simultaneously working 1,480 hours in Crescent Dunes, and 2,910 hours, 2,415 hours, and 1,340 hours, respectively, in Gemasolar.

2.5.2 Pump Head

The head of the pump is defined as the potential power of the tower plus the pressure drop in the receiver and the tower pipes, and minus the pressure in the cold tank. The potential power is a function of the height difference between the cold tank and the receiver, Δh, and of the density of the molten salt at inlet work temperature, $\rho_{HTF,in}$=1906 kg/m^3 (Zavoico, 2001), while the pressure drop in the receiver has been calculated as Rodríguez-Sánchez & Santana (2014), considering the receiver a set of straight tubes, elbows, contractions and

expansions.

$$H_{pump} = \rho_{HTF,in} g \Delta h + \Delta p_{rec} - p_{tank} \tag{2.6}$$

The pressure drop in the receiver, Δp_{rec}, changes with the mass flow rate, therefore it is necessary to modify the operation mode of the pump to obtain the best efficiency as possible. The characteristic equations for a pump with frequency controller are obtained from the similarity relations of the centrifugal pumps. Then, the hourly pump efficiency, η_{pump}, is obtained at the intersection between the characteristic curves of the pump and the resistance curve of the pump system. The estimated hourly power supply by the pump, E_{pump} can be calculated using Equation 7.

$$E_{pump} = \frac{\dot{m}_{HTF} H_{pump}}{\rho_{HTF,in} \eta_{pump}} \tag{2.7}$$

For this work, Friatec has provided the head, shaft power and efficiency curves of a typical vertical pump used in molten salt SPT, see Figure 2.6. The model shown is a GVSO pump, whose design point is a head of 330 m, a volume flow rate of 820 m3/h, and an efficiency of 75.3%. The price of this pump is around 350,000 $. The characteristic curves of the pump provided by Friatec are adequate for the operational conditions of Crescent Dunes, see solid lines at Figure 2.6. However, Gemasolar has been solved using the similarity laws of the centrifugal pumps.

Figure 2.6 also shows the resistance curve of one feed pump of Crescent Dunes, and it efficiency has been represented by green plus symbols (+). The head of the pump is given by $h_{pump} = 2.9 \cdot 10^{-5} Q^2 + 6.5 \cdot 10^{-3} Q + 343.6$[m], where Q is the hourly volume flow rate. Although, the efficiency does not follow a perfect second order equation due to the speed control of the pump; several values are shown in Figure 2.6. To carry out these calculations, it has been assumed smooth tubes and a dynamic viscosity of 0.0016 Pas.

2.5.3 PERS Turbine

Due to the extreme operational conditions, the PERS turbines must satisfy several requirements: bear high temperatures (about 600 °C) and a corrosive ambient, high robustness, no moving parts, no lubricant, and no cavities in order to avoid solidification or stagnation. The turbines that could bear these

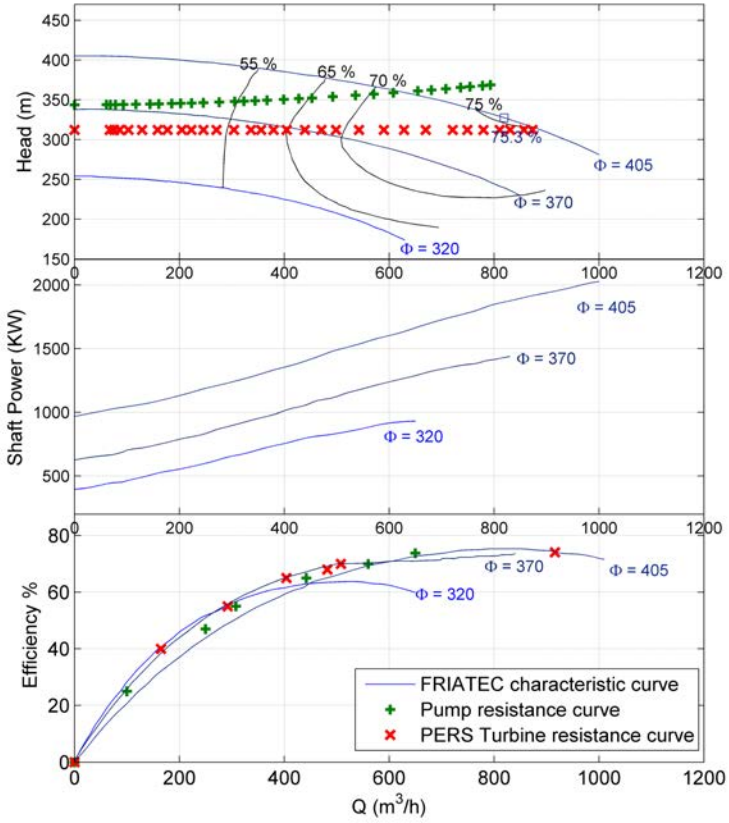

Figure 2.6: Characteristic and resistance curves of a GVSO vertical pumps and PERS turbine for Crescent Dunes.

conditions can be the same vertical pumps used to raise the HTF, but operating in turbine regime. The PERS turbine must be installed taking into account the same considerations that the feed pumps. To avoid salt freeze in the starting and stopping it must have a pre-heated system, and it must allow gravity drain.

Nowadays, there is no knowledge of the commercialization of this kind of pumps working as a turbine (PAT). In absence of theoretical and experimental data, the curves of Figure 2.6 have been used to calculate the efficiency of the turbine, following Derakhshan & Nourbakhsh (2008) where is stated that the

maximum efficiency is approximately the same in pump and turbine modes. In this case the head of the turbine is constant for the whole range of mass flow rate, and it is equivalent to the height of the column of HTF, $\rho_{HTF,out} g \delta h$, where $\rho_{HTF,out}$ is 1730 kg/m3 (Zavoico, 2001). Then, the power recovered by the turbine can be calculated by Equation 2.8, where η_{turb} is the instantaneous turbine efficiency calculated with the resistance curve of the turbine and the characteristic curves of the turbine. Note that the volume flow rate at the turbine is higher than at the pump, due to the density variations of the salt.

$$E_{turb} = \eta_{pump} \frac{\dot{m}_{HTF} H_{turb}}{\rho_{HTF,out}} \tag{2.8}$$

In Figure 2.6 a PERS turbine geometrically similar to the feed pump also has been represented by red crosses (X). In addition, to obtain the saved electrical power using the PERS, E_{turb} must be multiplied by the energy transformation coefficients of the corresponding PERS configuration.

2.5.4 PERS configurations

As a single turbine cannot recover the potential energy of the whole flow rate at the receiver, several PERS configurations have been analysed. Firstly, the possibility of setting up two or three PERS working in parallel has been studied (configurations 1 and 2 of Figure 2.7). Each turbine is geometrically similar to the feed pumps and between them, and they will be engaged to the corresponding feed pump.

In addition, by similarity other two PERS turbine configurations have been studied. One has a design point equivalent to twice the maximum volume flow rate of the feed pumps (configurations 3 of Figure 2.7), and the other three times the maximum volume flow rate of the pumps (configurations 4 of Figure 2.7).

2.6 Cost − Benefit analysis

To complete the PERS implementation study, a cost-benefit analysis (CBA) has been made in order to determinate the income using this system. The model developed by Li *et al.* (2014) has been used to calculate the net present value. In addition, the worst scenario described by Perini & Rosasco (2013) has been chosen to evaluate the CBA for the PERS.

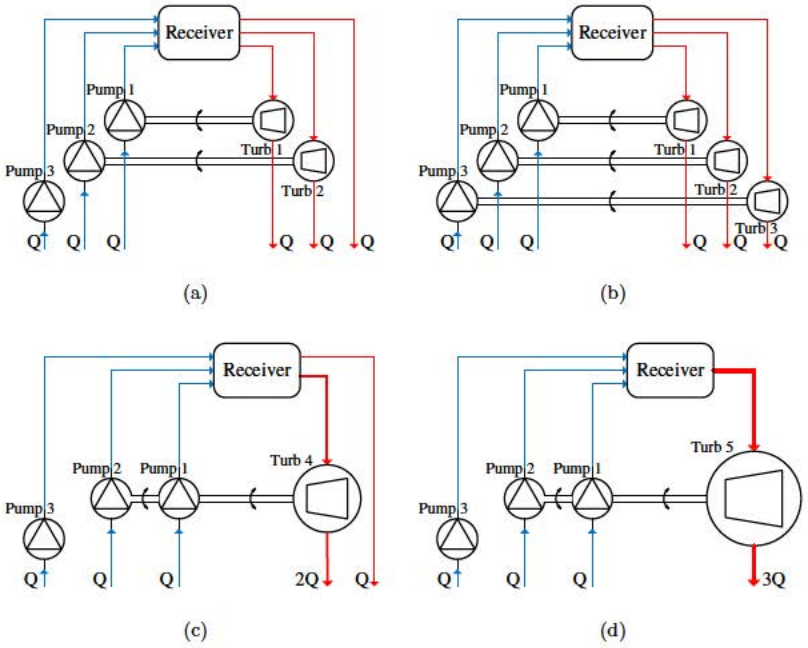

Figure 2.7: Different PERS configurations studied. a) Configuration 1: two PERS working in parallel. b) Configuration 2: three PERS working in parallel. c) Configuration 3: One PERS of two times Q_{max}. d) Configuration 4: One PERS of three times Q_{max}.

The benefit of the PERS is equivalent to the profit of the electricity sale and the additional profit resulted from the carbon credits. In the Spanish electrical market around two thirds of the energy is negotiated in a day-ahead spot market. Power plants under special regime may choose once a year between two possible ways of selling their energy: a feed-in tariff or participation in the wholesale market plus a premium (SpainGovernment, 2007; Usaola, 2012). Gemasolar is regulated by the feed-in tariff, then this electrical production is paid at 26.93 c€/kWh during the first twenty five years and during the following years the kWh will be paid at 25.4 c€/kWh. The Policy Mechanisms for the CSP electric market in USA are four: power purchase agreement (PPA), renewable portfolio standards that depends of every State, loan guarantee, and investment tax credits (Gallego & Bial, 2013). Crescent Dunes has obtained a power purchase agreement with the Nevada Government by which all the energy

that the plant will product during the first twenty five years will be acquired at 13.5 c$/kWh (Golden, 2015).

The carbon dioxide released by coal- fired power plants, f, is about 0.9 kg/kWh for USA and 0.93 kg/kWh for Spain (International Energy Agency, 2012). It has been assumed that the price of the coal, P_c, annually increases with constant inflation rate, θ. Then, as the solar electricity sale price is fixed for both studied plants, the annual profit can be expressed as $B^k = E_s P_s^k + fE_s P_c(1+\theta)^{k-1}$, where E_s is the annual electricity output (recovered by the PERS), P_s corresponds to the price of the electricity, and k represents the year of study, from 1 to the whole service period, x, see Table 2.2.

The cost analysis in the whole service period includes three parts: the principal and interest of loans in the repayment period, the operation and maintenance costs, and the tax costs: $C^k = C_p^k + C_I^k + C_O^k + C_T^k$. It has been assumed that all the investment is borrowed, and that the repayment time is y, see Table 2.2. An equal principal repayment with interest rate of loan, r, has been used. Note that, the tax cost is only applying to Spain because of in the State of Nevada the societies have fiscal advantages and the income tax rate is zero.

Taking into account the cash flows, and the discount rate τ, it is possible to estimate the total net present value (TNPV) and then the profit using the PERS. According to Okoye & Atikol (2014) the project is said to be economically feasible if the NPV>0, if otherwise, it is said to be non-feasible.

$$TNPV = \sum_{k=1}^{n} NPV_k = \sum_{k=1}^{n} \frac{B_k - C_k}{(1+\tau)^k} \tag{2.9}$$

2.7 Results

In this section a study of the best configurations and size of the turbine of the PERS is performed, based on both, energetic and economic analysis.

Figure 2.8(a) shows the sum of the recovered power by each of the three PERS turbines of Crescent Dunes and the relation of this power with the consumption of the feed pumps. It can be seen that the maximum instantaneous power recovered by each turbine is around 1 MW, meanwhile each pump consumed around 3 MW. As the efficiencies are similar for pump and turbine modes, the great difference of power is due to the pressure drop at the receiver, note that the velocity of the salt at the receiver is around 3.8 m/s for the maximum solar flux. In addition, this difference is also caused by the volume flow

rate difference at the pump and at the turbine. Note that around one third of the power consumed by the pumps can be recovered reducing the parasitic power consumption of the solar plant. Although the sum of the power recovered by the PERS turbines is always lower than the consumption of the first feed pump, each turbine must be mechanically engaged to the corresponding pump.

For Gemasolar, it has been supposed that the pumps are geometrical similar to the Crescent Dunes pumps for its corresponding flow rate, and relations of similarity for centrifugal pumps have been applied. In addition, it has been assumed that the turbine efficiency increases with the size of the turbine as Equation 2.10, (Dixon & Hall, 2014).

$$\frac{1-\eta_{turb,1}}{1-\eta_{turb,2}} = \left(\frac{D_{turb,2}}{D_{turb,1}}\right)^{0.25} \tag{2.10}$$

Figure 2.8(b) represents the same than Figure 2.8(a) but for Gemasolar. In this case the percentage of recovered power respect to the consumption of the pumps is higher. On one hand, it can be seen in the slope of the pump consumption that the pressure drop at the receiver is lower, due to the velocity of the salt in the tubes of the receiver is around 3.2 m/s for the maximum solar flux. On the other hand, the total volume flow rate of the plant and the tower height are lower, and the pumps consumption lesser, around 2 MW. In this plant, the implementation of PERS can saved around a 50% of the total power consumption of the feed pumps.

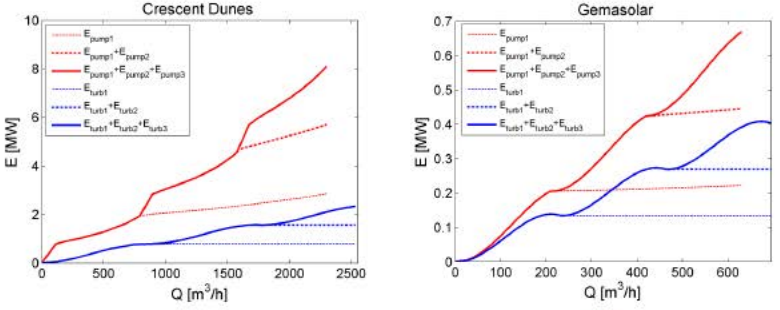

(a) (b)

Figure 2.8: Power consumed by the feed pumps and power recovered by each of the three PERS turbines working in parallel for Crescent Dunes. a) Individual power. b) Sum of power.

To try to save more energy and taking into account Equation 10 by means the turbine efficiency increases with the size, several turbine sizes have been analysed in order to obtain the optimal PERS design for the analysed plants. Applying the similarity law for turbines other two PERS turbines for each plant have been studied (configurations 3 and 4 of Figure 2.7).

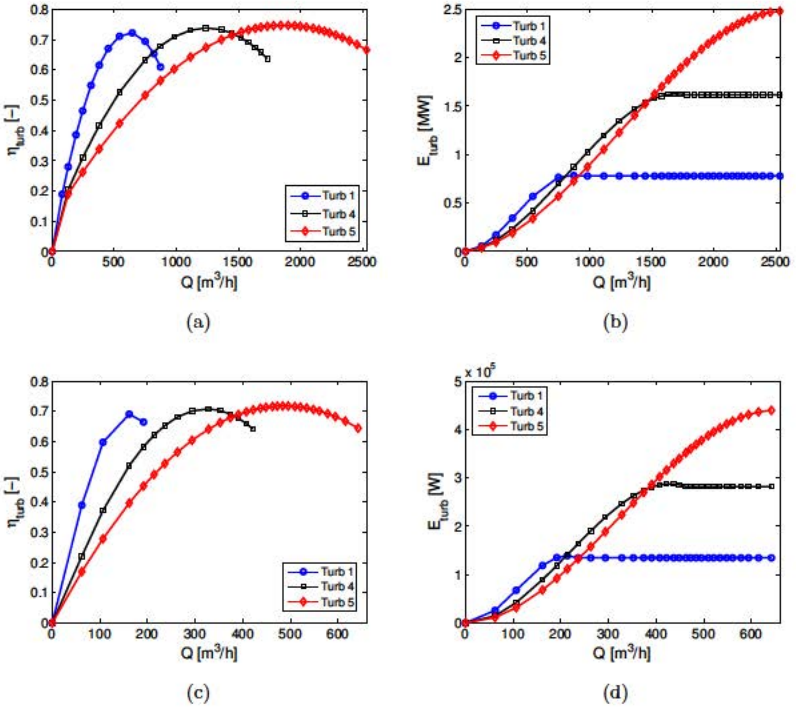

Figure 2.9: Geometrical similar turbines for PERS applications. a) Crescent Dunes: Efficiency. b) Crescent Dunes: Power recovered. c) Gemasolar: Efficiency. d) Gemasolar: Power recovered.

In Figures 2.9(a) and 2.9(c) it can be observed that the turbine efficiency grows with the geometrical similar turbine size, from 0.69 for the smallest PERS turbine of Gemasolar to 0.75 for the largest turbine of Crescent Dunes. In addition, the maximum efficiency is displaced to higher flow rates with the turbine size. Figures 2.9(b) and 2.9(d) represent the power recovered by each individual turbine, and as it was expected the largest turbine recover more energy that the others, even more than when three PERS in parallel are used.

A summary of the main results of the PERS implementation in both solar plants is shown in Figure 2.10. It shows the power recovered by the different configurations of PERS turbines multiplied by the factor of mechanical conversion, the rate of recovered energy respect to the pumps consumption, and the power consumption rate of each of the three pumps of the plants. The power recovered by Crescent Dunes is almost four times higher than the power recovered in Gemasolar. It is due to Crescent Dunes tower is taller than Gemasolar tower and operates with higher flow rate. In addition, the salt velocity in the receiver is higher for Crescent Dunes, producing a larger pressure drop.

The difference in the pressure drop at the receiver increases further the percentage of energy recovered by the PERS in Gemasolar than in Crescent Dunes. It has been estimated that the PERS can recover around 30% of the pump consumption for Crescent Dunes, and 70% for Gemasolar. Overall, the implementation of PERS allows to recover an important part of the power used in pumping the HTF from the tank to the receiver, and then allows to reduce the parasitic power consumption of the plants.

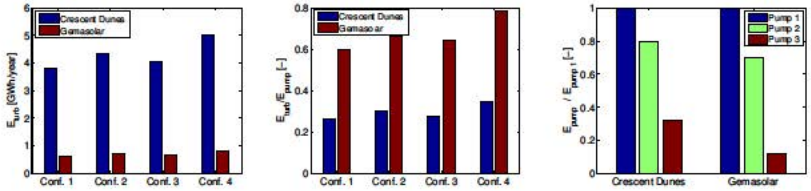

(a) (b) (c)

Figure 2.10: Energy balance results of the PERS implementation in Crescent Dunes and Gemasolar. a) Recovered energy. b) Rate of recovered energy. c) Rate of energy.

In Figure 2.10, it can be seen that the recovered energy by the PERS is similar for configurations 1, 2 and 3. However, in configuration 4 the recovered energy is significantly higher. For the use of turbines of large capacity, it is necessary to compare the recovered power to the power consumed by the pumps, in order to decide if the turbine must be engaged to one, two or the three feed pumps. The power consumed by each of the pumps can be seen in Figure 2.10(c). For Crescent Dunes the power consumed by the pumps is 16 times higher than for Gemasolar.

In the case of Crescent Dunes the similar turbines (configurations 3 and 4) recover less energy than the energy consumed by the first pump. Then, the

PERS turbine must be coupled only to the first pump. However, in Gemasolar the power recovered by configuration 4 is higher than the power consumed by the first pump. Then, its turbine must have a system to couple with the two first pumps, and to decouple of the second pump when it is not working.

In spite of that, an economic analysis is necessary to choose the most adequate PERS configuration, attending not only to energetic considerations but to the economic point of view. To make that decision Table 2.2 shows the main parameters used for the CBA calculations. For the estimation of the cost of the turbines of larger size than the presented by Friatec the relation of Equation 2.11 have been used (Towler & Sinnott, 2013):

$$C_2 = C_1 \left(\frac{W_2}{W_1} \right)^{0.7} \tag{2.11}$$

Table 2.2: Values of economic parameters used in carrying out cost-benefit analysis (Li *et al.*, 2014; Perini & Rosasco, 2013).

Economic parameters	**Crescent Dunes**	**Gemasolar**
Inflation rate, θ [%]	3	3
Interest rate of loans, r [%]	4.18	6.77
Income tax rate, t [%]	0	30
Repayment period of loans, y [year]	10	7
Whole service period, x [year]	30	30
First year maintenance cost, C_o^1 [$]	3000	1500
Solar electricity sale price, P_s [$/kWh]	$0,135$	0.2693
Carbon dioxide released, f [kg/kWh]	0.9	0.93
Carbon dioxide price, P_c [$/kg]	0.038	0.06
Discount rate, τ [%]	5.5	5.5

The results obtained in the cost-benefit analysis are shown in Figure 2.11. Although in Nevada the price of the electricity is lower than in Spain the fiscal conditions are better. Adding that the power recovered is higher for Crescent Dunes than for Gemasolar, it can be seen that the economic profit of Crescent Dunes is at least four times higher than for Gemasolar. In spite of that, for both plants the implementation of PERS would be profitable, it has been checked that the flow cash for all the years is positive and that the TNPV is mayor than zero, therefore the project is economically attractive.

Figure 2.11 shows the average annual cash flow for each studied configuration. As it was expected configuration 4 of PERS has the highest annual cash flow. Configuration 2 is the second more adequate PERS configuration, and Configuration 1 is the worst option.

To finalize with the economic analysis, the payback period has been calculated as the initial investment cost divided by the annual cash inflows. It has been assumed that the total initial investment cost has been paid without bank help. This parameter allows to estimate the time required to recover the cost of the initial investment; longer payback periods are typically not desirable for investment positions. It can be noticed that the first configuration has the shortest payback period and the forth the longer. However, as in all the cases studied the payback period is lower than two years, any configuration could be used.

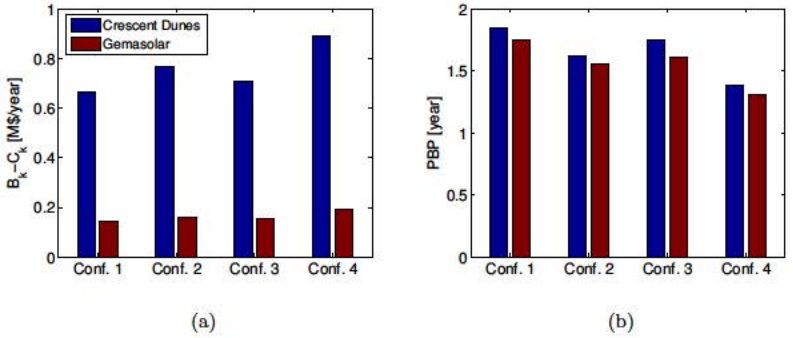

(a) (b)

Figure 2.11: Cost−Benefit analysis. a) Average annual cash flow. b) Payback Period.

2.8 Conclusions

The cost reduction and energetic saving using different PERS configurations in two different solar tower power plants have been estimated. The solar plants are located in different countries and one has a power forecast generation 5 times larger than the other. In this way, it is possible to compare the recovered energy between plant sizes and to compare the economic profit between countries.

The PERS configurations analysed are able to recover a significant part of the energy used to pump the HTF thought the receiver. In Crescent Dunes

the reduction of the parasitic power consumption of the receiver pumps reaches 26.32% for a turbine of the same size than the feed pump, and up to 34.4% for a geometrical similar turbine of three times the maximum flow rate. While in Gemasolar for the same configurations the recovered energy is 60.57% and 78.84%. This raise in the proportion of the recovered energy is mainly due to the velocity of the HTF in the receiver. The height of the tower plays a minor role in the rate of recovered energy. However, the net recovered energy is scaled with the size of the plant, (5.02 GWh/year for Crescent Dunes and 0.86 GWh/year for Gemasolar). Therefore, the overall efficiency of the plant improves considerably using the PERS, notably in plants of large power generation capacity and high towers. Consequently, the profit depends on the plant size and on the market regulation laws of each country. It has been assumed the worst scenario as possible, and in both cases the TNPV is mayor than zero and for every year the annual cash flows are positive. Then, the PERS set-up seems to be a profitable project. In Crescent Dunes for an initial investment cost of 1.26 M$ the average annual cash flow is 0.89 M$/year, and for Gemasolar whose initial investment cost of 0.26 M$ the average annual cash flow is 0.19 M$/year. In addition, the payback period is always lower than two years. Finally, the optimal PERS configuration would be the set-up of only one turbine of a design point three times the design flow rate of one feed pump. The second best option would be the implementation of three parallel turbines of the same size that the feed pumps.

Nomenclature

A	Surface area [m^2]
B	Benefit [$]
C	Cost [$]
C_p	Specific heat [J/kg° C]
D	Diameter [m]
DNI	Direct normal irradiance [W/m^2]
E	Power [W]
f	Carbon dioxide released [-]
g	Gravity acceleration [m/s^2]
H	Head [Pa]
h	Length [m]
$\dot{m}$	Mass flow rate [kg/s]

N	Number of elements [-]
P	Price [$]
p	Pressure [Pa]
Q	Volume per unit of time [m^3/h]
r	Loan interest rate [-]
ref	Reflectivity [-]
S	Heliostat-Receiver distance [m]
T	Temperature [K]
t	Income tax rate [-]
W	Shaft power [W]
x	Whole service period [year]
y	Repayment time [year]

Greek letters

β	Sun-Heliostat normal surface angle [°]
ΔP	Pressure drop [Pa]
η	Thermal efficiency [-]
θ	Inflation rate [-]
ρ	Density [kg/m^3]
τ	Discount rate [-]

Subscripts

at	Atmospheric
c	Coal
ci	Initial investment
hel	Heliostat
HTF	Heat transfer fluid
I	Interest
in	Inlet
max	Maximum
O	Operation and maintenance
out	Outlet
p	Principal repaid
rec	Receiver
s	Solar electricity

sp	Spillage
s& b	Shading and blocking
T	Tax
turb	Turbine

Abbreviattions

CBA	Cost-Benefit analysis
HTF	Heat transfer fluid
PERS	Potencial Energy Recovery System
SPT	Solar power tower
PAT	Pump as turbine
PPA	Power purchase agreement
TNPV	Total net present value

References

Augsburger, Germain 2013 Thermo-economic optimisation of large solar tower power plants. PhD thesis.

Benammar, S., Khellaf, a. & Mohammedi, K. 2014 Contribution to the modeling and simulation of solar power tower plants using energy analysis. *Energy Conversion and Management* 78, 923–930.

Besarati, Saeb M., Yogi Goswami, D. & Stefanakos, Elias K. 2014 Optimal heliostat aiming strategy for uniform distribution of heat flux on the receiver of a solar power tower plant. *Energy Conversion and Management* 84, 234–243.

Blanco, J, Heller, P, Mehos, M, Meier, A & Meyer, R 2010 Solar Power and Chemical Energy Systems Annual Report. *Tech. Rep.*. International Energy Agency (IEA), DLR.

Burgaleta, J.I., Arias, S. & Salbidegoitia, I.B. 2009 Operative advantages of a central tower solar plant with thermal storage system. In *SolarPACES*, p. n 11720. Berlin, Germany: SolarPACES.

Collado, F.J. & Guallar, J. 2012 Campo: Generation of regular heliostat fields. *Renewable Energy* 46, 49–59.

Collado, F.J. & Guallar, J. 2013 A review of optimized design layouts for solar power tower plants with campo code. *Renewable and Sustainable Energy Reviews* 20, 142–154.

Derakhshan, Shahram & Nourbakhsh, Ahmad 2008 Experimental study of characteristic curves of centrifugal pumps working as turbines in different specific speeds. *Experimental Thermal and Fluid Science* 32 (3), 800–807.

Dixon, S.L. & Hall, C.A. 2014 *Fluid Mechanics and Thermodynamics of Turbomachinery*, 7th edn. Butterworth Heinemann.

Duffie, J A & Beckman, W A 1991 *Solar engineering of thermal processes*. New York: Wiley.

Gallego, Belen & Bial, Marcel 2013 CSP Global MARKETS. *Tech. Rep.*. CSP Today.

Golden, C. 2015 System advisor model (sam). sam.nrel.gov/content/downloads.

Hoffschmidt, B., Alexopoulos, S., Göttsche, J., Sauerborn, M. & Kaufhold, O. 2012 *Comprehensive Renewable Energy*. Elsevier.

Huang, Weidong & Xu, Qian 2014 Development of an analytical method and its quick algorithm to calculate the solar energy collected by a heliostat field in a year. *Energy Conversion and Management* 83, 110–118.

International Energy Agency 2012 CO2 emissions from fuel combustion. *Tech. Rep.*. iea.

Jianfeng, Lu, Jing, Ding & Jianping, Yang 2010 Heat transfer performance of an external receiver pipe under unilateral concentrated solar radiation. *Solar Energy* 84 (11), 1879–1887.

Kolb, G.J.; Ho, C.K.; Mancini T.R. & Gary, J.A. 2011 Power Tower Technology Roadmap and Cost Reduction Plan. *Tech. Rep.* April. Sandia National Laboratories, Sandia National Laboratories, Albuquerque.

Lata, Jesús, Alcalde, Sergio, Fernández, David & Lekube, Xabier 2010 First surrounding field of heliostats in the world for commercial solar power plants - Gemasolar. In *Solarpaces* (ed. Sener), pp. 1–9.

Lata, Jesús M., Rodríguez, Manuel & Álvarez de Lara, Mónica 2008 High Flux Central Receivers of Molten Salts for the New Generation of Commercial Stand-Alone Solar Power Plants. *Journal of Solar Energy Engineering* 130 (2), 1–5.

Li, W., Wei, P. & Zhou, X. 2014 A cost-benefit analysis of power generation from commercial reinforced concrete solar chimney power plant. *Energy Conversion and Management* 79, 104–113.

Lovegrove, K & Stein, W 2012 *Concentrating solar power technology: principles, developments and applications*. Cambridge (U.K.).

McGovern, Ronan K. & Smith, William J. 2012 Optimal concentration and temperatures of solar thermal power plants. *Energy Conversion and Management* 60, 226–232.

Noone, Corey J., Torrilhon, Manuel & Mitsos, Alexander 2012 Heliostat field optimization: A new computationally efficient model and biomimetic layout. *Solar Energy* 86 (2), 792–803.

Okoye, Chiemeka Onyeka & Atikol, UÄ§ur 2014 A parametric study on the feasibility of solar chimney power plants in North Cyprus conditions. *Energy Conversion and Management* 80, 178–187.

Perini, Katia & Rosasco, Paolo 2013 Cost - benefit analysis for green façades and living wall systems. *Building and Environment* 70, 110–121.

Rodríguez-Sánchez, M.R.; Soria-Verdugo, A.; Almendros-Ibáñez J.A; Acosta-Iborra A. & Santana, D. 2014 Thermal design guidelines of solar power towers. *Applied Thermal Engineering* 63 (1), 428–438.

Sánchez-González, A. & Santana, D. 2015 Solar flux distribution on central receivers: A projection method from analytic function. *Renewable Energy* 74, 576–587.

Schmitz, M.; Schwarzbözl, P.; Buck R. & Pitz-Paal, R. 2006 Assessment of the potential improvement due to multiple apertures in central receiver systems with secondary concentrators. *Solar Energy* 80 (1), 111–120.

Serrano, E., Wiesenberg, R., Rayo, D., Barroso, H., Villa, J. & Santana, D. 2011 Solar Power Tower System.

SolarReserve 2014 SolarReserve: Crescent Dunes.

SpainGovernment 2007 Real Decreto 436/2004, de 12 de marzo.

Tenerelli, J. 2000 *Efficiency of the energy conversion*. College of Earth and Mineral Sciences.

Torresol 2010 Torresol Energy: Gemasolar. www.torresolenergy.com/TORRESOL/gemasolar-plant/en.

Towler, G. & Sinnott, R.K. 2013 *Chemical Engineering Design*, 2nd edn. San Diego, California: Elsevier.

Trabish, Herman K. 2013 A Climb Up the SolarReserve Solar Power Tower.

Usaola, Julio 2012 Participation of CSP plants in the reserve markets: A new challenge for regulators. *Energy Policy* 49, 562–571.

Wagner, M. J. 2008 Simulation and Predictive Performance Modeling of Utility-Scale Central Receiver System Power Plants. PhD thesis, University of Wisconsin, Madison.

Yang, X.; Yang, X.; Ding J.; Shao-Y. & Fan, H. 2012 Numerical simulation study on the heat transfer characteristics of the tube receiver of the solar thermal power tower. *Applied Energy* 90 (1), 142–147.

Zavoico, A.B. 2001 Solar Power Tower: Design Basis Document. *Tech. Rep.* July. Sandia National Laboratory, San Francisco, SAND2001-2100.

CHAPTER

THREE

Simplified heat transfer models for molten salt solar external receivers and comparison with CFD Simulations

Contents

Scientific Contributions

- M.R. Rodríguez-Sánchez, C. Marugán-Cruz, A. Acosta-Iborra, D. Santana. Comparison of Simplified Heat Transfer Models and CFD Simulations for Molten Salt External Receiver. Applied Thermal Engineering, 73 (2014) 991-1003.

3.1 Abstract

In the absence of experimental correlations of the solar external receiver performance, it is particularly necessary to develop thermal models to optimize the receiver operating modes and to properly design such equipment. Since CFD models require an enormous computational cost to simulate a receiver, two simplified bi-dimensional implicit-scheme models have been developed. Both models consider axial and circumferential variations on the heat flux absorbed by the tubes and on the wall temperature. One assumes homogeneous surface boundary condition and the other assumes homogeneous surface heat flux at the discretized tube wall.

The effects of mass flow rate, and wind velocity on the receiver performance have been analysed considering steady state operation. The results have been compared with a simulation carried out with ANSYS Fluent. Both simplified models are able to predict the heat fluxes, the salt and the tube wall temperature with a deviation lower than 6% compared to CFD simulations. The analysis of the developed models has been also compared with a model usually employed that does not consider variable circumferential temperature. The results show that keeping constant the circumferential tube wall temperature leads to lower wall temperature, underestimating the film temperature, the thermal stress and the salt decomposition.

3.2 Introduction

Solar power tower systems (SPT), using molten salt as a heat transfer fluid (HTF), are one of the most promising technologies for electricity generation. The solar field of a central receiver system is made up of hundreds or thousands of mirrors placed around the receiver, located at the top of the tower. One of the main advantages of SPT systems is the large heat storage capability, which allows these systems to generate electric power with continuity and stability. In SPT technologies much attention has been paid to the receiver design because according to Kolb & Gary (2011) its cost is around 19% of the total capital investment cost of a solar plant. A more detailed cost analysis can be done with the model developed by Singer *et al.* (2010). In addition, the receivers are subjected to extreme working conditions, having uncertain lifetime. The scarcity of experimental data makes necessary to develop thermal models to understand the operation modes and the optimization of the receiver, as well as

the degradation of the heat transfer fluid (HTF) López-González *et al.* (2013).

Not surprisingly there has been a strong interest in the scientific community to try to bring some light to this complex problem. The advantages of using molten salt as heat transfer fluid in CSP have been widely investigated by numerous authors. In particular, Yang & Fan (2012) analyzed experimentally and numerically a single receiver tube of 1 meter of length, using HITEC as HTF. In their study half tube was heated by an uneven radiation while the other half tube was considered an adiabatic surface. The heat transfer process over the tube was simulated with the commercial CFD software Fluent 6.1 using the Navier-Stokes momentum equations and the energy equation for a three dimensional compressible flow. The comparison between the numerical and experimental Nusselt numbers showed differences lower than $\pm$ 7.5%, in the range of Reynolds number of 10,000 $-$ 40,000. Lim *et al.* (2014) proposed a tubular solar receiver with porous medium; using the commercial software Fluent the conventional continuity, momentum, and energy equations were solved with a porous medium inside. They optimize the receiver design as a compromise between the maximum temperature of the porous medium and the maximum pressure drop. Garbrecht *et al.* (2013) also simulated with the commercial CFD software Fluent the heat transfer in a new design of external molten salt solar receiver, formed by many hexagonal pyramid shaped elements, of dimensions 100 mm of length and 30° of apex angle. They focused their CFD analysis on one pyramid element which was numerically simulated by coupling the heat flow into the receiver and the radiation with a Matlab® code.

Current CFD models do not simulate the whole receiver due to the high computational cost required to solve the problem. The different length scales of the system, i.e. receiver length or diameter compared to the tube diameter, would imply an enormous number of computational cells to simulate the complete receiver. Simplified models are currently used to decide the initial design of central receiver, simulating the whole receiver since they are less computationally expensive than CFD models.

Jianfeng *et al.* (2010) studied the efficiency of the heat absorption of an external receiver pipe under unilateral concentrated radiation considering only heat losses by natural convection and radiation based on the mean wall temperature of the tube. Singer *et al.* (2010) used an iterative receiver design algorithm (RDA) to calculate the receiver efficiency matrix according to the assessed HTF, tube dimensions and number of serially and serpentine flow through panels and tubes. Singer *et al.* (2010) considered heat losses through free convection, radi-

ation and reflection for each panel using the effective temperature of radiation, but they did not take into account circumferential wall temperature variations, which can be important for the estimation of radiation losses. Xu *et al.* (2011) employed an equivalent method to the Singer method in the calculus of the receiver, and Irfan & Chapman (2009) studied the thermal stresses in radiant tubes in the three directions . In addition, Lata *et al.* (2008) made a sensitivity analysis of a receiver panel based on the design of the SOLAR TRES receiver; they varied the number of tubes that form the panels, the tube external diameter and the tube thickness, in order to optimize the receiver efficiency. They carried out the analysis with a code developed by SENER (SENREC) and the results were used to obtain a prototype panel design.

The main goal of the present study is to develop two bi-dimensional simplified thermal models for external receivers that assume axial and circumferential variations on the heat flux absorbed by the tubes and on the tube wall temperatures, solving the receiver performance in a simply and fast mode. Both models consider grey surfaces, and constant internal convective coefficient with the angle. In addition, these models contemplate different initial hypotheses: first one considers homogeneous wall temperature (HTM) and the second one considers homogeneous heat flux (HHFM) in each discretized section of the receiver wall. The models have been developed using the commercial software Matlab®.

The results of the simplified models over the effects of mass flow rate, and wind velocity on the receiver working under steady state operation have been compared to the numerical results of a three-dimensional and more spatially simulation, carried out with the commercial CFD code ANSYS Fluent v.12, in order to probe that the hypotheses assumed by the developed models produce similar results than the numerical simulations. It has been obtained that the simplified models are able to predict the temperature of the molten salt, the tube wall temperatures, and the heat fluxes absorbed by the salt with low differences respect to CFD and having lower computational cost than CFD simulations.

3.3 External receiver characteristics

The molten salt external receivers are configured as 360° cylindrical tubular receivers, formed by a variable number of vertical tubes that gather into panels and through which the HTF flows, (see Figure 3.1). Each panel includes an

inlet and an outlet header, inlet and outlet nozzles and tubes Falcone (1986).

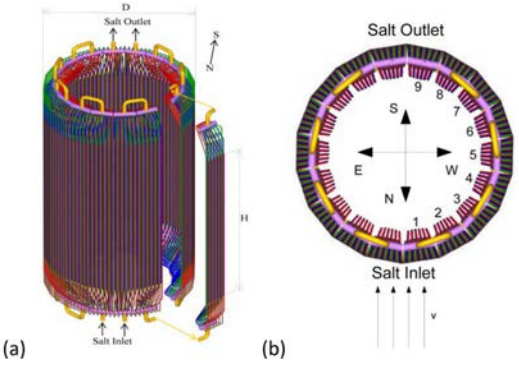

Figure 3.1: (a) External receiver scheme with one of the panel separated from the rest to improve visualization. (b) Relative position of the panels and wind velocity direction.

In the north hemisphere the salt enters in the receiver through the northern panel at low temperature, slightly above the melting point, $T_{salt}(0) = 290$ °C. The salt flow is divided into two paths (north-east-south and north-west-south), and in each circuit the salt passes through half of the panels of the receiver, as a serpentine. In each panel the salt flow is divided into the tubes that make part of the panel. As the salt moves through the panels the temperature of the salt increases cooling the tube walls.

The basic parameters of the receiver analysed in this study and the ambient conditions have been defined in 3.1. The HTF used in the simulations is molten salt, 60% KNO_3 − 40% $NaNO_3$, whose temperature variations of the density, dynamic viscosity, specific heat, and thermal conductivity are taken into account in the models, using the data given by Zavoico (2001). The material of the tubes is Niquel Alloy 800H and they are coated with Black Pyromark, a paint of high absorptivity of the solar radiation. In the models introduced in Sections 3.4 and 3.5, the density and specific heat of the tube material are considered to be constant with the temperature, and only the variations of the thermal conductivity with temperature are taken into account ASME (2011). In order to reduce the heat losses at the rear side of the tubes a refractory wall thermally insulated (mineral wool) and jacketed by a high reflectivity material, White Pyromark, is used Zavoico (2001). The values for the absorptivity

and emissivity coefficients of these materials have been obtained from Zavoico (2001) and Slemp & Wade (1962). The receiver configuration selected (number of flow paths, N_{fp}, number of tube panels, N_p, and the number of tubes per panel, N_t) is based on the receiver operation conditions included in Table 3.2.

Table 3.1: Design parameters of the external receiver and ambient conditions.

Parameters	**Symbol**	**Values**
Receiver: height,	H	7.4
diameter [m]	D	6
Tube:external and internal	d_{out}; d_{int}	42.2; 38.9
diameter, pitch [mm]	B	44.2
Salt: inlet temeprature [°C],	$T_{salt}(0)$	290
outlet pressure [bar]	$P_{salt}(HN_p/N_{fp})$	1
Sky: Temperature [°C]	T_{sky}	19.5
Number of:flow paths, panels,	N_{fp}; N_p	2; 18
tubes per panel, [-]	N_t	24
Emissivity: tubes. sky, refractory	$\overline{\epsilon_t}$; ϵ_{sky}	0.87; 0.895
wall, ground [-]	ϵ_{N_s+1}; ϵ_{gr}	0.2; 0.955
Visible tube absorptivity [-]	α	0.93
Fouling resistance [Km^2/W]	R_{foul}	$8.8 \cdot 10^{-5}$

The spring equinox-solar noon has been defined as the design point of the SPT Kistler (1986). Regarding the solar flux that reaches the receiver, Augsburger & Favrat (2013) showed that the flux radiation map for the spring equinox-solar noon is completely symmetric with respect to the North-South axis for a Gemasolar-like heliostat field. In the present work, following Augsburger & Favrat (2013), approximately a normal map that represents the spring equinox noon has been used for the definition of the radiation map along the receiver. This means a maximum value of the solar radiation in the northern panels of the receiver and a minimum value in the southern panels. Due to the symmetry, only one flow path of the receiver has been simulated.

One of the most popular codes to obtain the solar flux in a receiver, DELSOL3, divides the heliostat field in a maximum of 13 angular sectors Kistler (1986). Based on this code, the radiation map used in this study is a square grid of $13x13$. To simulate the whole receiver the radiation map has been axially divided in 13 blocks (N_b) of same length. However, in circumferential direction it is necessary to interpolate the radiation map grid to adapt it to the number

of panels (N_p) of the receiver. Assuming that the heat flux on all the tubes of a panel is approximately the same, the radiation map has been divided in N_p=18 fragments. Figure 3.2 shows the radiation map on one flow path of the receiver. The panels are indicated in the horizontal axis, while the height and the number of blocks in which the tubes are axially divided can be seen in the vertical axis. It can be observed that the maximum radiation arrives at the northern panel (N_p=1) and the minimum at the southern panel (N_p=9). Note that the radiation map it is not axially symmetric; the heat flux is higher in the top of the receiver than in the bottom Schwarzbözl & Schmitz (2009), and its maximum is located around 3 m length.

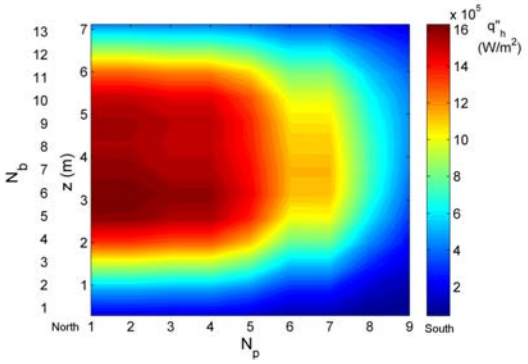

Figure 3.2: Radiation map scheme. The vertical axis contains the 13 axial steps in which the tubes has been divided and the horizontal axis contains the 9 panels that formed one flow path of the receiver.

To evaluate the advantages of the proposed models, five cases have been studied varying the mass flow rate of the molten salt ($\dot{m}$) and the wind velocity close to the receiver (v), see Table 3.2. However, in the study it has been assumed steady state conditions. The wind direction is North- South, since the effect of the wind on the receiver in that direction is the highest. In the cases where there is no wind, cases A, D and E, only natural convection has been taken into account to find the convective heat losses. The major part of the results will be based on case A because this case has intermediate salt mass flow rate and it is not influenced by external effects like the wind.

Table 3.2: Design parameters of the external receiver and ambient conditions.

Parameters	Case A	Case B	Case C	Case D	Case E
Wind velocity, v [m/s]	0	7.5	15	0	0
Salt mass flow rate, $\dot{m}$ [kg/s]	281.6	281.6	281.6	256	301

3.4 Simplified thermal models

In this section the two simplified thermal models developed in this study are presented. In both of them, the temperature of the tubes is assumed to vary in axial and circumferential directions of each tube. In the circumferential direction each tube has been discretized in several sections (N_s=37) and in the axial direction each tube has been divided in different blocks (N_b=13). The first model assumes homogeneous temperature in each discretized cell of the tube wall (HTM) whereas the second model assumes homogeneous heat flux absorbed by each discretized cell of the tube wall (HHFM). Finally, an even more simplified model (SM), where the tube wall temperature is considered to vary only in the axial direction is exposed.

Due to the complexity of the problem, only one tube per panel (or two semi-tubes) has been studied, see Figure 3.3. The effects of the adjacent tubes have been taken into account by using lateral symmetric conditions that results from assuming that every tube in a panel receives the same radiation flux, and therefore has the same wall temperature. Hence, the element of study is formed by two semi-tubes sited face to face, a rear surface thermally isolated, that can be considered as a refractory wall, and an imaginary front surface totally transparent to solar irradiation and through which the energy reflected to the sky is lost (see Figure 3.3). An artificial and punctual energy source representing an emitter of the reflected radiation is coming from the heliostat field.

In the models exposed in this study the z coordinate follows the salt flow direction. Its origin is the bottom of the first panel (north side), which means that $z = H$ is the end of the first panel (upflow), $z = 2H$ is the end of the second panel (downflow) and so on, until $z = HN_p/N_{fp}$ which is the end of the last panel. The circumferential coordinate, θ, has its origin at the front part of each tube, facing the heliostat field.

A staggered grid has been used in the salt flow direction (z), that allows to

obtain the salt calculations at the cell faces. However, the calculations made at the tube wall are performed in the middle of the cells. So that, the origin for the tube wall variables is displaced a length of $+\Delta z/2$ with respect to the salt variables in the salt flow direction. The radiation reflected by the heliostat field is directed towards the receiver, reaching the tube walls and the refractory wall. Equally, the refractory wall irradiates to the sky and to the tubes, whereas the tubes irradiate to the three surfaces: the sky, the refractory wall and the other tube sections, see Figure 3.3. The relative importance of each surface is quantified by the view factors, which have been calculated using the Crossed-Strings Method by Modest (2003).

In order to minimize the error committed using two-dimensional view factors the axial step, Δz, must be as large as possible. Comparing this two-dimensional assumption with a Montecarlo method, the error committed is 17% for $\Delta z = d_{out}/2$, 13% for $\Delta z = d_{out}$ and 4% for $\Delta z = 5d_{out}$. However, to fulfil the hypotheses of homogenous temperature or homogeneous heat flux, the size of the cells must be limited. According to these hypotheses and based on DESOL3 Schwarzbözl & Schmitz (2009), each tube has been divided into 13 vertical blocks, $\Delta z = H/N_b \simeq 13 d_{out}$, that means a low error rate compared with Montecarlo. To facilitate the calculations of the view factors the number of circumferential sections (N_s=37) is calculated dividing the tube in parts close to 5°.

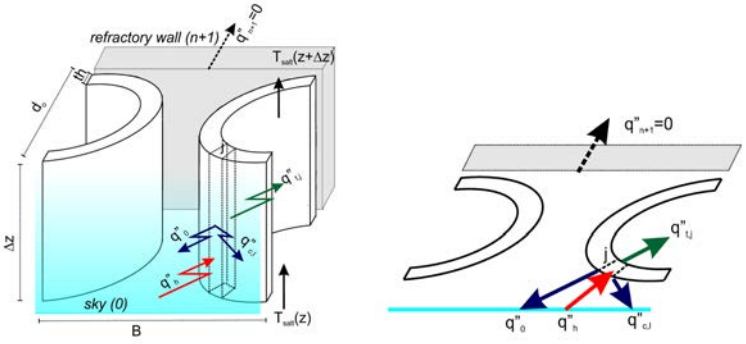

Figure 3.3: Simplified geometry used to simulate the radiative heat transfer in the receiver for the simplified models.

The second hypothesis assumed by the developed models is to consider

all the surfaces involved in the problem as grey surfaces. The Net Radiation Method by Modest (2003), based on the balance of the outgoing radiation travelling from surface to surface (m sub-index) within each axial step, has been used to calculate the radiative heat transfer, see Equation 3.1. The radiation balance equations have been solved individually for each axial step.

$m = 0, 1, ..., N_s + 1$

$$\left[\frac{\delta_{m,0}}{\varepsilon_0} - \left(\frac{1}{\varepsilon_0} - 1\right) F_{m,0}\right] \frac{q''_0}{\sigma} + \sum_{j=1}^{N_s} \left[\frac{\delta_{m,j}}{\varepsilon_j} - \left(\frac{1}{\varepsilon_j} - 1\right) F_{m,j}\right] \frac{q''_j}{\sigma} -$$

$$[\delta_{m,N_s+1} - F_{m,N_s+1}]\, T^4_{N_s+1} = [\delta_{m,0} - F_{m,0}]\, T^4_0 + \sum_{j=1}^{N_s} [\delta_{m,j} - F_{m,j}]\, T^4_j \quad (3.1)$$

$$- \left[\frac{\delta_{m,N_s+1}}{\varepsilon_{N_s+1}} - \left(\frac{1}{\varepsilon_{N_s+1} - 1}\right) F_{m,N_s+1}\right] \frac{q''_{N_s+1}}{\sigma} - F_{m,0} \frac{q''_h}{\sigma} \alpha$$

Where, the refractory wall and the imaginary surface, corresponding to the environment, are represented by the subscripts N_s and 0, respectively, see Figure 3.3. In Equation 3.1, T represents the effective temperature of radiation, δ corresponds to the Kronecker Delta, F symbolizes the view factors between surfaces, ϵ is the emissivity coefficient in the infrared spectrum for the different surfaces, α represents the absorptivity coefficient of the tubes in the visible spectrum and σ is the Stefan-Boltzmann constant.

The conductive losses through the refractory wall, q''_{N_s+1} , are null since the wall has been considered adiabatic. In Equation 3.1 the heat flux reflected by the heliostats, q''_h , is obtained from the radiation map shown in Figure 3.2. In addition, the surroundings temperature, T_0, has been calculated according to Berger *et al.* (1984) as:

$$T^4_0 = \frac{\varepsilon_{sky} T^4_{sky} + \varepsilon_{gr} T^4_{amb}}{\varepsilon_{sky} + \varepsilon_{gr}} \quad (3.2)$$

For the homogeneous temperature model (HTM), an initial estimation of the effective wall temperature, $T(z, \theta)$, is necessary to obtain the heat flux losses to the ambient due to radiation, $q''_0(z)$, the temperature of the refractory wall, T_{N_s+1}, and the heat flux absorbed by the tubes, $q''(z, \theta)$, see scheme in Figure 3.4. Note that the heat absorbed by the tubes, $q''(z, \theta)$, does not take into account the heat lost to the surroundings due to convection, but considers the heat losses by radiation to the surroundings. On the other hand, for the homogeneous heat flux model (HHFM) an initial estimation of the heat

flux absorbed by the tubes without taking into account convective heat losses, $q''(z,\theta)$, is used to obtain the effective wall temperature for the walls of the tubes, , the temperature of the refractory wall, $T(z,\theta)$, and the heat flux losses to the ambient due to radiation, $T_{N_s+1}(z)$, see scheme in Figure 3.5.

Once the radiation power transmitted to the tubes is calculated, the heat losses by convection are included in the model. According to Siebers & Kraabel (1984) the convective heat transfer coefficient for the receiver is a combination between the cross-flow transfer coefficient caused by the wind velocity and the natural convective coefficient, $\overline{h} = (\overline{h}_{fc}^{3.2} + \overline{h}_{nc}^{3.2})^{1/3.2}$. It has been considered that the receiver is equivalent to a rough cylinder whose roughness is given by the tubes. Thus, the forced coefficient depends on the Nusselt and Reynolds numbers based on the receiver diameter, and on the tube relativity roughness, $d_{out}/2/D$. The natural convection coefficient is determined by the Nusselt, Reynolds and Grashof numbers based on the receiver height and by the ambient and tube wall temperature. The convective heat losses, $q''_{c,l}(z,\theta)$, on the different sections of the tubes exposed to the ambient have been calculated with the Newton's law of cooling, Equation 3.3.

$$q''_{c,l}(z,\theta) = \overline{h}(T_{wall}(z,\theta) - T_{amb}) \tag{3.3}$$

Where, $\overline{h}$ is the external convective heat transfer coefficient and T_{wall} corresponds to the external tube wall temperature of each cell of tube, which will be calculated by Equation 3.6.

Under quasi-steady conditions of solar radiation the conductive heat losses through the tube wall in axial and circumferential directions can be neglected compared to the amount of heat absorbed in radial direction, which is at least one magnitude order higher. Therefore, in this study the conduction through the tubes in axial and circumferential directions has not been considered. The thermal specifications of the homogeneous temperature model (HTM) and the homogeneous heat flux model (HHFM) will be described in the following subsections. Both models are solved by an iterative process (see Figures 3.4 and 3.5). Starting at the inlet of the receiver (northern panel), where the temperature of the salt is $T_{salt}(0)$= 290 °C. The simulations progress by means of a finite difference method. The salt temperature at the outlet of each panel is used as an inlet condition for the tube of the next panel. The simulation finishes at the southern panel, where the salt exits at maximum temperature, $T_{salt}(HN_p/N_{fp}$.

3.4.1 Homogeneous temperature model (HTM)

In this model the external wall temperature ,$T_{wall}(z,\theta)$, is initially estimated. As a first approximation the effective wall temperature for radiation at the tube walls, $T(z,\theta)$, is preliminary considered equal to the external wall temperature, and then the receiver heat losses can be calculated as $q_l''(z,\theta) = q_{r,l}''(z,\theta) + q_{c,l}''(z,\theta)$, where $q_{r,l}''$ corresponds to the net radiation losses toward the surrounding (i.e. sky and ground) per unit area referred to the tube surface, defined as $q_{r,l}''(z,\theta) = -q_0''(z)2B/d_{out}\theta$. Subtracting the heat losses to the heat flux reflected by the heliostats based on the radiation map, $q_h''(z)$, it is possible to obtain the heat flux absorbed by the tubes and therefore by the salt, $q_t''(z,\theta)$. This process is described in the scheme shown in Figure 3.4. Note that the difference between q", from Equation 3.1, and q_t'' is that the first one does not take into account the convective heat losses. As q_t'' is the heat flux gained by the molten salt, the energy balance of the whole tube is fulfilled by Equation 3.4.

$$\begin{cases} \int_0^z \int_0^{2\pi} q_t''(z,\theta)\frac{d_{out}}{2} d\theta dz = \int_{T_{salt}(z=0)}^{T_{salt}(z)} \dot{m}_t Cp_{salt} dT_{salt} \\ \int_{T_{salt}(z=0)}^{T_{salt}(z)} \frac{dT_{salt}}{T_{wall}(z,\theta) - T_{salt}(z)} = \int_0^z \int_0^{2\pi} \frac{U}{\dot{m}_t Cp_{salt}} \frac{d_{out}}{2} d\theta dz \\ T_{salt}(0) = 290\ ^{\circ}\mathrm{C} \end{cases} \tag{3.4}$$

Where, Cp_{salt} is the specific heat of the salt at bulk temperature, $T_{salt}(z)$, and $U(z)$ represents the overall heat transfer coefficient, which connects the external surface of the tube wall to the bulk temperature of the salt, $U(z) = \left(\frac{d_{out} ln(d_{out}/d_{int})}{2k_t} + R_{foul} d_{out}/d_{int} + \frac{d_{out}/d_{int}}{h_{salt}}\right)^{-1}$, where R_{foul} is the fouling coefficient of Petukhov (1970), k_t corresponds to the tube thermal conductivity coefficient which depends on the temperature and h_{salt} is the internal convective coefficient which depends on the salt properties at bulk temperature, $h_{salt}(z) = Nu(z)k_{salt}/d_{int}$.

According to Yang & Fan (2012), the value of the internal Nusselt number for the tubes of an external receiver is almost unchanged in circumferential direction for Reynolds and Prandtl numbers around 17,000 and 12, respectively. Then, solving Equation 3.4, the evolution law of the bulk temperature of the salt inside each of the blocks, in which the receiver tubes have been divided,

can be obtained; it has been represented by Equation 3.5.

$$T_{salt}(z) = \overline{T_{wall}}(0) - (\overline{T_{wall}}(0) - T_{salt}(0)) \exp^{-NTU \frac{z}{HN_p/N_{fp}}} \tag{3.5}$$

Where $\overline{T_{wall}}$ is the average temperature of an annular section of tube, defined as $\overline{T_{wall}}(z) = 1/(2\pi) \int_0^{2\pi} T_{wall}(z,\theta) d\theta$, and $NTU(z)$ represents the number of net transfer units expressed as $NTU(z) = U(z)\pi d_{out} z/(\dot{m}_t Cp_{salt})$. Once the salt temperature evolution along the receiver is known it is necessary to recalculate the external wall temperature and the effective temperature of radiation according to the results obtained, see Equations 3.6 and 3.7.

$$T_{wall}(z) = \frac{q_t''(z,\theta)}{U(z)} + T_{salt}(z) \tag{3.6}$$

$$T^4 = \frac{1}{z} \int_0^z \left(T_{salt}(z) + \frac{q_t''(z,\theta)}{U(z)} \right)^4 dz \tag{3.7}$$

The process, from Equation 3.4 to Equation 3.7, has to be repeated until the difference between the values of the tube wall temperature for two consecutive iterations (TOL1) is lower than 10^{-3}. Figure 3.4 shows the iterative algorithm followed by HTM to solve the whole receiver.

3.4.2 Homogeneous heat flux model (HHFM)

In order to apply the model of homogeneous heat flux it is necessary to know the incident solar flux at the receiver, $q_h''(z)$. Initially it will be assumed null radiative and convective heat losses in the receiver. Therefore, the heat flux absorbed by the tubes is equivalent to the solar power reflected by the heliostats, $q_t''(z,\theta) = q_h''(z)$. In this case the energy balance in the tubes, Equation 3.4, must be integrated in a different way than for HTM to obtain the salt temperature along the tubes of the receiver, see Equation 3.8.

$$T_{salt}(z) = T_{salt}(0) + \int_0^z \int_0^{2\pi} \frac{q_t''(z,\theta)}{\dot{m}_t Cp_{salt}} \frac{d_{out}}{2} d\theta dz \tag{3.8}$$

In this case it is possible to calculate the evolution of the external tube wall temperature and the effective temperature of radiation using the same expressions than for HTM, Equations 3.6 and 3.7. Then, applying the new

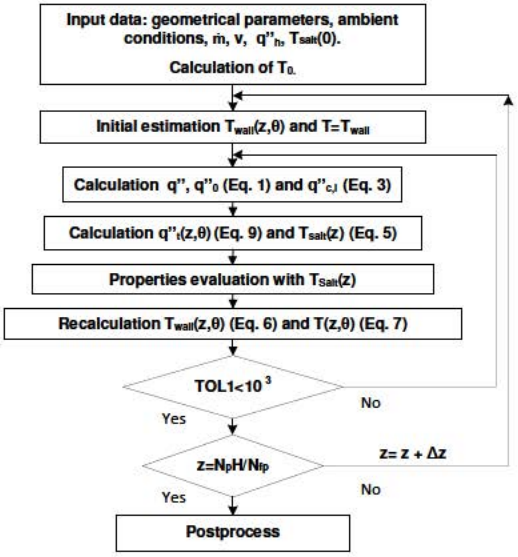

Figure 3.4: Calculation algorithm for HTM.

effective temperature of radiation in Equations 3.1 and 3.3, the heat losses and the heat flux absorbed by the salt can be recalculated. This process is repeated until the difference between the values of the heat flux gained by the molten salt for two consecutive iterations (TOL2) is lower than 10^{-3}. Figure 3.5 represents the calculus algorithm for this iterative process, which solves the whole receiver assuming homogeneous heat flux.

3.4.3 Standard model (SM): no temperature variations in circumferential direction

This subsection explains the calculations followed in a simplified model that does not take into account tube wall temperature variations in circumferential direction. As this simplification is commonly employed in the literature by authors as Singer *et al.* (2010) and Jianfeng *et al.* (2010); this model will be named as standard model (SM).

The standard model only considers a single mean wall temperature for each axial step, Δz. Instead of using variables as a function of the coordinates z, θ this model uses all its variables as an only function of the coordinate z (i.e. old variable $T(z,\theta)$ is transformed to $T(z)$). This fact modifies the Equations 3.1,

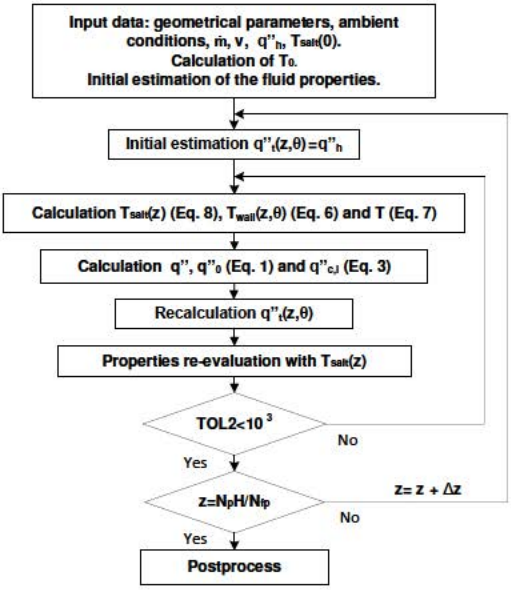

Figure 3.5: Calculation algorithm for HHFM.

3.3, 3.4, 3.6, 3.7, and 3.8 and makes that sub-index in Equation 3.1 can only take the values 0, 1 and 2.

This standard model simplifies the equations and the problem resolution. The number of cells in the tubes has been reduced because only the axial variations of temperature and heat flux are considered in the discretization of the receiver. Figure 3.6 shows the iterative scheme of the process following by SM to solve a whole receiver, which is equivalent to the scheme following by HHFM without considering circumferential variations of the problem variables.

3.5 CFD: Numerical simulations

A numerical simulation of the central receiver was carried out using the commercial code, ANSYS Fluent. The results of this simulation have been compared to the simplified models introduced in Section 3.3 in order to proof that the considerations of bi-dimensional problem, constant internal convective coefficient with the angle, and circumferential variations of the tube wall temperature, assumed by the simplified models, lead to results very close to the ones obtained

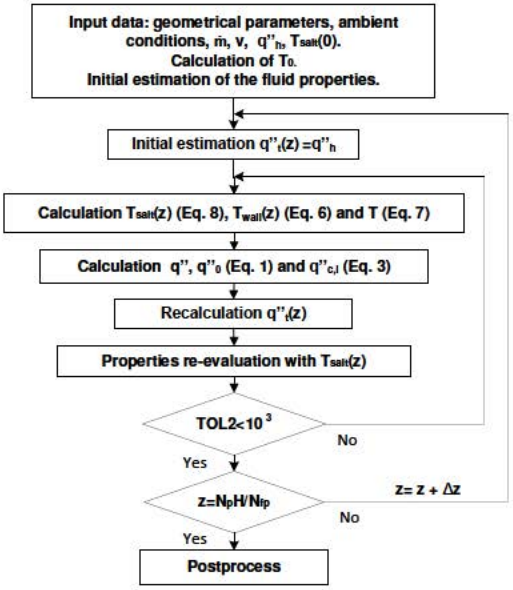

Figure 3.6: Calculation algorithm for SM.

with the fully three-dimensional and highly complex CFD model.

In CFD simulation the mass, momentum and energy equations were solved using a control volume technique. A pressure correction based model was used to solve the Navier-Stokes equations. To reduce the calculation time only one representative tube per panel was simulated. Each tube was calculated separately, using the conditions at the outlet of each tube as the inlet conditions for the tube of the next panel downflow. The air surrounded the tubes was simulated as an ideal gas. Fouling inside the tubes was also taken into account; the fouling thickness was of 90 μm and the resistivity is R_{foul}, see Table 3.1.

The computational domain used to simulate the flow and the radiation for each tube, occupies a rectangular cuboid of dimensions: 7.4 m x 0.0442 m x 0.5232 m ($HxBxL$), see Figure 3.7. The domain includes the tube, the reradiating wall of the tower receiver and the air surrounding the tube. The domain was discretized using an unstructured mesh and hexahedrical cells. Due to the large aspect-ratio of the domain the size of the grid is of order of 10^5 cells. Tests were performed to check that the grid was suitable for this problem by mesh-refinement. For example, comparison of results from a sequence of

successively refined meshes of 103,400, 215,400, 439,400 and 1,335,400 cells, gave an estimated numerical accuracy of 0.2% for the mean salt temperature and 4% for the maximum wall temperature when using the grid of 439,400 cells. Due to its fine compromise between accuracy and computational cost, the grid of 439,400 cells was selected for the CFD results presented in the study.

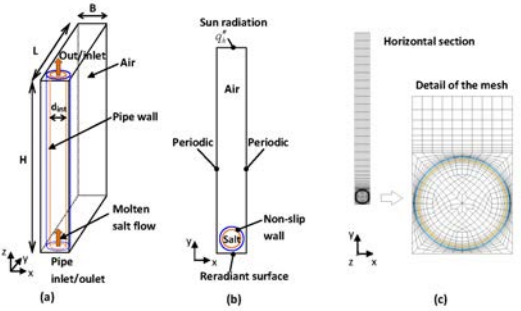

Figure 3.7: (a) Sketch of the computational domain for CFD simulations. (b) Detail of a transversal cut of the computational domain for CFD. (c) Detail of the computational mesh in a transversal cut. (In the figure the mesh density has been lowered for clarity reasons).

To simulate the radiation between the tube surface, the reradiating wall and the surroundings, the Discrete Ordinates model was chosen. The turbulent model used to simulate the molten salt behaviour inside the tubes and the air outside the tubes was Standard k-epsilon. Enhanced Wall Treatment was used to solve the flow near the walls. An implicit method was selected to solve the Navier-Stokes and the energy equations, and a second-order discretization was chosen for the convective terms. A scheme from the family of the SIMPLE algorithms was used for the coupling of the pressure and velocity of each fluid.

At the inlet of each tube the velocity and temperature of the molten salt was imposed. No-slip condition was assumed on the walls of the tubes. Pressure-outlet at the outlet of the tube and pressure-inlet at the front side of the cuboid were imposed. To simulate the radiation received by each tube, an effective external blackbody temperature, $T_{cb}(z)$, was also assumed on N_s=13 axial blocks of the front side of the cuboid, so that $\sigma T_{cb}^4(z)$ reproduced the values of the irradiation map of Figure 3.2. That means that the temperature of the equivalent blackbody was a function of the height as well as the panel considered. Implicit in this equivalent blackbody temperature is the fact that

the irradiation from the heliostats is much higher than from atmosphere and the land. The CFD simulations initially started with all the fluids at rest and ambient temperature, excepting for the values set at the boundary conditions.

This simulation was initially validated with two kinds of tests. A test was performed imposing uniform temperature at all the surfaces and the simulation results verified against the theoretical view factors of an infinite array of tubes near an infinite plane Modest (2003). Only a 4% of discrepancy was found between the CFD radiation calculations and the theoretical view factor. In another test the pressure drop and coefficient of convection obtained in the simulation were satisfactorily compared with the semi-empirical correlations of Petukhov and Gnielinski for turbulent flows (Lienhard & Lienhard (2008)). In particular, in all the cases the mean discrepancy between the CFD and experimental Nusselt number was smaller than the intrinsic 25% accuracy of the experimental Nusselt correlations for turbulent flows with transport properties highly dependent on temperature Lienhard & Lienhard (2008).

3.6 Results

In this section a receiver configuration under different work conditions has been simulated by means of CFD simulation, two simplified models explained in previous sections, HTM and HHFM, and a standard model, SM. The main goal of this section is to demonstrate if the numerous initial hypotheses of the simplified models against the more spatially resolved and three-dimensional CFD model under quasi-steady work conditions representative of central solar receiver produce similar results. And then, the simplified models could be used in the study of receiver designs. The different cases studied in this section are shown in Table 3.2; remember that it has been assumed steady state conditions for all the cases studied.

Figure 3.8 shows the evolution of the tube wall temperature at $\theta = 0^\circ$ and the bulk temperature of the salt calculated with HTM and HHFM for case A. Both simplified models approach to the same solution when a sufficiently fine mesh at the outer tube is used. If the provided solar flux-map is a coarse mesh, HHFM is a more appropriate model than HTM because of the heat transfer process is dominated by the incoming solar flux instead of the internal heat transfer coefficient. The absorbed radiation is lowly dependent on the heat transfer coefficients, almost for the operating conditions analysed. On the other hand, for a fine mesh HTM is preferred because this boundary condition only

reflects the thermodynamic equilibrium condition. As, with the chosen mesh, the results of both models are practically identical, in the following subsections only HTM (and not HHFM) will be represented in order to simplify and clarify the figures.

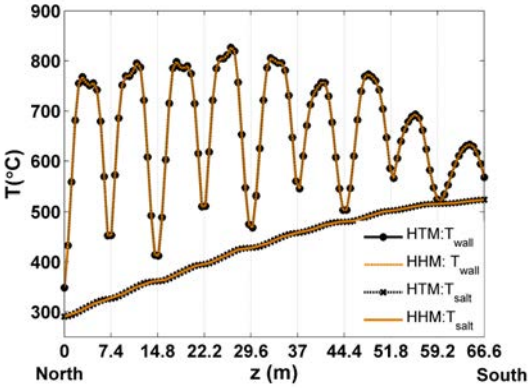

Figure 3.8: Evolution of the maximum tube wall temperature (θ=0°) and the salt bulk temperature evolution obtained with HTM and HHFM for Case A conditions. Black lines for HTM and cyan lines for HHFM.

Note that in Figure 3.8 the bulk salt temperature increases from 290 °C (at the inlet of the receiver, z=0 m) up to 524 °C (at the exit of the receiver, z=66.6 m). However, the evolution of the tube wall temperature at θ=0° is not as simple; it is influenced by the molten salt temperature and by the heat flux received from the heliostat field. Then, the maximum tube wall temperature does not increase axially. The heat flux is, indeed, maximum at the northern panel (first panel), and is minimum at the southern panel. Furthermore, the heat flux is not constant, nor circumferentially, nor axially (see Figure 3.2). Therefore, the axial wall temperature at θ= 0° is approximately maximum at the middle of each tube and minimum at its edges, similarity to the heat flux. Since the heat transfer fluid increases its temperature, as it flows through the tubes, its ability to refrigerate the tube walls decreases with the distance from the inlet, hence, in Figure 3.8 the variations of the maximum tube wall temperature show the balance between the decreasing heat flux and the decreasing refrigeration power of the salt. It can be seen that the maximum wall temperature withstand by the tubes is around 800 °C, it is at the middle of the fourth panel, where the solar flux is not the highest.

At the same time, it can be observed a different behaviour between odd and even panels. It is caused by the different direction of the mass flow rate and by the non-symmetry of the radiation map.

3.6.1 External temperature distributions of the tube wall

Figures 3.9 and 3.10 show the axial and circumferential distributions of the external tube wall temperature for the first and fourth panels of the receiver, respectively, and for conditions of case A. The results represented have been obtained with HTM and CFD simulations. The first and fourth panels have been chosen to be represented since they are the panels with the highest heat flux and the maximum tube wall temperature, respectively (see Figures 3.2 and 3.8). In addition, one panel is odd (upstream) and the other even (downstream), that lets appreciate the two different behaviours of the tube temperature in a receiver.

In Figures 3.9 and 3.10 the angle $\theta = \pm 180°$ corresponds to the tube part exposed to the refractory wall and $\theta = 0°$ represents the tube side exposed to the ambient and to the solar radiation. The temperature of the tube wall is minimum at $\theta = \pm 180°$, where the tube wall temperature is strongly influenced by the salt temperature. In this zone, the tube wall temperature increases from the inlet of the tubes to the outlet, see the salt temperature evolution in Figure 3.8.

The tube wall temperature suddenly increases at 90°, being maximum at $\theta = 0°$). In this zone the tube wall temperature is strongly influenced by the heat flux and its shape is similar to the solar radiation received. Then, the tube wall temperature is especially high close to the middle length of the tubes and minimum in their edges. Due to the non-symmetry of the radiation map in axial direction, in the first panel (upstream) the tube wall temperature at $\theta = 0°$ is lower at the inlet of the tubes than at the outlet, however at this angles in the fourth panel (downstream) the wall temperature at the inlet of the tube is higher than at the outlet.

In panel one (Figure 3.9) the inlet salt temperature is the same for both models, and at the rear part of the tubes the difference between models for tube wall temperature is negligible. However, at the front side of the tubes the differences are noticeable, especially at the centre of the tube length where the heat flux is maximum. Here, the wall temperature estimated with HTM is higher than with CFD simulations; the latter one considers dissipative effects in the tube walls and takes into account 3D effects in the view factors distributing

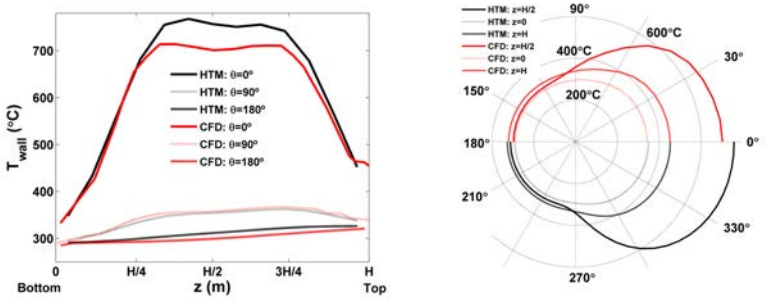

(a) (b)

Figure 3.9: External wall temperatures of the representative tube of the first panel, for Case A conditions. (a) Axial profile at different circumferential positions. (b) Circumferential profile at different heights. Red lines correspond to CFD and black lines to HTM.

more homogeneously the heat flux and then smoothing the tube wall temperature. However, the maximum relative difference in the calculation of the tube wall temperature for the first panel is lower than 2.5%.

In the fourth panel (Figure 3.10) the inlet temperature of the salt for the simplified model and CFD simulations are different due to the differences in the previous panels and then the comparison is more complex; nevertheless it is important to study this panel because it has the maximum wall temperatures. As the wall temperature is strongly influenced by the salt temperature, the inlet temperature of the salt depends on the panel, 290 °C for the first panel and close to 390 °C for the fourth panel. Then, the tube wall temperature at the inlet of the fourth panel must be higher than in the first panel. Since the tube wall temperature is also influenced by the heat flux received by the tubes, the maximum wall temperature at the front side of the tubes is displaced axially with respect to the wall temperature of the first panel. Despite that, the results obtained are similar to those obtained for panel one, and the maximum relative difference in the calculation of the tube wall temperature of panel four, using HTM or CFD, is 2.5%.

3.6.2 Outlet salt and maximum tube wall temperatures

Figures 3.11 and 3.12 represent the outlet salt temperature and the highest external wall temperature of each representative tube (i.e. panel) for one flow

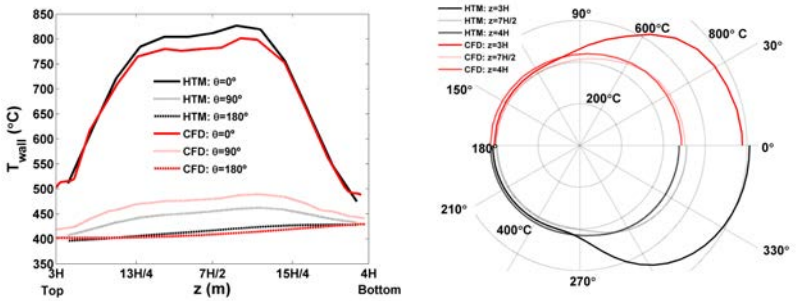

(a) (b)

Figure 3.10: External wall temperatures of the representative tube of the fourth panel for Case A conditions. (a) Axial profile at different circumferential positions. (b) Circumferential profile at different heights. Red lines correspond to CFD and black lines to HTM.

path. They have been obtained with HTM, SM, and CFD simulations. Starting in the first panel of one flow path (north side) and finishing in the last panel (south side).

In Figure 3.11 the outlet salt temperature and the maximum wall temperature of each panel are presented for different wind velocities (Cases A, B and C); while in Figure 3.12 these variables are represented for different mass flow rates (Cases A, D and E).

In Figures 3.11(a) and 3.12(a), the outlet salt temperature increases in each panel, although its slope decreases around the fifth panel. This slope decrease in the temperature growth is related with the heat absorbed by the salt in the tubes; the heat flux absorbed by the salt remains almost constant from the first to the fourth panel (diminishing slightly); in addition, there is an important drop on the heat absorbed by the salt in the sixth and seventh panel, see Figure 3.13(a).

Figures 3.11(a) and 3.12(a) also show that the salt outlet temperature is slightly higher for CFD simulations than for the simplified models, and these differences are almost constant for every panel. In CFD simulations the energy is better distributed, producing a decrease in the maximum tube wall temperature and in the heat losses to the ambient. Then, the salt temperature and the receiver efficiency increase. The receiver efficiency is defined as the ratio between the heat absorbed by the fluid and the incident heat radiation

($\eta = \dot{Q}_t/\dot{Q}_h$), and its values for the different cases can be seen in Table 3.3.

The maximum salt temperature difference between HTM and CFD simulations is approximately 17 °C at the exit of the receiver ($z = HN_p/N_{fp}$). This difference could be considered negligible compared with the broad work temperature range, and represents a relative discrepancy of 7.5% taking into account the salt temperature increment along the receiver. The salt outlet temperature difference between the simplified models and CFD is higher than between SM and CFD model; being the discrepancy in the calculus of the bulk temperature of the salt for SM lower than 7%. The maximum difference reach between HTM and CFD occurs for case C (maximum wind velocity) and it could be caused by a difference in the calculation of external convective coefficient; the minimum difference occurs for case D (minimum mass flow rate), when the internal convective coefficient is minimum, it can be seen in Table 3.3.

For Figures 3.11(b) and 3.12(b), recall that the maximum external wall temperature is always located on the front part of the tubes ($\theta = 0°$) and approximately in the middle length of the tubes. This maximum temperature on the outer wall of the tubes is related with the heat flux absorbed by the tubes and the bulk temperature of the salt. Since the heat flux absorbed by the tubes is practically the same in the panels one to four and the temperature of the salt is higher in panel four, the temperature wall at this panel has to be the higher. Notice that this exactly what happens in the panels six and seven.

Paying attention to the tube wall temperature the differences between CFD simulations and the simplified models are around 20 °C, that represents a 2.5% of deviation, being the maximum difference for case C and the minimum for case E. However, comparing any of these models with SM the tube wall temperatures are at least 200 °C smaller for SM, which represents a deviation of 30%, as shown Table 3.3. Moreover, the maximum tube wall temperature for SM is at the seventh panel instead of at the fourth.

Then, using the SM, that does not consider the circumferential variations of the temperature (i.e. Singer *et al.* (2010) and Jianfeng *et al.* (2010)), leads to a good prediction of the salt temperature and to the receiver efficiency, but to an inaccurate prediction of the tube wall temperature resulting in lower values of the maximum temperature at the tube external surface (30% lower).

In addition, the internal tube wall temperature, calculated from the external tube wall temperature using Equation 3.9, is the critical point of design of a receiver, Rodríguez-Sánchez & Santana (2014). An internal tube wall temperature higher than 620 °C increases exponentially the salt decomposition and

the corrosion rate of the tubes jeopardizing the integrity of the receiver. Then, as SM undervalues the maximum internal tube wall temperature, it is unable to carry out an appropriate receiver design (i.e. materials, tube thickness and diameter of the tubes). Nevertheless, consider circumferential temperature variations in the tubes (HTM and HHFM) seems to be an appropriate method for the receiver design.

$$T_{wall,int}(z,\theta) = T_{wall}(z,\theta) - \frac{1}{2} q''_t(z,\theta) \frac{d_{out} ln\left(\frac{d_{out}}{d_{int}}\right)}{k_t} \tag{3.9}$$

Despite of SM is not capable of predicting the tube wall temperature, SM correctly calculates the salt temperature and the receiver efficiency. It occurs only for the particular conditions of the receiver studied; it has been assumed grey surfaces and that the emissivity of the Black Pyromark varies with the tube wall temperature. Then, if the tube wall temperature decreases the emissivity of the tubes decreases and its reflectivity increases. The increment of the reflectivity is compensated for the reduction of heat losses produced by a minor wall temperature, being the receiver efficiency the same than for CFD or simplified models. Then, in this particular case, SM could be used to calculate the preliminary designs of the heliostat field but it cannot predict a proper design of a receiver.

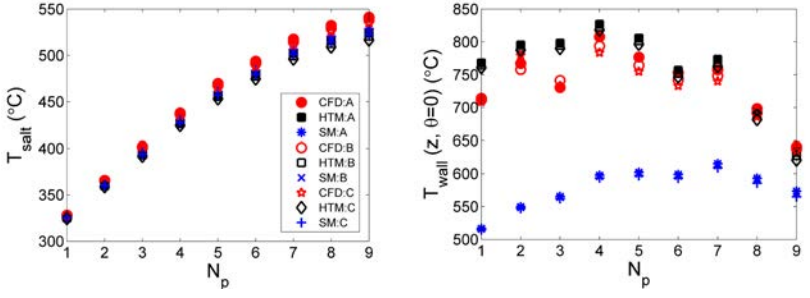

(a) (b)

Figure 3.11: Results of the sensitivity analysis to wind velocity. (a) Outlet salt temperature for each panel. (b) Maximum external wall temperature for each panel. Red symbols for CFD, black symbols for HTM and blue symbols for SM.

Another result obtained from Figure 3.11 is that the outlet salt temperature and the tube wall temperature for the cases with wind and without wind are

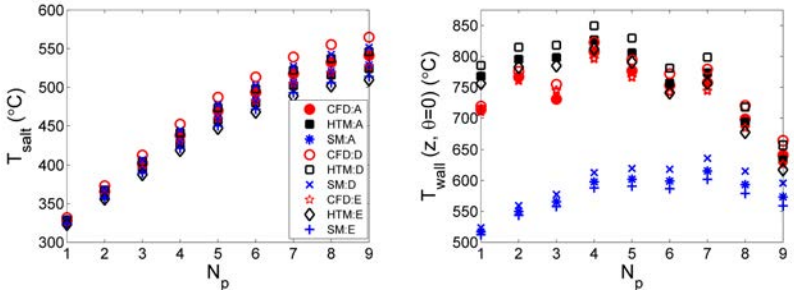

(a) (b)

Figure 3.12: Results of the sensitivity analysis to the mass flow rate in the tubes. (a) Outlet salt temperature for each panel. (b) Maximum external wall temperature for each panel. Red symbols for CFD, symbols lines for HTM and symbols lines for SM.

quite similar; this implies that the heat dissipated to the ambient by convection is relatively low compared with the solar net flux radiation.

The sensitivity of the results to variations in the mass flow rate of the salt (Cases A, D and E) is studied in Figure 3.12. Increasing the mass flow rate of molten salt in the tubes, the outlet salt temperature and the tube wall temperature are reduced. Then, the salt convective coefficient increases and the receiver efficiency improves. The differences between CFD and HTM are not higher than the differences observed when changing the wind velocity.

In Table 3.3 can be seen that the tube wall temperature obtained with CFD and the simplified models is higher than 800 °C, this temperature is excessively high for a receiver, but this study is focused on prove that the predictions of the developed models are appropriate, and not in the receiver design. Then, the most unfavourable conditions have been studied; as higher is the solar heat flux more pronounced will be the difference between models.

3.6.3 Heat flux absorbed by the salt

Finally, the heat flux absorbed by the salt has been analysed in this subsection. Figure 3.13(a) shows the heat flux absorbed for the representative tube of each panel in axial direction for CFD, HTM and SM; for cases A and C, which represent a wind velocity of 0 m/s and 15 m/s , respectively. Similar trends are obtained with Cases B, D and E and have not been represented in order to

Table 3.3: Efficiency, highest tube wall temperature and outlet salt temperature for the five cases studied and for the different models employed: CFD, HTM, HHFM, and SM.

Parameters	**Model**	**Case**				
		A	**B**	**C**	**D**	**E**
η [-]	CFD	0.85	0.84	0.83	0.85	0.86
	HTM	0.79	0.78	0.77	0.79	0.80
	$HHFM$	0.79	0.78	0.77	0.79	0.80
	SM	0.81	0.80	0.79	0.81	0.81
$T_{\text{salt}}\left(\frac{HN_p}{N_{fp}}\right)$ [°C]	CFD	541.2	538.1	534.4	564.8	526.6
	HTM	524.1	520.7	516.7	546	509.7
	$HHFM$	524.1	520.6	516.6	545.9	509.6
	SM	528.7	525.6	521.9	551.6	513.9
$T_{\text{wall}}\left(\frac{4H}{N_{fp}}, 0\right)$ [°C]	CFD	807.7	793.7	783.5	822.8	796
	HTM	826.8	822.8	818	849.7	811.9
	$HHFM$	826.8	822.7	817.9	849.6	811.8
	SM	597.7	595.7	593.4	612.7	588

simplify. The figure shows the heat flux absorbed by one flow path, from north to south.

While Figure 3.2 shows the heat flux image that is received by the front part of the tubes (θ= 0°), Figure 3.13 represents, in axial direction, the heat flux integration in the whole perimeter of the tubes when the heat losses to the surroundings have been subtracted. Thereby, the heat flux magnitude difference between both figures. In Figure 3.13(a) can be noticed that the heat flux shape is so similar to the maximum external wall temperature of the tubes, maximum approximately in the centre of the tubes and minimum at the edges. Nevertheless, the maximum heat flux absorbed by the tubes corresponds to the northern panels of the receiver and the minimum to the southern panels. For case A, without wind, the heat flux obtained with CFD simulations is slightly higher than the obtained with the HTM or SM, and slightly lower for case C, maximum wind. This difference is more important in the middle of the tubes, where the heat flux is maximum.

Figure 3.13(b) shows a detail of the centre of the tubes for panels third and fourth. It can be noticed that the influence of the wind is more noticeable for CFD simulations than for the simplified models. Despite of that, the maximum

difference between cases A and C is not significant, leading to only $2x10^3$ W/m^2 of difference. This confirms that the main heat losses in the receiver are due to radiation and not to convection. The maximum heat flux difference obtained between HTM and CFD simulations is lower than 6% and is located in the fourth panel.

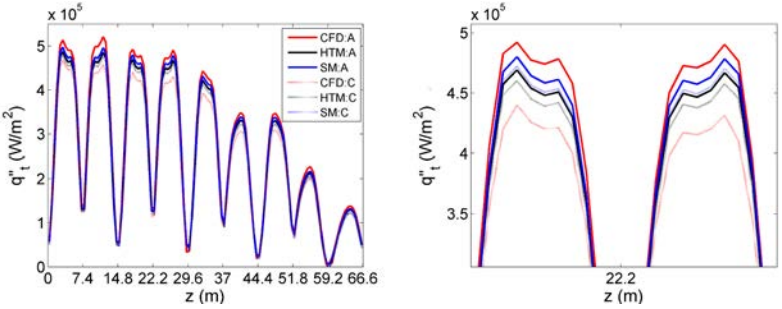

(a) (b)

Figure 3.13: Heat fluxes absorbed by the salts. (a) Heat flux profiles along one flow path of the receiver. (b) Zoom of the third and fourth panel heat fluxes. Red lines for CFD, black lines for HTM and blue lines for SM.

3.6.4 Simulation times and number of iterations

The main information about the computational time and the number of iterations of all the models proposed in this study is encompassing in Table 3.4. The represented values are the approximate mean value for a complete receiver simulation of all the cases analysed, using a standard PC equipped with an Intel quad-processor and 4 GB of RAM.

Table 3.4: Mean computational time and number of iterations of a complete receiver simulation for all the cases studied (CFD and simplified models).

Parameters	CFD	Simplified Modeles
# Cells per tube	$439,400$	481
# Iterations	10^4	6
# Time [s]	$3 \cdot 10^4$	15

It can be noticed that the number of cells and the time to complete a whole receiver simulation is several order of magnitude higher for CFD simulations

than for the simplified models proposed. CFD does not assume as many hypotheses in the calculations of a receiver; instead it solves the energy balance for the internal and the external fluid and for the tube walls using a large computational domain. For CFD simulation, the computational domain used to simulate the flow and the radiation for each tube, occupies a rectangular cuboid that includes the tube, the reradiating wall and the air surrounding the tube. Then, CFD simulations are not recommended to be used for initial designs of the receiver, when a lot of parameters (N_p, d_{int}, d_{out}, B, H, D) have to be taken into account and numerous simulations have to be launched.

In addition, the results obtained with CFD simulations and with the simplified models are quite similar. The tube wall temperature differs less than 2.5%, and the salt temperature and the heat flux absorbed by the salt differ around 7%. As the computational cost is lower for the simplified models than for CFD simulations, HTM and HHFM will be the most appropriate models to carry out and analysis and optimization of the previous design of the receivers.

3.7 Conclusions

In this study, two new simplified models have been developed to calculate the thermal properties of an external receiver during the steady state operation. Both models consider circumferential temperature variations and heat flux variations but, one model assumes homogeneous temperature boundary condition, HTM, and the other one assumes homogeneous heat flux boundary condition, HHFM.

Different cases, varying the mass flow rate and the wind velocity on the receiver, have been studied in order to probe the sensitivity of the models respect to these factors. The results of HTM and HHFM have been compared with a SM, reported in the literature, which does not consider circumferential variations of the wall temperature. The three simplified models show similar results for the temperature evolution of the molten salt because the heat flux absorbed by the tubes in average is mainly determined by the irradiation from the heliostat field. However, the maximum wall temperatures obtained using HTM and HHFM are higher to the temperatures predicted when the circumferential variations are not considered (SM). Since the inner tube wall temperature is the critical point of design to predict problems like the corrosion rate of the tubes and the salt decomposition, the SM is unable to carry out an appropriate receiver design (i.e. materials, tube thickness and diameter of the tubes).

Hence, we can conclude that an appropriate receiver design must be carried out considering circumferential temperature variations at the tubes.

In addition, the results of the models have been compared with CFD simulations. The results of the new models and the CFD simulations are in good agreement. The difference in the wall temperature, outlet salt temperature and absorbed heat flux is always smaller than 7%. This similarity validates the hypotheses assumed in the new simplified models, including the axial and circumferential discretization selected and the non 3D effect consideration. The advantage of the new proposed models, with respect to the CFD simulations, is that they lead to similar results but they introduce a dramatic decreasing in the computational time, mandatory for receiver design purposes. Therefore, the simplified models presented here open the possibility of simulating the whole receiver, including all the tubes of a panel. In these integral models, the salt and tube wall temperatures of the whole receiver could be solved in one step and with a low number of iterations. In summary, the simplified models developed in this work could be a useful tool for the estimation of the external receiver performance and for design purposes, allowing the thermal and mechanical characterization of external receivers in a fast and simple way.

It has seen that the differences between models are almost equal for all the cases studied. In addition, it has been checked that there are not noticeable differences between the cases with and without wind, it confirms that the main heat losses in the receiver are due to radiation and not to convection. Finally, an increase of the mass flow rate reduces the outlet salt temperature and the tube wall temperature and improves the receiver efficiency.

Nomenclature

B	Tube pitch [m]
C_p	Specific heat [J/kg° C]
D	Receiver diameter [m]
d	Tube diameter [m]
F	View factor [-]
H	Receiver/ Tube length [m]
h	Convective coefficient [W/m^{2}K]
k	Conductive coefficient [W/mK]
L	Cuboid wide [m]
$\dot{m}$	Mass flow rate [kg/s]

N	Number of elements [-]
Nu	Nusselt number [-]
NTU	Number of net transfer unit [-]
P	Pressure [bar]
q''	Heat flux [W/m^2]
R_{foul}	Fouling resistance [m^2K/W]
T	Temperature [° C]
$TOL1$	Temperature tolerance [° C]
$TOL2$	Heat flux tolerance [W/m^2]
U	Global transfer coefficient [W/m^2K]
S	Flow surface [m^2]
v	Velocity [m/s]
z	Flow path coordinate [m]

Greek letters

α	Solar absorptivity [-]
Δz	Axial step [m]
δ	Kronecker delta [-]
ϵ	Emissivity [-]
ϕ	Relative humidity [%]
η	Thermal efficiency [%]
θ	Circumferential coordinate [°]
σ	Stefan-Boltzmann constant [W/m^{2}K^4]

Subscripts

amb	Ambient
b	Blocks
c	Convection
cb	Cuboid
fc	Forced convection
fp	Flow path
gr	Ground
h	Heliostat
int	Internal
l	Heat losses

N_s+1	Refractory wall
nc	Natural convection
out	External
p	Panel
r	Radiation
s	Sections
t	Tube
0	Surroundings

Abbreviattions

CSP	Concentrated solar power
HHFM	Homogeneous heat flux model
HTM	Homogeneous temperature model
HTF	Heat transfer fluid
SM	Standard model
SPT	Solar power tower

References

ASME 2011 ASME Boiler and Pressure Vessel Code, Section II - Materials. *Tech. Rep.*. American Society of Mechanical Engineers, New York.

Augsburger, Germain & Favrat, Daniel 2013 Modelling of the receiver transient flux distribution due to cloud passages on a solar tower thermal power plant. *Solar Energy* 87, 42–52.

Berger, X., Buriot, D. & Garnier, F. 1984 About the equivalent radiative temperature for clear skies. *Solar Energy* 32 (6), 725–733.

Falcone, P.K 1986 *A handbook for solar central receiver design*. Livermore, California: Sandia National Laboratories.

Garbrecht, Oliver, Al-Sibai, Faruk, Kneer, Reinhold & Wieghardt, Kai 2013 CFD-simulation of a new receiver design for a molten salt solar power tower. *Solar Energy* 90, 94–106.

Irfan, Mohammad a. & Chapman, Walter 2009 Thermal stresses in radiant tubes due to axial, circumferential and radial temperature distributions. *Applied Thermal Engineering* 29 (10), 1913–1920.

Jianfeng, Lu, Jing, Ding & Jianping, Yang 2010 Heat transfer performance of an external receiver pipe under unilateral concentrated solar radiation. *Solar Energy* 84 (11), 1879–1887.

Kistler, B.L. 1986 A User's Manual for DELSOL3: A Computer Code for Calculating the Optical Performance and Optimal System Design for Solar Thermal Central Receiver Plants. *Tech. Rep.*. Sandia National Laboratories, Albuquerque.

Kolb, G.J.; Ho, C.K.; Mancini T.R. & Gary, J.A. 2011 Power Tower Technology Roadmap and Cost Reduction Plan. *Tech. Rep.* April. Sandia National Laboratories, Sandia National Laboratories, Albuquerque.

Lata, Jesús M., Rodríguez, Manuel & Álvarez de Lara, Mónica 2008 High Flux Central Receivers of Molten Salts for the New Generation of Commercial Stand-Alone Solar Power Plants. *Journal of Solar Energy Engineering* 130 (2), 1–5.

Lienhard, J.H. IV & Lienhard, J.H. V 2008 *A Heat Transfer Textbook*, third edit edn., *McGraw-Hill Higher Education*, vol. 82. Cambridge, Massachusetts: Phlogiston Press.

Lim, Sehwa, Kang, Yongheack, Lee, Hyunjin & Shin, Seungwon 2014 Design optimization of a tubular solar receiver with a porous medium. *Applied Thermal Engineering* 62 (2), 566–572.

López-González, D., Valverde, J.L., Sánchez, P. & Sanchez-Silva, L. 2013 Characterization of different heat transfer fluids and degradation study by using a pilot plant device operating at real conditions. *Energy* 54, 240–250.

Modest, F Michael 2003 Radiative Heat Transfer. In *Radiative Heat Transfer*, Second edi edn. (ed. Elsevier Science), chap. 5. RADIATI, pp. 162–197. New York, San Francisco, London.

Petukhov, B.S. 1970 *Heat Transfer and Friction in Turbulent Pipe Flow with Variable Physical Properties*, , vol. 6. Moscow (USSR).

Rodríguez-Sánchez, M.R.; Soria-Verdugo, A.; Almendros-Ibáñez J.A; Acosta-Iborra A. & Santana, D. 2014 Thermal design guidelines of solar power towers. *Applied Thermal Engineering* 63 (1), 428–438.

Schwarzbözl, P.; Pitz-Paal, R. & Schmitz, M. 2009 Visual HFLCAL - A Software Tool for Layout and Optimisation of Heliostat Fields. In *SolarPACES*. Berlin, Germany: SolarPACES.

Siebers, D L & Kraabel, J S 1984 Estimating Convective Energy Losses From Solar Central Receivers. *Tech. Rep.*. Sandia, Livermore.

Singer, C.; Buck, R.;, Pitz-Paal, R. & MuÌĹller-Steinhagen, H. 2010 Assessment of Solar Power Tower Driven Ultrasupercritical Steam Cycles Applying Tubular Central Receivers With Varied Heat Transfer Media. *Journal of Solar Energy Engineering* 132 (4), 041010: 1–12.

Slemp, W. S. & Wade, W. R. 1962 A method for measuring the spectral normal emittance in air of a variety of materials having stable emittance characteristics. *Tech. Rep.*. NASA, Hampton, VA, United States.

Xu, Chao, Wang, Zhifeng, Li, Xin & Sun, Feihu 2011 Energy and exergy analysis of solar power tower plants. *Applied Thermal Engineering* 31 (17-18), 3904–3913.

Yang, X.; Yang, X.; Ding J.; Shao-Y. & Fan, H. 2012 Numerical simulation study on the heat transfer characteristics of the tube receiver of the solar thermal power tower. *Applied Energy* 90 (1), 142–147.

Zavoico, A.B. 2001 Solar Power Tower: Design Basis Document. *Tech. Rep.* July. Sandia National Laboratory, San Francisco, SAND2001-2100.

CHAPTER
FOUR

Validation of the thermal models with experimental data

Contents

Scientific Contributions

- M.R. Rodríguez-Sánchez, A. Sánchez-González, D. Santana. Revised receiver efficiency of molten-salt power towers. Submitted for publication to Renewable & sustainable energy reviews.

4.1 Abstract

The demonstration power plant Solar Two was the pioneer design of a molten−salt power tower in the report "Final Test and Evaluation Results from the Solar Two Project" (Pacheco, 2002) the efficiencies of the three main subsystems: heliostats, receiver and power block were measured or estimated. The efficiency of the plant and the power block could be obtained with confidence. Whereas, the efficiencies of the heliostat field and the receiver could only be estimated because the solar flux reflected by the heliostats and intercepted by the receiver cannot be measured. The receiver efficiency was estimated using

the Power−On Method. The authors themselves highlight that this method contain an important assumption: the temperature distribution on the receiver surface is independent of the incident power level. This assumption is equivalent to have a Biot number much smaller than one. For Solar Two reported data the Biot number is of order unity, and then the external tube temperature depends of the receiver load; being the thermal losses linearly with the incident solar flux rather than constant. Besides, our results show that receiver efficiency is around 76% for full load and 69% for half load instead of 87% and 80% reported assuming external tube temperature independent of the incident power.

4.2 Introduction

The increasing problem of CO_2 emissions has strengthened interest in renewable energy source. Solar Power Tower (SPT) is known as an important candidate for becoming in a major clean technology for commercial electricity power generation in the medium-term.

A STP is formed by three main subsystems: heliostat field, receiver and power block. The industry and laboratory research efforts are now focusing on optimizing the efficiency of the SPT. The power block is usually a traditional Rankine cycle, widely studied. Then, the global plant and the power block efficiency could be obtained with confidence because it is possible to reliably measure the input and the output data of the plant: Direct Normal Insolation (DNI), heliostats area, salt flow rate, salt temperature, and gross−electrical output.

However, the solar flux reflected by the heliostats and intercepted by the receiver cannot be measured, and then the efficiencies of the heliostat field and the receiver could only be estimated. In a SPT the receiver plays the important role of intercepting the reflected solar radiation from the heliostat field and transferring it to the heat transfer fluid. The main challenge associated with this process is the high temperature gradient at the receiver surface and transient thermal processes that may lead to local hot spots, and consequently, degradation or failure of the receiver (Winter *et al.*, 1991). Therefore, the receiver temperature distribution must be carefully controlled. The temperature distribution at the receiver surface depends on the heat flux distribution, which is closely connected with the heliostat field and the aiming strategy (Salomé & Thiery, 2013).

The heliostat field layout is another key in a SPT due to its high capital investment cost (approximately 45% of the plant−total cost (Collado, 2008)). Then, the proper estimation of the heliostat field is an economical target. Several models predict the solar flux distribution on the receiver and the optical efficiency of the heliostat field. Walzel *et al.* (1977) proposed a sixth order Hermite polynomial to obtain the flux map at the receiver. This model was first implemented in the RCELL code (Lipps & Vant-Hull, 1978), then in the DELSOL (Kistler, 1986), and most recently in the SAM software (Golden, 2015). Another approximate function, based on a single circular Gaussian distribution, is used by HFLCAL code (Schwarzbözl & Schmitz, 2009). Collado & Turégano (1986) obtained an analytical expression based on the error function, which is implemented in the UNIZAR model.

In addition, numerous authors based their studies in the thermal characterization of the molten salt receivers. Jianfeng *et al.* (2010) implemented a theoretical model that investigated the heat transfer performance of external receivers under unilateral concentrated solar radiation, obtaining receiver performances between $87 - 92\%$. Singer *et al.* (2010) made a similar study assuming no circumferential variations at the tube wall temperature, and their receiver thermal efficiency was comprised between $85 - 87\%$. Moreover, Lata *et al.* (2008) made a sensitivity analysis of a receiver panel based on the design of the Solar Tres receiver using the SENREC code; obtaining receiver efficiencies of $77 - 87\%$. However, since the amount of experimental data and studies concerning central receivers in the literature is reduced, the validation of these models is quite difficult.

Radosevich (1988) reported the experimental test results of the demonstration power plant Solar One, a direct steam-generation plant. He estimated the receiver efficiency as the unknown in a global energy balance. Where, the efficiencies of the global power plant and the power block were calculated, and the efficiency of the heliostat field was simulated by means of MIRVAL code. The receiver thermal efficiencies obtained were comprises between $70 - 76\%$. In addition, Baker (1990) stablished that *"the thermal losses in the Solar One receiver fit linearly with the incident power"*. Pacheco (2002) studied the demonstration power plant Solar Two, which was the pioneer design of a molten-salt power tower. He implemented a Power−On Method (POM) to calculate the receiver thermal efficiency. In the full knowledge that it is not entirely correct, they assumed that *"under steady-state conditions with constant inlet and outlet salt temperatures and wind velocity, the temperature distributions on the*

receiver surface and thorough the receiver are independent of the incident power level. Therefore, the thermal losses are also independent of the incident power". As a function of the solar irradiation and the wind speed, they obtained receiver performances of $80 - 87\%$.

The main goal of this work is to determine the receiver thermal efficiency using the data of the Solar Two Project, estimating the ratio between the thermal losses for half and full power. The POM is a good first approximation to calculate the receiver efficiency. However, it does not consider the tube wall temperature variations with the incident solar-flux distribution, and then assumes that the Biot number is lower than one. We show that in the Solar Two receiver the Biot number is of order unity, and then the estimated thermal efficiencies of the receiver are lower than those predicted by Pacheco (2002). These results permit a more accurate design and a revision of the objectives to improve SPT performance.

4.3 Solar Two: experimental procedure

Experimental data of SPT are scarce in the literature. For SPT working with molten salt only Pacheco (2002) have published experimental data. Since the incident power could not be measured directly on the receiver surface (Pacheco *et al.*, 1995), they designed a series of experiments carried out in the Solar Two power plant in order to calculate the efficiency of the receiver.

The experimental procedure divided the heliostat field into two groups with an equal number of heliostats symmetrically dispersed around the receiver. In this way, the power on the receiver could be halved regardless of the field cleanliness, mirror corrosion, and heliostat availability.

During 9 clear-sunny days four different tests were performed symmetrically about solar noon between 11:00 a.m. and 1:00 p.m. solar time. In the different periods of time, all the heliostats of the field (full power: cases A and C) or one half of the heliostats, scattered around the receiver (half power: cases B and D), were under operation, see Table 4.1 and Figure 4.2 for further information.

In order to keep constant the outlet temperature of the salt, the mass flow rate at the receiver was adjusted for each period of time. Then, because of symmetry the average incident power during period A is twice the average incident power during period D. Likewise, for periods C and B.

After defining the experimental procedure, the averaged data collected by Pacheco (2002) were: the heliostat availability, the mass flow rate at the re-

Table 4.1: Sequence of heliostat tracking the receiver (Pacheco, 2002).

Period	Solar Time	Heliostat Group(s)	Incident Power (Available)
A	11:00 a.m. to 11:30 a.m.	1 and 2	100%
B	11:30 a.m. to 12:00 p.m.	1	50%
C	12:00 p.m. to 12:30 p.m.	1 and 2	100%
D	12:30 p.m. to 13:00 p.m.	2	50%

ceiver, the inlet and outlet temperature of the salt, the DNI, and the wind direction and speed, see Table 4.2.

4.4 Power-On Method Analysis

The receiver efficiency is defined as the ratio of the average power absorbed by the working fluid to the average power incident on the receiver, and it is evaluated under steady-state-conditions.

$$\eta = \frac{\overline{P}_{abs}}{\overline{P}_{inc}} \tag{4.1}$$

From a heat balance on the receiver during steady-state conditions, the power incident on the receiver equals the sum of power reflected by the receiver, the power absorbed by the salt, and the receiver thermal losses (radiation, convection, and conduction), see Equation 4.2. The absorbed power is obtained using the inlet and outlet temperatures of the salt and the mass flow rate measured in the receiver.

$$\overline{P}_{inc} = \rho\overline{P}_{inc} + \overline{P}_{abs} + \overline{L}_{th} \tag{4.2}$$

Following the Power-On Method (POM) (Pacheco, 2002), the efficiency was obtained by eliminating the incident power from the heat balance equation and by calculating the thermal losses from known measurements. In addition, to solve the problem they made the following assumption in the full knowledge that it can be taken only as a first approximation: *"Under steady-state conditions with constant inlet and outlet salt temperatures and wind velocities, the temperature distributions on the receiver surface and throughout the receiver are*

Table 4.2: Summary of key measurements during receiver efficiency tests (Pacheco, 2002).

Test Date	**29/09/97**	**30/09/97**	**01/10/97**	**05/03/99**	**12/03/99**	**17/03/99**	**22/03/99**	**23/03/99**	**24/03/99**
Heliostats Tracking Receiver									
A	1767	1764	1804	1668	1685	1681	1699	1626	1725
B	883	883	897	831	853	836	847	809	858
C	1767	1758	1798	1664	1684	1676	1692	1625	1720
D	884	876	898	833	830	840	847	805	848
Average Mass Flow ($\dot{m}$) [kg/s]									
A	80	90	90	81	67	78	69	61	70
B	39	43	44	36	32	37	32	28	33
C	85	91	91	80	73	80	70	65	73
D	39	43	42	38	33	36	32	30	32
Average Inlet Temperature [°C]									
	295	301	305	308	303	302	301	302	299
Average Outlet Temperature [°C]									
	551	550	550	564	563	564	563	561	564
Average Ambient Temperature [°C]									
	32	33	33	16	14	18	18	16	17
Average Direct Normal Insolation [W/m^2]									
	913	975	942	989	898	960	871	874	894
Average Wind Speed [m/s]									
	0.6	1	0.6	3	1.8	1.4	0.9	7.9	1.3
Average Wind Direction (Clocklkwise from North)									
	131	241	210	270	223	241	165	263	241

independent of incident power level ($T_{we,A} = T_{we,D}$). Therefore, the thermal losses are also independent of the incident power ($L_{th,A} = L_{th,D}$)".

However, this assumption is contrary to the results obtained in a previous work (Rodríguez-Sánchez & Santana, 2014), in which a simplified thermal model to calculate the receiver efficiency was developed. Rodríguez-Sánchez & Santana (2014) found that the tube wall temperature depends on the incident power and its distribution. It can be seen applying an energy analysis on the

receiver. The heat flux absorbed by the molten salt at the receiver tubes can be expressed by Equation 4.3. Where, the heat power absorbed by the salt, the convective coefficient, the external tube wall temperature, and the mass flow rate depend on the incident power level; while the bulk temperature of the salt, the conductivity of the tube material, and the tube diameters are independent of that power.

$$P_{abs} = \left(\frac{d_o}{d_i h} + \frac{d_o ln\left(d_o/d_i\right)}{2k} \right)^{-1} \pi d_o L \left(T_{we} - T_{salt}\right) = \dot{m} Cp \Delta T_{salt} \quad (4.3)$$

Gnielinski (2013) revised the heat transfer correlation for turbulent flow in tubes finding that the convective coefficient grows as the Reynolds number raised to the power between 0.75 and 0.87. For simplicity, it has been assumed that the convective coefficient is proportional to the Reynolds number, and then to the salt velocity ($h \ \alpha \ Re \ \alpha \ v$). Equation 4.4 results from Equation 4.3, where the Biot number is defined as the ratio between conduction and convection resistances, $Bi = h d_i ln(d_o/d_i)/2k$.

$$P_{abs} = \pi L d_i h \left(1 + Bi\right)^{-1} \left(T_{we} - T_{salt}\right) = \dot{m} Cp \Delta T_{salt} \quad (4.4)$$

Equation 4.5 is obtained dividing a percentage of the full absorbed power (P'_{abs}) by the full absorbed power. Where it has been assumed that the convective coefficient and the mas flow rate vary proportionally to the salt velocity, and then $h\dot{m}'/h\dot{m} \simeq 1$.

$$\frac{1 + Bi'}{1 + Bi} = \frac{\left(T'_{we} - T_{salt}\right)}{\left(T_{we} - T_{salt}\right)} \quad (4.5)$$

It can be noticed that the only condition to match the tube wall temperature for a full power or any lower power is that the Biot number tends to zero. That means that the resistance by conduction must be negligible with respect to the resistance by convection. To fulfil that condition it is necessary that at least one of the following assumptions be achieved:

- Extremely high conductivity of the tube material. Nevertheless, the Solar Two tubes are 316 stainless steel, whose conductivity coefficient is $k = 20$ W/m°C.
- Slim tubes (1.2 mm for Solar Two), however thickness reduction is limited because it is detrimental for the mechanical behaviour of the tubes, generating a reduction of the receiver operational life.

- Small tube diameter (21 mm for Solar Two), but it increases the pressure drop and the consumption of the feed pumps (Rodríguez-Sánchez & Santana, 2014). In addition, a reduction of the tube diameter produces an increment of the salt velocity and of the convective coefficient, being contrary to the Biot number decrement.

- High circumferential diffusion in the tube surface, but in a previous work (Rodríguez-Sánchez & Santana, 2014) it has been demonstrated that the circumferential diffusion is negligible respect to the radial one.

For the Solar Two reported data the tube wall conduction and the internal convection resistances are of the same order. Therefore, the Bi number must be taken into account to calculate the receiver thermal efficiencies and the tube wall temperature, which would be higher for full power than for half power. Figure 4.1 represents the Biot number as a function of the absorbed power for September 29^{th} 1997 reported by Pacheco (2002). It can be seen that in this kind of problems the Biot number is not constant, it increases with the absorbed power in a nonlinear way, neither negligible, for an absorbed power of 100% de Biot number is 2.8.

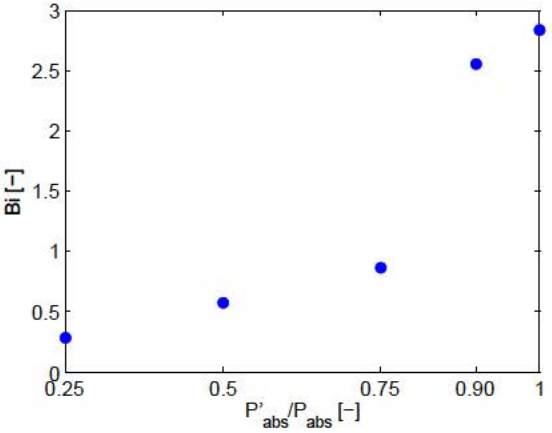

Figure 4.1: Variation of the Biot number as a function of the absorbed power.

Once it has been proved the necessity of considering the Biot number in this problem, a modification in the Power-On Method has been introduced, in order to take into account the heat losses variations with the incident power. The differences between the thermal losses for full and half power have been included

as $L_{th,D} = yL_{th,A}$. Then, under this assumption, the equations used by POM to obtain the thermal losses and the receiver efficiency are the following ones:

$$\begin{cases} P_{inc,A} = 2P_{inc,D} \\ P_{inc_C} = 2P_{inc,B} \end{cases} \tag{4.6}$$

$$\begin{cases} P_{abs,A} + L_{th,A} = 2P_{abs,D} + 2L_{th,A} \\ P_{abs,C} + L_{th,C} = 2P_{abs,B} + 2L_{th,C} \end{cases} \tag{4.7}$$

$$L_{th,A} = L_{th,C} = \frac{(P_{abs,A} + P_{abs,C} - 2P_{abs,B} - 2P_{abs,D})}{4y - 2} \tag{4.8}$$

$$L_{th,D} = L_{th,B} = yL_{th,A} = yL_{th,C} \tag{4.9}$$

$$\eta = \frac{P_{abs}}{P_{inc}} = \frac{\alpha}{1 + \frac{L_{th}}{P_abs}} \tag{4.10}$$

Pacheco (2002) assumed that the thermal losses are constant with the incident power level, $y = 1$. It has been demonstrated that this value must be lower than the unit; however it cannot be estimated using only the measured data from Solar Two and the Power-On Method. Then, a more detailed thermal model has been used to calculate the thermal losses.

4.4.1 Simplified thermal model

A simplified model of the central receivers has been yet presented by Rodríguez-Sánchez & Santana (2014). That model has been modified in order to adapt it as much as possible to the Solar Two operational and geometrical characteristics. In addition, it has been combined with the heliostat model developed by Sánchez-González & Santana (2015) that allows to calculate the solar flux distribution on the receiver.

The Solar Two collector field consists of 1818 heliostats (mirror area: 39.13 m^2) of the former Solar One plant and 108 new heliostats (95 m^2) added to the south side. Each heliostat coordinate has been gathered from Pacheco (2002). Besides the heliostat field layout, other optical parameters have been

taken from the same reference, e.g.: reflectivity, cleanliness, tracking error or heliostat availability.

Heliostats were aimed at different positions along the vertical of the receiver surface. Every 10 minutes, each heliostat aiming was commanded by the Static Aim Processing System (SAPS), which ensures a rather uniform flux distribution in the central region of the receiver. In the absence of specific aim-point information, a previously reported multi-aiming strategy (Sánchez-González & Santana, 2015) has been applied in the computational model. An aiming factor equal to 1.5 has been assigned in order to reduce spillage losses and distribute homogeneously the solar flux.

For each selected day and instant of time in the middle of each period (Table 4.2), the flux density distribution on the receiver has been computed using the optical model (Sánchez-González & Santana, 2015). The optical efficiency at Solar Two heliostat field is represented in Figure 4.2 for each period during experiments of September 29^{th}, 1997. In addition, for these experiments the measured field efficiency, ignoring heliostats reflectivity and cleanliness, was between 66% and 62%, in agreement with our model outputs (62.6 - 61.7%). On the basis of the optical model, flux maps for each test period are generated, providing the necessary input for the proposed receiver thermal model (Rodríguez-Sánchez & Santana, 2014).

Regarding the external receiver the main design parameters can be seen in Table 4.3. Although the operation mode of Solar Two have been widely described in Pacheco (2002), there are some unknown parameters that have to be assumed in the thermal model. To estimate the mass flow rate in the receiver, it has been imposed that the salt temperature at the outlet of the receiver for each period is that reported by Pacheco (2002). By means of a valve the mass flow rate in each flow path is fitting, to fulfil the outlet temperature of the salt. Besides, the mass flow by all the tubes of a panel is assumed to be the same.

The mass flow rate predicted by the authors is slightly lower than that measured in the tests ($\sim$10kg/s), it could be associated to a difference in the solar flux distribution on the receiver. Besides, it is necessary to take into account that: the reported experimental results corresponds to averaged data over half an hour (i.e. non-instantaneous), the internal Nusselt correlation adopted in the simulations is subject to an error, conditions of cleanliness and constant absorptivity has been assumed, the aiming point strategy for the heliostat at Solar Two is not fully described, the process of heat exchange in the head of the panels has been neglected in the thermal model, and then fully developed

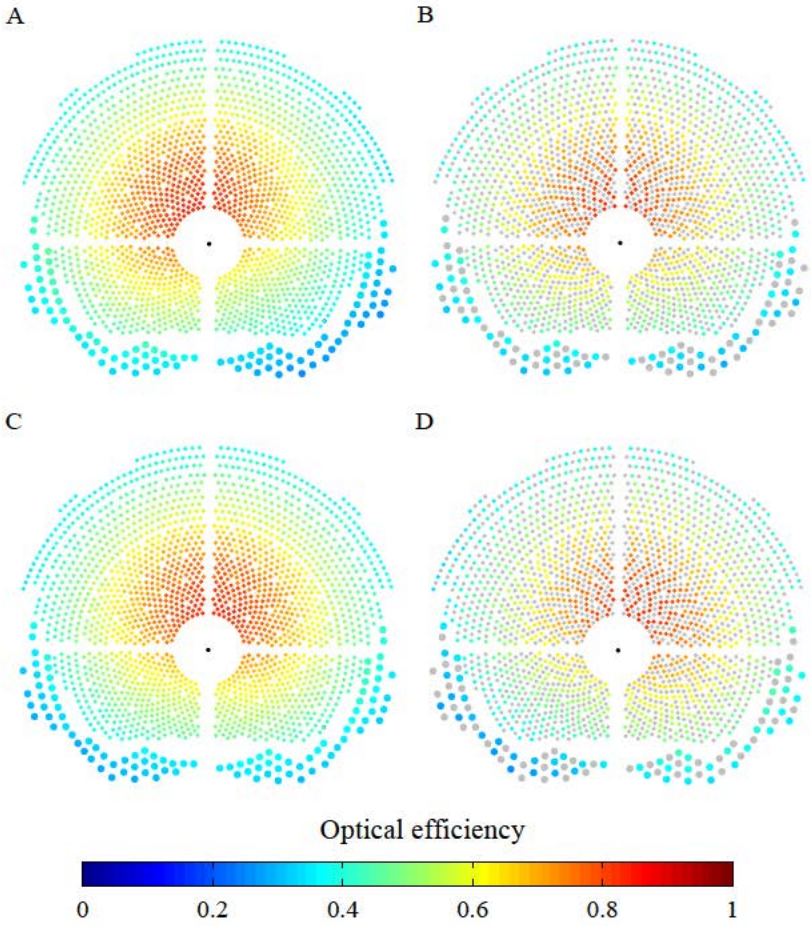

Figure 4.2: Simulated optical efficiency of the heliostats at Solar Two field during the four cases of September 29^{th}, 1997.

flow has been assumed in the whole receiver, etc.

According to this model the thermal losses for half power are around 64% of the thermal losses for full power, $y = 0.642$.

Table 4.3: Main design parameters of the Solar Two heliostat field and solar receiver.

Number of heliostat	1960
Heat Transfer Fluid	Molten Salt
Tube material	316H Stainless Steel
Receiver Diameter/ Lenght	5.1/ 6.2 m
Inlet/ Outlet temperature	290/ 565 °C
Number of flow circuits	2
Number of panels	24
Number of tubes per panel	32
Tube diameter/ thickness	21 / 1.2 mm
Absorptivity	0.95 (Black Pyromark)

4.5 Results

In this section the thermal losses and the thermal efficiency of the receiver for full and half power have been shown. They have been obtained by the Power-On Method using $y = 1$ (assumed by Pacheco (2002)) and $y = 0.642$ (estimated using Rodríguez-Sánchez & Santana (2014) and Sánchez-González & Santana (2015)).

In addition, the distribution of the tube wall temperature have been calculated and compared for both assumptions. In contrast to $y = 1$, for $y = 0.642$ differences can be seen in the tube wall temperature distribution caused by the variation of the incident power in the receiver. It produces different thermal losses for full and half power.

Figure 4.3 shows the thermal losses and the receiver thermal efficiency obtained by the POM with $y = 1$, assuming that the thermal losses are equal for full and half power. In addition, it can be seen the results obtained for the POM and $y = 0.642$. In this way, the thermal losses are dependent of the incident power and in both cases are higher than the thermal losses predicted with $y = 1$. It is due to the elevated wall temperature in the front part of the tubes (see Figure 4.4). Since the thermal losses are higher, the receiver efficiencies are lower than those expected by $y = 1$, approximately 11% lower. In addition, the averaged values for all the test days of each experiment are shown.

The estimated $y = 0.642$ generates different heat losses for full and half power. And as it was expected the heat losses for full power are higher than for half power (see Figure 4.3(a)). In addition, the heat losses obtained with this y are for both cases higher that the predicted by the assumption of $y = 1$.

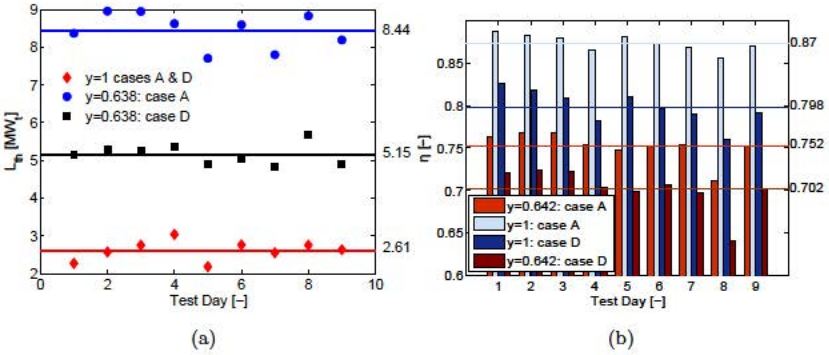

Figure 4.3: a)Thermal losses and b) Receiver efficiency comparison for case A and D using $y = 1$ and $y = 0.642$.

The average difference in the thermal losses between both y values is 5.8 MW for full field, and 2.54 MW for half field.

Considering that the receiver temperature distribution is dependent on the incident power ($y = 0.642$) the thermal efficiency decreases in average 11% respect to the $y = 1$ (see Figure 4.3(b)). The maximum efficiency difference is 14.53% for full field and 12.1% for half field, both occurs the 23^{th} of March, a day with high wind speed, low DNI and low mass flow rate in the receiver.

Taking into account the whole plant, the global efficiency must be 15% (Pacheco, 2002). For $y = 0.642$ multiplying the three efficiencies: power block (34% calculated in Pacheco (2002)), heliostat field (53%) and receiver (76%) the expected global efficiency has been obtained. However, for $y = 1$ the global efficiency is slightly higher, attributed to a mistake in the heliostat field model (Pacheco, 2002).

Figure 4.4 represents the temperature distribution in every panel of the receiver according to the thermal model ($y = 0.642$) for September 29^{th} 1997. It can be seen how the surface temperature distribution varies with the incident power. Figure 4.4(a) corresponds to full power distribution (case A), circumferential variations of the tube wall temperature can be observed. The maximum tube wall temperature reaches 595.53 °C in the external part of the tubes sited on the west/east side of the receiver. Figure 4.4(b) depicts the tube wall temperature distribution of the receiver working at half power (case D), its maximum value is 567.7 °C, and it is found in the same location than for case A.

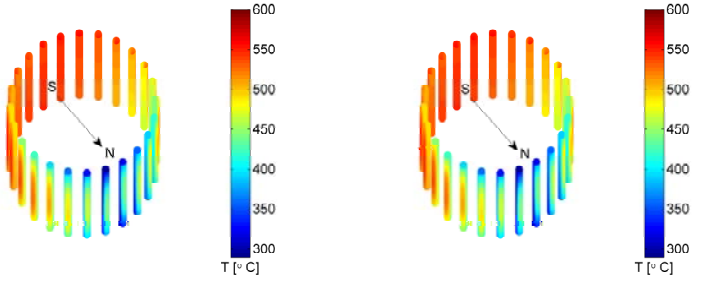

(a) (b)

Figure 4.4: Tube wall temperature distribution using $y = 0.642$ for September 29^{th} 1997. (a) Case A. (b) Case D.

Figure 4.5 shows the temperature distribution of the receiver tubes as the result of applying the hypothesis of $y = 1$, (Pacheco, 2002). The first problem found was that it is impossible to fix the three dependent variables: incident power, mass flow rate and outlet salt temperature. Then, it was decided to keep constant the absorbed power varying the incident one. The day shown is September 29^{th} 1997 and case A, although according to Pacheco (2002) the case is indifferent because all them have the same temperature distribution. As has been previously shown the tube wall temperature does not vary circumferentially. In this case the maximum tube wall temperature is 566 °C and it is located in the southern tubes. It means that modifying the y value the tube wall temperatures differ in 30 °C. It has strong influence in the heat losses, mainly in the radiative heat losses.

It is not the same the average temperature at the fourth potency than the individual temperature at the fourth potency averaged ($\overline{T^4} > \overline{T}^4$). Then, the effective temperature of radiation calculated with $y = 0.642$ for full and half power of September 29^{th} 1997 is 793.5 °C and 771.6 °C, respectively. While for $y = 1$ the value of this temperature is 632.2 °C, calculated by Equation 4.4 and full power. The difference in the effective temperature of radiation affect to the thermal losses and then to the thermal efficiency, as can be seen in Figure 4.3.

4.5.1 Variation of the incident thermal power

In this subsection we have extended the Solar Two results for half and full power reported by Pacheco (2002) to different incident power of the receiver by means

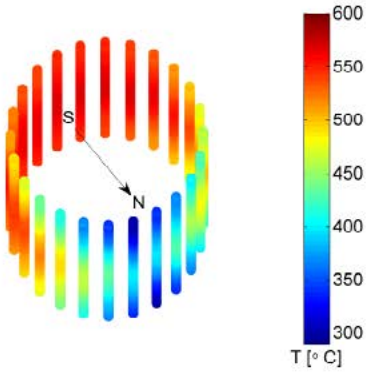

Figure 4.5: Tube wall temperature distribution using $y = 1$ for September 29^{th} 1997.

of the thermal model developed by the authors.

Figure 4.6 shows the tube wall temperature distribution along the receiver and how it varies as a function of the incident power (25%, 50%, 75% and 100%) from the day September 30^{th} 1997. In addition, it can be seen the average salt temperature evolution, that is practically constant for the fourth incident power analysed.

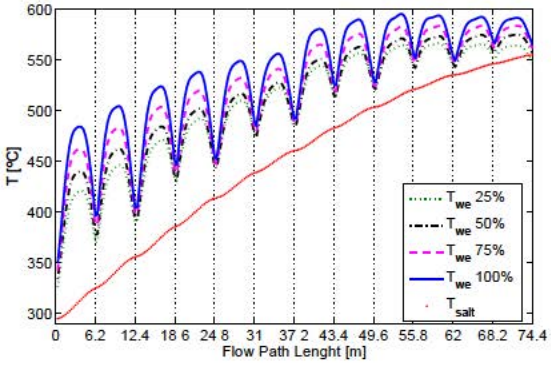

Figure 4.6: Tube wall temperature distribution along the receiver as a function of the incident power.

In Figure 4.6 it is shown that the tube wall temperature is strongly affected by the incident power, moreover in the centre of the tubes. The maximum

tube wall temperature is 596 °C for the maximum incident power, for a 75% of this power the maximum wall temperature decreases to 584 °C, while for a 25% decreases to 567 °C. These 30 °C of difference respect to the total incident power could have a fatal influence in the mechanical behaviour of the tubes and in their life time operation.

Figure 4.7(a) presents the relative heat losses as a function of the incident power. It can be noticed that the thermal losses ratio is lineal with respect the incident power, in this way it can be said that for the Solar Two the thermal losses ratio, y, can be expressed as a lineal function of the incident power, see Equation 4.11. In addition, it is observed that for an incident power of 25% the thermal losses are reduced 56% respect to the full load case.

$$\frac{L'_{th}}{L_{th}} = y = 0.74\frac{P'_{inc}}{P_{inc}} + 0.25 \tag{4.11}$$

Figure ?? shows the receiver thermal efficiency relation as a function of the incident power. It can be seen that the efficiency increases with the incident power even though the thermal losses increases too. The receiver efficiency varies smoother than the thermal losses, less than 20% when the incident power is a quarter of the total one; and this variation is not linear. Although the receiver efficiency increases with the incident power, and then with the thermal losses, it is always lower than the estimated by the Power-On Method for $y = 1$.

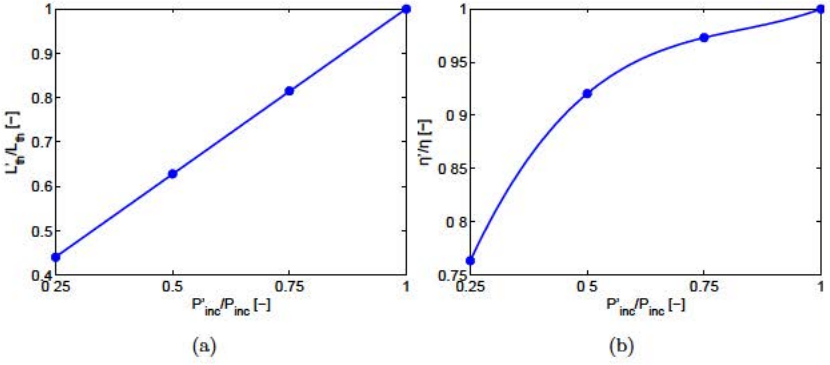

(a) (b)

Figure 4.7: a) Thermal losses ratio and b) receiver thermal efficiency ratio as a function of the incident power for Solar Two project.

Then, given the expression, and measuring the absorbed power for any ratio of incident power it is possible to calculate, by means of the Power-On Method,

any thermal behaviour of the receiver using the following equations. However, when y is missing another model more detailed it is necessary to calculate these values, due to the thermal losses varies with the incident power.

$$L_{th} = \frac{P'_{abs} - P_{abs}\frac{P'_{inc}}{P_{inc}}}{0.26\frac{P'_{inc}}{P_{inc}} - 0.25} \tag{4.12}$$

$$\eta = \frac{P_{abs}}{P_{inc}} = \frac{P_{inc} - L_{th}}{P_{inc}} \tag{4.13}$$

Figure 4.8 is the result of applied the Equations 4.12 and 4.13 for Solar Two receiver. As it was said before, it has been obtained that for full power the heat losses are 8.5 MW and the receiver efficiency of 0.76 for full power. Moreover, the values of these variables for 25% and 75% of power can be obtained without the necessity of experimental measures.

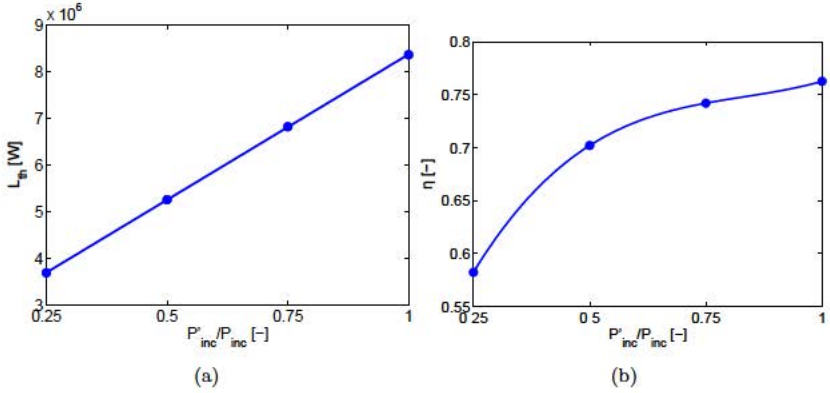

Figure 4.8: a) Thermal losses and b) receiver thermal efficiency as a function of the incident power for Solar Two project.

4.6 Conclusions

The precise estimation of the thermal behaviour of the central receiver of a SPT is necessary to avoid damages in this system. Furthermore, it is important for the design of the heliostat field, the most expensive part of a SPT. An oversized heliostat field means an unnecessary investment cost, while and undersized heliostat field reduces the electrical energy production of the SPT.

To calculate the receiver efficiency Pacheco (2002) developed the Power-On Method on the basis of the experimental test results of the pilot plant Solar Two. In that model the following assumption, in the full knowledge that it is not entirely correct was made: *"Under steady-state conditions with constant inlet and outlet salt temperatures and wind velocities, the temperature distributions on the receiver surface and throughout the receiver are independent of incident power level ($T = T_{1/2}$). Therefore, the thermal losses are also independent of the incident power ($L_{th} = L_{th,1/2}$)"*. It is the same that neglect the conductivity of the receiver tubes and considers the Bi number much lower than one. However, from Solar Two reported data it can be calculated that the tube wall conduction and the internal convection resistances are of the same order ($Bi = 2.8$), and then the Bi number must be taken into account to obtain the receiver thermal efficiencies, and the tube wall temperature.

Therefore, the Power-On Method cannot be employed while the thermal losses ratio or at least the thermal losses for full power are not measured. In the absence of more detailed experimental data the authors have used a previous developed thermal model for central receivers (Rodríguez-Sánchez & Santana, 2014; Sánchez-González & Santana, 2015). In this way, a lineal relation between the thermal losses and the incident power has been found $L'_{th}/L_{th} = y = 0.74P'_{inc}/P_{inc}+0.25$. The thermal losses for half power are 64.2% of the thermal losses for full power. This thermal losses relation allows to extend the model for any ratio of incident power, even in absence of experimental data of a particular incident power.

In addition, the thermal model allows to calculate the tube wall temperature distribution as a function of the incident power. In a receiver tube there are circumferential variations of the surface temperature that modify the effective temperature of radiation from 640 °C for $y = 1$ to 790 °C for $y = 0.642$. According to POM with $y = 1$, in which there are not circumferential variations, the thermal losses of the receiver were 2.61 MW. However, for $y = 0.642$, in which these variations are taken into account, the thermal losses increase up to 8.5MW for the full field. As a consequence, the thermal efficiency of the receiver decreases 11%, from 87% to 76%; it is agreement to the global plant efficiency. These results would permit a more accurate design and a revision of the objectives to improve SPT performance.

Nomenclature

Bi	Biot number [-]
C_p	Specific heat [J/kg° C]
DNI	Direct normal irradiance [W/m^2]
H/L	Receiver/ Tube length [m]
d	Tube diameter [m]
h	Convective coefficient [W/m^{2}K]
k	Conductive coefficient [W/mK]
L_{th}	Thermal losses [W]
$\dot{m}$	Mass flow rate [kg/s]
P	Power [W]
q''	Heat flux [W/m^2]
Re	Reynolds number [-]
T	Temperature [° C]
v	Molten salt velocity [m/s]
y	Thermal losses ratio [-]
z	Axial coordinate [m]

Greek letters

α	Absorptivity [-]
ϵ	Emissivity [-]
η	Thermal efficiency [%]
ρ	Reflectivity [-]
σ	Stefan-Boltzmann constant [W/m^{2}K^4]

Subscripts

abs	Absorbed
conv	Convection
i	Internal
inc	Incident
o	External
rad	Radiation
we	External wall

Abbreviattions

POM	Power-on method
SAPS	Static aim processing system
SPT	Solar power tower

References

Baker, Aivin F 1990 Techniques for Processing Experimental Data From a Solar Central Receiver to Evaluate the receiver steady-state efficiency. *Journal of Solar Energy Engineering* 112 (February), 6–11.

Collado, F.J.; Gómez, A. & Turégano, J.A. 1986 An analytic function for the flux density due to sunlight reflected from a heliostat. *Solar Energy* 37, 215–34.

Collado, F.J. 2008 Quick evaluation of the annual heliostat field efficiency. *Solar Energy* 82 (4), 379–384.

Gnielinski, V. 2013 On heat transfer in tubes. *International Journal of Heat and Mass Transfer* 63, 134–140.

Golden, C. 2015 System advisor model (sam). sam.nrel.gov/content/downloads.

Jianfeng, Lu, Jing, Ding & Jianping, Yang 2010 Heat transfer performance of an external receiver pipe under unilateral concentrated solar radiation. *Solar Energy* 84 (11), 1879–1887.

Kistler, B.L. 1986 A User's Manual for DELSOL3: A Computer Code for Calculating the Optical Performance and Optimal System Design for Solar Thermal Central Receiver Plants. *Tech. Rep.*. Sandia National Laboratories, Albuquerque.

Lata, Jesús M., Rodríguez, Manuel & Álvarez de Lara, Mónica 2008 High Flux Central Receivers of Molten Salts for the New Generation of Commercial Stand-Alone Solar Power Plants. *Journal of Solar Energy Engineering* 130 (2), 1–5.

Lipps, F.W. & Vant-Hull, L.L. 1978 A cellwise method for the optimization of large central receiver systems. *Solar Energy* 20 (6), 505–516.

Pacheco, J.E. 2002 Final Test and Evaluation Results from the Solar Two Project. *Tech. Rep.* January. Sandia National Laboratories, Albuquerque, SAND2002-0120.

Pacheco, J.E., Ralph, M.E. & Chavez, J.M. 1995 Investigation of Cold Filling Receiver Panels and Piping in Molten-Nitrate-Salt Central-Receiver Solar Power Plants. *Journal of Solar Energy Engineering* 117 (NOVEMBER), 282.

Radosevich, L.G. 1988 Final Report on the Power Production Phase of the 10MWe Solar Thermal Central Receiver Pilot Plant. *Tech. Rep.*. Sandia National Laboratories. SAN087-8022, Livermore, California.

Rodríguez-Sánchez, M.R.; Soria-Verdugo, A.; Almendros-Ibáñez J.A; Acosta-Iborra A. & Santana, D. 2014 Thermal design guidelines of solar power towers. *Applied Thermal Engineering* 63 (1), 428–438.

Salomé, A.; Chhel, F.; Flamant G.; Ferrière-A. & Thiery, F. 2013 Control of the flux distribution on a solar tower receiver using an optimized aiming point strategy: Application to THEMIS solar tower. *Solar Energy* 94, 352–366.

Sánchez-González, A. & Santana, D. 2015 Solar flux distribution on central receivers: A projection method from analytic function. *Renewable Energy* 74, 576–587.

Schwarzbözl, P.; Pitz-Paal, R. & Schmitz, M. 2009 Visual HFLCAL - A Software Tool for Layout and Optimisation of Heliostat Fields. In *SolarPACES*. Berlin, Germany: SolarPACES.

Singer, C.; Buck, R.;, Pitz-Paal, R. & MuÌĹller-Steinhagen, H. 2010 Assessment of Solar Power Tower Driven Ultrasupercritical Steam Cycles Applying Tubular Central Receivers With Varied Heat Transfer Media. *Journal of Solar Energy Engineering* 132 (4), 041010: 1–12.

Walzel, M.D., Lipps, F.W. & Vant-Hull, L.L. 1977 A solar flux density calculation for a solar tower concentrator using a two-dimensional hermite function expansion. *Solar Energy* 19 (3), 239–253.

Winter, C J, Sizmann, R L & Vant-Hull, L L 1991 *Solar Power Plants*. Berlin, Heidelberg: Springer Berlin Heidelberg.

CHAPTER

FIVE

Design guidelines of solar external receivers under nominal conditions

Contents

Scientific Contributions

- M.R. Rodríguez-Sánchez, M. Venegas, C. Marugán-Cruz, D. Santana. Thermal, mechanical and hydrodynamic analysis to optimize the design of molten salt central receivers of solar tower power plants. Proceedings of International Conference on Renewable Energies and Power Quality (ICREPQ), (2013).

- M.R. Rodríguez-Sánchez, A. Soria-Verdugo, J.A. Almendros-IbáÃśez, A. Acosta-Iborra, D. Santana. Thermal design guidelines of solar power towers. Applied Thermal Engineering, 63 (2014) 428-438.

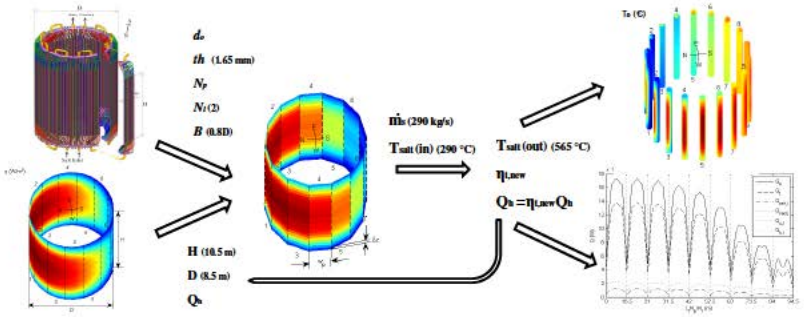

5.1 Abstract

One of the main problems of solar power tower plants with molten salt as heat transfer fluid is the reliability of central receivers. The receiver must withstand high working temperatures, molten salt corrosion and important solar flux transients that lead to thermal stresses and fatigue. Despite these difficulties, it is necessary an estimation of the receiver thermal efficiency in order to have an accurate estimation of the investment cost of the solar plant and to assure the lifetime estimation of the receiver.

A thermal, mechanical and hydrodynamic analysis of these receivers has been developing in this work, assuming constant heat flux in each axial discretized section of the tube wall but considering circumferential temperature variations in the perimeter of the tubes caused by the difference between the heat flux received by the front part of the tubes and by the rear part.

The thermal analysis shows that the radiation losses are higher than in literature, and consequently the thermal efficiency is lower too. This is due to the fact that the effective tube wall temperature for radiation is higher than the mean tube wall temperature, especially if the rear temperature of the tubes is considered. Besides, it has been found that the highest temperatures and thermal stresses are sited on the eastern and western panels of the receivers.

Film temperature is the most limiting parameter for the receiver design due to it is responsible for salt decomposition and tube corrosion. Therefore, once the tube material is chosen, the film temperature cannot exceed a critical value over which the corrosion ratio raises rapidly. Small tube diameters and low number of panels results in low film temperatures, although this kind of design increases the pressure drop. Therefore, a compromise between film temperature and pressure drop can lead to a receiver design that ensures its lifetime, and at

the same time, optimizes the investment and operational cost of the receiver.

5.2 Introduction

Environmental problems and limited fossil fuel resources require new sustainable electricity generation options. An important alternative for providing clean and renewable energy needed in the future is solar thermal power generation with optical concentration technologies. Solar power tower technology (SPT), using molten salt as a heat transfer fluid (HTF), is known as one of the most promising technologies for electricity generation. SPT has the advantages of high working temperatures, high efficiency, great power and a large thermal storage capability that lets cost advantages respect to dispatchability.

SPT consists of three main systems: heliostat field, solar collector and power-block island. Direct solar radiation is reflected and concentrated by a heliostat field (individual mirror assembly with solar tracking system) onto a receiver placed at the top of a tower. In this way, the direct solar radiation is concentrated in the effective area of the receiver reaching a high flux of radiation, which is converted into thermal energy in the working fluid. In SPT much attention has to be paid to the heliostat field because they are around 50% of the total capital investment cost (Kolb & Gary, 2011) and to the receiver that represent the 20% of the total capital investment cost (Gielen, 2012). This fact highlights the importance of a correct estimation of the receiver thermal efficiency, to avoid oversize the heliostat field and increase excessively the cost of SPT systems.

Nevertheless, receivers have the most uncertain lifetime because they are subjected to extreme working conditions; the outer surface of the tubes intercepts high solar flux radiation while the inner surface of the tubes is in contact to HTF. During operation of the receiver the main problems are tube corrosion caused by the high corrosive effect of the molten salt at high temperature; cracks in the welded zones and problems related to material resistance due to thermal stresses and fatigue; tube overheating; and salt freezing during unsteady states (passage of clouds).

In the last years, many efforts have been focused on the receiver design optimization in order to reduce heat losses and early failure of the tubes, as well as to increase the energy conversion efficiency of the receiver. Lata *et al.* (2008) focused their research on the optimization of the diameter and wall thickness of the receiver tubes. In addition, they analysed different tube materials as nickel

base alloys 625-LCF, 230, 617-LCF and the austenitic stainless steel 800H to establish which one could fulfil better the solar power plant requirements. On the contrary, other authors tried modifying the heat transfer fluid (HTF); Jianfeng *et al.* (2010) made a numerical analysis using HIATEC, they studied the heat absorption efficiency and heat transfer characteristics of an external receiver under unilateral concentrated solar radiation realizing how the efficiency increases with the incident energy flux and the flow velocity and obtaining values for absorption efficiency between 83 and 90%. Cui *et al.* (2006) even tested solid-liquid phase change materials with high melting point; they analysed numerically and experimentally the thermal performance of one isolated tube and developed a numerical model based on the enthalpy method. Liao *et al.* (2014) studied the maximum flux density allowable in solar receivers for different HTF and tube materials due to the thermal strains in the tubes; they assumed a non-uniform flux distribution on the outside tube surfaces, with cosine shape.

A further step was taken by other authors that presented novel designs for molten salt solar receivers. It is the case of Yang *et al.* (2010), who tested a solar receiver formed by spiral tubes, using HIATEC as heat transfer fluid in their experiments; Garbrecht *et al.* (2013), proposed an innovative design composed by many hexagonal pyramid shaped elements instead of tubes, obtaining thermal efficiencies of 91.2%; Boerema & Rosengarten (2013) calculated the flux distribution and the thermal efficiency of a receiver formed by panels of tubes multi-diameter. They assumed that the heat flux distributional along the tube perimeter is a cosine function in the front part of the tubes and null in the rear part, obtaining an efficiency of 92.6%; and Lim *et al.* (2014) proposed a tubular solar receiver with porous medium, they optimize the receiver design as a compromise between the maximum temperature of the porous medium and the maximum pressure drop.

Furthermore, the convection and radiation heat losses play an important role in the heat absorption processes of central receivers and these processes have been studied by numerous authors. Dehghan & Behnia (1996) investigated the heat efficiency of the receivers by considering natural convection, conduction and radiation heat transfer in a discretely heated open cavity. Jianfeng *et al.* (2010) analysed numerically the effects of radiation and convection heat losses on the energy absorbed by an isolated tube of an external receiver and Clausing (1981) analysed the convective losses from cavity central receivers. Pacheco (2002) reported the test results of the external molten salt receiver from Solar Two project, they obtained high values for the receiver efficiency (85- 89%).

It was calculated as a function of wind speed by the power-on method which assumes that thermal losses are independent of the incident radiation power.

In the present paper, a thermal study of central receivers for a solar power tower plant has been carried out. This is an external receiver that uses molten salt (60% wt $NaNO_3$ and 40% wt KNO_3) as heat transfer fluid. The main characteristics of this salt are low vapour pressure, neither inflammable nor explosive, properties desirable for thermal storage (Mar & Kramer, 1980). In contrast, it has a great corrosion potential that presents a challenge for the heat exchange in the receiver (Allen & Janz, 1980).

The thermal analysis takes into account circumferential and axial variations of the tube wall temperature. Tube temperature is not circumferentially homogeneous, as in the case of water tube boilers where the wall temperature is approximately the phase change temperature, being the non-uniform interception of solar radiation by the tubes the main cause of the temperature variations in the heat-transfer process.

In this way, the heat flux absorbed by the tubes and the evolution of wall, film and bulk temperatures along the receiver have been calculated. In addition, in order to optimize the design of the receivers and the heliostat field and assure the lifetime of SPT, the thermal stresses of the tubes, the total pressure drop and the thermal efficiency of the receiver, based on the wall temperature of each tube element (and not on the mean wall temperature) have been analysed.

5.3 Central solar receiver configuration: Design considerations

The molten salt central receiver analysed is configured as a 360 degrees cylindrical tubular receiver, formed by a variable number of vertical blocks of tubes, panels. Each panel include an inlet header, inlet nozzles, tubes, outlet nozzles and an outlet header (top-left of Figure 5.1). The tubes of each panel are individually supported at the top that permits unrestricted downward thermal expansion and it is guided periodically over its entire length by tube clips welded to each tube (Falcone, 1986). In order to reduce the heat losses in the back side of the tubes, there is a thermal insulation (mineral wool) jacketed by a high reflectivity material (Zavoico, 2001).

In the north hemisphere, the inlet flow at minimum temperature enters at the north side of the receiver, where the solar flux is maximum. Here the salt is divided in two parallel flows, to ensure symmetry. Both parallel flows exit

at the south side at maximum temperature. The HTF flows as a serpentine from one panel to the next, and one or more crossovers in the flow paths are provided to keep the energy capture of the two parallel flows in balance over the complete range of operating conditions. The same parameters or as similar as possible to those of Gemasolar SPT have been used in this study (Table 5.1), with the exception of the tube external diameter (d_o) and the number of panels (N_p) which are variable.

Table 5.1: Design parameters.

Parameters	**Values**
Receiver length, H	10.5 m
Receiver diameter, D	8.5 m
Thermal power	120 MW_{th}
Total mass flow, $\dot{m}_s$	290 kg/s
Number of flow paths, N_{fp}	2
Tube thickness, th	1.65 mm
Tube pitch, B	8% d_o
Ambient temperature, T_{amb}	30 °C
Ambient pressure, P_{amb}	1 bar
Relative humidity, ϕ	60%
Wind speed, v	0 m/s

To fulfil the power balance the salt goes into the receiver at a bulk temperature equal to $T_{salt}(in) = 290$ °C to avoid salt freezing and exits at $T_{salt}(end) = 565$ °C to prevent solar salt decomposition. Thermal decomposition of the solar salt begins about 580 °C (Nissen & Meeker, 1983). The salt bulk temperature must maintain below this limiting temperature to avoid nitrate thermal decomposition to high corrosive compounds as nitrites and peroxides (Burgaleta *et al.*, 2009).

In this study has been used Incoloy Alloy 800H, whose film temperature must reach less than 650 °C (Bradshaw & Goods, 2001). Miliozzi *et al.* (2001) found the limiting temperature for other materials as 316 stainless steel and Inconel 625-LCF, whose maximum film temperatures are 600 °C and 630 °C. As Incoloy has high solar reflectivity and low solar absorptivity, a coating as black Pyromark has to be used, it has a solar absorptivity of about 93% (Persky & Szczesniak, 2008) and a thermal emissivity around 85% (Kennedy, 2002).

A model for the radiation flux map has been used to carry out this analy-

sis. It is a two-dimensional normal distribution with average heat flux of 0.8 MW/m^2 and a maximum heat flux of 1.2 MW/m^2. The radiation flux of this model is similar to the obtained with a three aiming point strategy. The map is symmetric respect to the north-south axis, as shown at the bottom-left of Figure 5.1. Since the plant is located in the north hemisphere, the highest heat flux is received at the north face of the receiver and the lowest at the south side. In order to fulfil the inlet and outlet salt temperature, it could be necessary to reduce the initial heat flux on the receiver, in these cases the radiation map will be multiplied by a factor lower than unit (η_t).

5.4 Proposed modelling.

In this section a thermal model for the receiver is introduced. The model assumes that there are temperature variations in axial and circumferential directions. To solve this problem, the tube is discretized in sections (cells) where a uniform heat flux is considered to be absorbed. A two-dimensional discretization, in axial and circumferential direction, has been employed to define the cells. In order to simplify the simulation just one tube per panel has been simulated, although the influence of the adjacent tubes has been taken into account.

The problem has been solved by an iterative process, as Figure 5.1 shows. The geometry of the receiver is given by its vertical length and diameter (H, D), the outer diameter and the thickness of the tubes (d_o, th), the tube pitch (B), the number of panels (N_p), and the number of flow paths (N_{fp}). The heat flux reaches each section of tube (Q_j) can be estimated using these geometrical parameters and the radiation map model of the incident solar power on the receiver (Q_h); the heat flux that arrives for each section of tube can be estimated. In addition, imposing the total mass flow in the receiver ($\dot{m}_s$) and the inlet salt temperature ($T_{salt}(in)$), the outlet salt temperature ($T_{salt}(end)$) can be calculated. If is different to 565 °C, the radiation map values (Q_h) are multiplied by the factor η_t to obtain a new value ($Q_{h,new}$) and the calculation process is repeated. When the simulation converges ($T_{salt}(end) = 565$ °C), the heat losses, salt and wall temperatures, and thermal efficiency of the receiver (ϵ_{th}) are calculated. Once the thermal analysis is completed, the mechanical and hydrodynamic behaviours are studied in order to optimize the receiver design.

Convective losses ($Q_{c,l}$ or $q_{c,l}$) are caused by natural and forced convection. The convective heat transfer coefficient was calculated using Equation

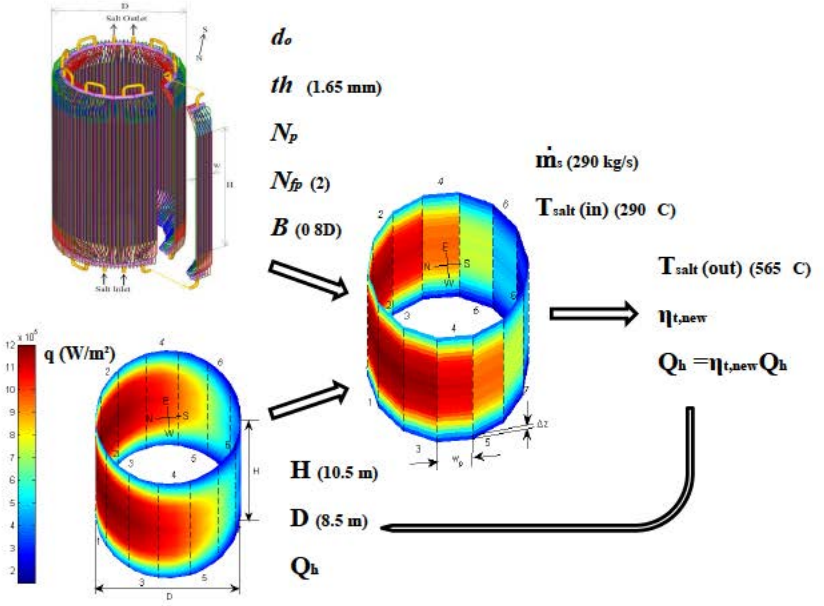

Figure 5.1: Calculation scheme for the thermal analysis of an external receiver.

5.1, according to Siebers & Kraabel (1984), where $\overline{h}_{fc}$ is the forced convection coefficient, which is obtained from the Nusselt number based on the receiver diameter (Nu_D), and $\overline{h}_{nc}$ is the natural convection coefficient, which is based on the Nusselt number with the receiver height as characteristic length (Nu_H). In our case the forced convection coefficient is equal to zero, since no wind velocity is considered. Thus, only natural convection losses are taking into account and $\overline{h}_{nc}$ can be obtained from Equations 5.2 and 5.3. In addition, convective heat losses are only calculated on the tube sections exposed to the ambient. The value of Nusselt number is almost invariable with the variation of the cosine angle over the circumferential direction for Reynolds number (Re) 17000 and Prandtl number (Pr) 12, (Yang & Fan, 2012). In the worst case, the error is lower than 10%, if wall temperature is estimated with the mean coefficient and considering the convective coefficient constant in the whole perimeter.

$$\overline{h} = (\overline{h}_{fc}^{3.2} + \overline{h}_{nc}^{3.2})^{1/3.2} = \overline{h}_{nc} \tag{5.1}$$

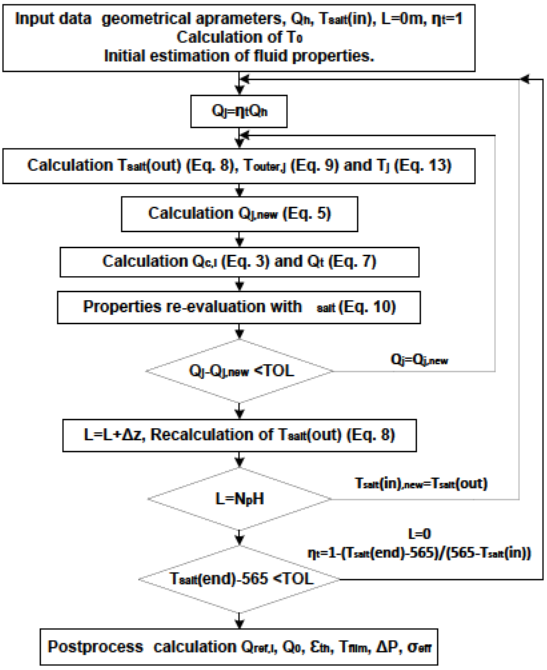

Figure 5.2: Calculation procedure.

$$\overline{h}_{nc} = \overline{Nu}_H \, k_{air}/H \tag{5.2}$$

$$\overline{Nu}_H = 0.098 Gr_H^{1/3} (T_{o,c}/T_{amb}) \tag{5.3}$$

$$Q_{c,l} = \sum_{j=\frac{n}{2}+1}^{n} \overline{h} p_j \Delta z (T_{o,j} - T_{amb}) \tag{5.4}$$

where, k_{air} is the conductive coefficient of the air,Gr_H corresponds to the Grashof number based in the length $Gr_H = g\beta(T_{o,j} - T_{amb})H^3/(\mu/\rho)^2$, $\overline{T}_{o,c}$ represents the mean wall temperature of the tube sections involved in convection, p_j is the perimeter of each tube section, Δz corresponds to the axial increment, and $T_{o,j}$ is the external temperature of the tube wall.

Radiation losses (Q_0 or q_0) are caused by the temperature difference between the tube outer wall or the refractory wall and the sky. To calculate radiation heat losses the net radiation method of Modest (2003) has been used, Equation 5.5. This equation considers grey surfaces that are diffuse emitters, absorbers and reflectors; this fact simplifies the analysis since it allows to calculate radiative heat transfer by balancing the outgoing radiation travelling directly from surface to surface. The values for absorptivity, emissivity and reflectivity coefficients have been obtained from Zavoico (2001); Wade & Slemp (1962); Incropera & Dewitt (1990) and they are shown in Table 5.2.

Table 5.2: Values employed for the absorptivity, emissivities and fouling resistance (Zavoico, 2001; Wade & Slemp, 1962; Incropera & Dewitt, 1990).

Parameters	**Values**
α_i [-]	0.93
ϵ_t [-]	0.87
ϵ_{sky} (30° C), [-]	0.895
ϵ_{n+1}, [-]	0.2
ϵ_{gr}, [-]	0.955
R_{foul}, [m^{2}K/W]	$8.808 \cdot 10^{-5}$

$m = 0, 1, ..., n+1$

$$\sum_{j=0}^{n} \left[\frac{\delta_{m,j}}{\varepsilon_j} - \left(\frac{1}{\varepsilon_j} - 1 \right) F_{m,j} \right] \frac{q_j}{\sigma} - \left[\delta_{m,n+1} - F_{m,n+1} \right] T_{n+1}^4 = \sum_{j=0}^{n} \left[\delta_{m,j} - F_{m,j} \right] T_j^4 - \left[\frac{\delta_{m,n+1}}{\varepsilon_{n+1}} - \left(\frac{1}{\varepsilon_{n+1} - 1} \right) F_{m,n+1} \right] \frac{q_{n+1}}{\sigma} - F_{m,0} \frac{\eta_t q_h}{\sigma} \alpha_i \tag{5.5}$$

Subscripts 1 to n denote the outer tube circular-sections, whereas the refractory wall and the imaginary surface corresponding to the environment are represented by the subscripts $n+1$ and 0, as can be seen in Figure 5.3. δ corresponds to the Kronecker Delta and F represents the view factors between tube sections, ambient and refractory wall.

Figure 5.3 represents the simplified receiver geometry used to solve the problem: an element formed by two semi-tubes placed face to face, a rear surface thermally isolated (refractory wall) and an imaginary front surface that represents the sky. Where the tube pitch is obtained as: $B = P_t - d_o$. Note that in

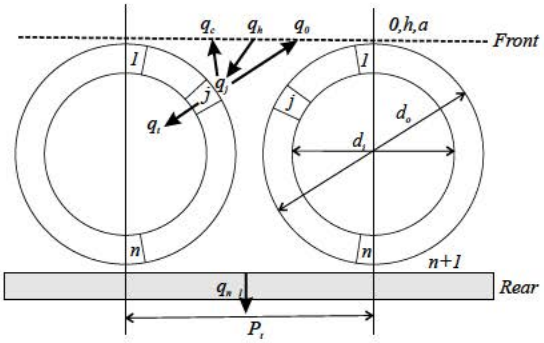

Figure 5.3: Scheme of the ambient, tubes and refractory wall, containing the most important parameters of the problem.

the equivalent circuit of radiation the energy reflected by the heliostats must be included.

The variables to obtain from Equation 5.5 are the radiation flux losses (q_0), the heat flux absorbed by the tubes without convection losses (q_j, $j = 1, ...n$) and the refractory wall temperature (T_{n+1}). Then, it is necessary to know the environmental temperature (T_0), which is calculated according to Equation 5.6 (Berger *et al.*, 1984), the heat flux that arrives to the receiver (q_h), which is obtained from the radiation map, the conductive losses through the refractory wall (q_{n+1}), that in this case are neglected, and the effective outer wall temperature of the tubes for radiation (T_j, $j = 1, ...n$) which are estimated.

$$T_0^4 = \frac{\varepsilon_{sky} T_{sky}^4 + \varepsilon_{gr} T_{amb}^4}{\varepsilon_{sky} + \varepsilon_{gr}} \tag{5.6}$$

In order to minimize the error in the discretization of the tubes, the relative importance of each tube section has been considered using the crossed-strings method to calculate the view factors (F) (Modest, 2003). This method discretizes the tubes in circumferential and axial directions. Choosing tube segments of length $1d_o$ (to fulfil the hypothesis of constant heat flux in each section) the error committed in the view factor, using a 2D method instead a 3D method (much more complex), will be lower than 25%.

Reflective losses ($Q_{ref,l}$) are also calculated using Equation 5.5. They correspond to the last term of the equation (function of $q_h \alpha_i$). Conductive fluxes ($Q_{k,l}$) in circumferential and axial directions can be neglected since they are at least two magnitude orders lower than the heat flux absorbed by the tubes

in the radial direction (Q_t). Therefore, the heat absorbed by the HTF, including every kind of heat losses, is the calculated by Equation 5.7. It is the heat flux absorbed by the tubes obtained by Equation 5.5 less convective heat losses calculated as Equation 5.4.

$$Q_t = \sum_{j=1}^{n} q_j p_j \Delta z - Q_{c,l} \tag{5.7}$$

5.5 Thermal analysis.

In this section the results obtained applying this method to a central receiver are shown, see Figure 5.2. First, the main results has been analysed in an exemplificative receiver configuration formed by $N_p = 18$ panels and a tube external diameter of $d_o = 4.22$ cm. To continue, a broad analysis of different receiver configurations has been done, changing the number of panels and the external diameter of the tubes, in order to find the best receiver design.

For the representative receiver, Figure 5.4 shows the evolution of the thermal power received from the heliostat field, the thermal power absorbed by the tubes as well as the heat losses due to reflection, radiation, convection and conduction, as a function of the distance covered by the salt (L_s) than can be defined as the tube length (H) by the number of panels (N_p) divided by the number of flow paths (N_{fp}). Horizontal axis starts at the north face of the receiver, where the heat flux received is maximum, and finishes at the south face, where the heat flux is minimum, as shown in Figure 5.1.

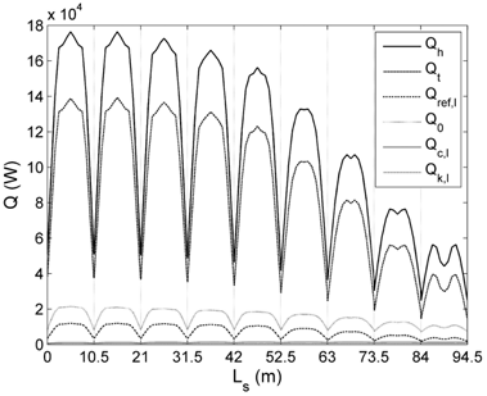

Figure 5.4: Thermal power evolution in the representative receiver.

According to Figure 5.4, the heat power along every tube is symmetric in the axial direction, with a maximum at the centre of the tubes due to the shape of the radiation map. The radiation heat losses are the most important heat losses, much higher than reflection and conduction; this is in contrast to the results found in the literature where both radiation and reflective losses are quite similar or where the reflective heat losses are the highest heat losses (Lata *et al.*, 2008). This difference is attributed to the circumferential temperature variations on the tube outer wall, which is not considered in previous models.

From the data represented in Figure 5.4, the thermal efficiency of the receiver (ε_{th}) can be calculated. It is defined as the ratio between the thermal power absorbed by the tubes (Q_t) and the solar power intercepted by the receiver from the heliostat field ($\eta_t Q_h$). For the representative receiver is equal to 77.81%. This value is lower than other values founded in the literature due to the higher radiation losses obtained. As a consequence, the heliostat field must be larger in order to increase the solar flux reflected by the heliostats.

Simplifiying our problem and assuming no temperature variation in circumferential direction, the thermal efficiency is similar to the one obtained by other authors, as Lata *et al.* (2008) , who obtained thermal efficiencies of 78 - 88%, Jianfeng *et al.* (2010) between 83 - 90% , Li *et al.* (2010) thermal efficiencies comprises from 83 to 91% or Xu *et al.* (2011) equal to 90% and the method employed is equivalent to the method developed by Singer *et al.* (2010). In this case, the heat flux absorbed by the tubes is calculated equally than before. Nevertheless, only one surface of the tube would be taken into account covering the whole perimeter of each axial section simulated. Thus, only one value for wall temperature is considered in each circular section, that is the average temperature of the wall, including also the rear part. As seen previously, the radiation losses will be affected by this simplification because the average wall temperature is not equal to the effective outer wall temperature for radiation for a tube if the circumferential temperature variation is taken into account.

To calculate heat losses, as $\overline{T}^4$ is much lower than $\overline{T^4}$, the simplification leads to lower radiation losses and higher thermal efficiency.

Once the thermal power absorbed by the tubes has been calculated by Equation 5.5, some important working temperatures can be obtained. Bulk temperature (T_{salt}) is the HTF mean temperature and is not affected by circumferential variations, Equation 5.8. T_{salt} must be high enough to avoid HTF freezing and low enough to prevent significative thermal decomposition of the HTF. The outer temperature of each tube section ($T_{0,j}$) is related to the thermal losses,

Equation 5.9. When $T_{0,j}$ increases excessively, corrosion under ambient condition increases too, the adherence of coating to metallic surfaces decreases, and the thermal stresses augment beyond the tube fatigue limit. Finally, the film temperature (T_{film}) in Equation 5.11 is the salt temperature of a thin layer close to the tube inner wall. T_{film} is approximated by the tube inner wall temperature and is the highest temperature of the HTF in the receiver. This temperature is responsible of the HTF stability. Furthermore, at this temperature the HTF corrodes tube material. A small increase of T_{film} above a certain limit can produce a sharp rise of the tube corrosion rate and stress corrosion cracking (SCC).

As explained before, if $T_{salt}(end)$ is not equal to 565 °C, a new iteration will be needed in the calculation process, see Figure 5.2. In the following iteration, the effective outer wall temperature of radiation for each tube section is calculated by Equation 5.12, and Equations 5.8-5.11 have been obtained solving an energy balance in the tubes:

$$T_{salt}(z) = T_{in} + \frac{z}{\dot{m}_s Cp} \sum_{j=1}^{n} q_{t,j} p_j \tag{5.8}$$

$$T_{0,j}(z) = \overline{T_{salt}}(z) + \frac{q_{t,j}}{U_o} \tag{5.9}$$

$$\overline{T_{salt}}(z) = T_{in} + \frac{z}{2\dot{m}_s Cp} \sum_{j=1}^{n} q_{t,j} p_j \tag{5.10}$$

$$T_{film,j}(z) = T_{0,j}(z) - \frac{1}{2} q_{t,j} \frac{d_o ln\left(\frac{d_o}{d_i}\right)}{k_t} \tag{5.11}$$

$$T_j^4 = \frac{1}{z} \int_0^z \left(T_{salt}(z) + \frac{q_{t,j}}{U_o} \right)^4 dz = A^4 - 2A^3 Cz + 2A^2 C^2 z^2 + AC^3 z^3 + \frac{1}{5} C^4 z^4 \tag{5.12}$$

where,$A = T_{in} + q_{t,j}/U_o$, $C = \sum q_{t,j} p_j / (\dot{m}_s Cp)$ and U_o is the global heat transfer coefficient, defined as follows:

$$\frac{1}{U_o} = \frac{1}{\overline{h}} \frac{d_o}{d_i} + \frac{d_o ln\left(\frac{d_o}{d_i}\right)}{2k_t} + R_{foul} \frac{d_o}{d_i} \tag{5.13}$$

where the fouling resistanceR_{foul} is indicated in Table 5.2.

Figure 5.5 shows the evolution of these temperatures for the representative receiver. It can be observed how the salt temperature increases from one panel to the following one, starting at 290 °C and ending at 565 °C. In this figure, several curves for the outer wall temperature (maximum, mean and minimum) can be observed, which represent different circumferential positions of the representative tube of each panel. The curve that represents the maximum film and outer wall temperatures is in the front section of the tubes, where the view factor to the heliostat field is maximum. The curve is symmetric in every tube, due to the radiation map used. The curve for the minimum values is at the rear side, where the view factor to the refractory wall is maximum, and its behaviour is equal to the salt bulk temperature (not symmetric).

In addition, overwieving the whole figure the panel that reach the maximum wall and film temperatures is found at the east/west side of the receiver, thus the temperature control of this panel is critical. The maximum is not observed in the northen panels, where the heat flux is maximum, because the salt temperature is minimum in this zone and it is capable of absorbe more quantity of energy. Whereas in the fifth panel, which corresponds to the west/east side of the receiver, the heat flux is still high, but the salt temperature is also high, resulting in the maximum temperature. Finally, at the southern panels the heat flux is low, so in these panels the wall temperature is the lowest.

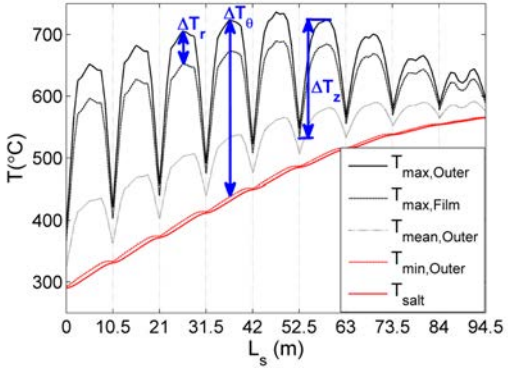

Figure 5.5: Temperature evolution in the representative receiver.

One of the most important characteristics of the assumptions made in this analysis is the wall temperature circumferential variations. Figures 5.6(a) and 5.6(b) show in detail the evolution of the external wall temperature in different

circumferential positions of each tube of the representative receiver. Figure 5.6(a) represents the temperature evolution for one of the salt path in the receiver, while Figure 5.6(b) corresponds to the temperature evolution for the whole receiver in three-dimensions. The temperature in the rear side of the tubes (maximum view factor to the refractory wall) is much lower than in the front side and its value is practically uniform, whereas in the front face the wall temperature follows a parabolic distribution. Therefore, for the representative receiver, the maximum outer wall temperature is at the tube front face of the eastern/western panels and it is equal to 686 °C.

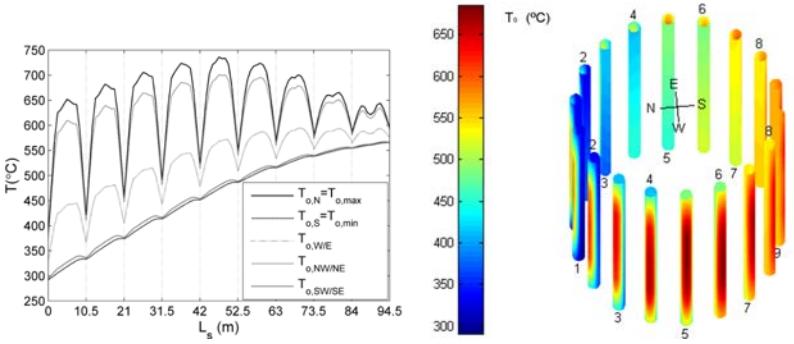

(a) (b)

Figure 5.6: (a) Outer tube wall temperature evolution in the representative receiver.(b) Outer wall temperature distribution in the whole representative receiver.

Note that the external wall temperature is a decisive factor for the material thermal stress, but it is not as critical as film temperature in the design of the receivers. Therefore, the maximum value for the film temperature has to be analysed in order to avoid salt decomposition and tube corrosion. In Figure 5.7 the axial and circumferential variations of the film temperature are included in a 3D representation of the receiver. As Figure 5.5 shows, the maximum film temperature is in the east/west side of the receiver, reaching the highest value at the front part of the tubes (highest view factor to the heliostat field), whereas it is practically constant for the rest of circumferential angles.

In the representative receiver, the maximum film temperature reaches 642 °C, as the tube material conductivity is similar for all the metals mentioned in this text, for all them the maximum film temperature is more or less the same. That means that a receiver made with 316 stainless steel or Inconel 625-LCF

presents risk of severe corrosion and therefore only a receiver made of Incoloy 800H could support this temperatures without risk of early failure. Besides, the salt close to the walls could decompose. However, as demonstrated previously, the fraction of the flow affected by this high temperature is less than 0.014%.

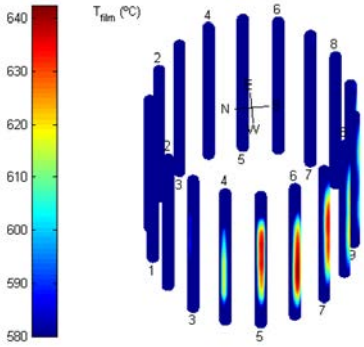

Figure 5.7: Film temperature distribution for the whole representative receiver.

To conclude the thermal analysis, the maximum film temperature,which is the most restrictive temperature of the problem, has been studied as a function of the number of panels (from 16 to 26) and of the external diameter of the receiver tubes (from 1.37 cm to 6.03 cm) (Figure 5.8). Then the number of tubes in each panel and in the receiver is calculated taking into account that each panel has an entire number of tubes, as the tube thickness (th) and tube pitch (B) do not vary, it will affect to the total effective surface of the receiver.

Figure 5.8 shows that the lowest temperature is obtained for the highest number of panels and the smallest diameters. For the configuration analyzed, a tube diameters of 6.03 cm is not desirable for any material, because the maximum film temperature reached is higher than 650 °C. For a diameter of 4.83 cm only receivers with more than 20 panels are suitable using Incoloy 800H. In the case of a diameter of 4.22 cm, a receiver formed by 16 panels cannot be used, but a receiver with higher number of panels is valid for Incoloy 800H. In addition, for this diameter, a receiver of 24 or 26 panels could use tubes made of Inconel 625-LCF. Finally, for stainless steel receivers, only combinations of a high number of panels and external diameters of 1.37, 1.71 and 2.13 cm avoid severe corrosion.

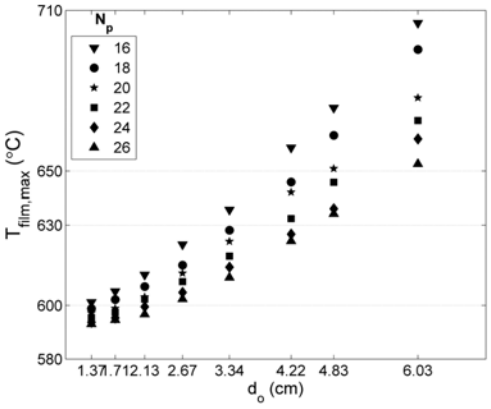

Figure 5.8: Film temperature as a function of the number of panels and the diameter of the tubes of the receiver.

5.6 Mechanical analysis.

The incident solar flux on the receiver produces temperature gradients in the tube wall large enough to develop plastic strains. Plastic strains are cumulative and the tubes will eventually fail due to low cycle fatigue. Moreover, the combination of thermal stress and corrosion can produce SCC in the tubes. Then ASME (2011) provided the SPT Solar Two basis for calculating tube strains and fatigue life for a molten nitrate salt receiver operating at temperatures from 427 °C to 760 °C.

The temperature in the tubes of an external receiver cause thermal stress in the three directions: axial, radial and circumferential. The three directions of thermal stresses are independent to each other (Fauple & Fisher, 1981). According to the results obtained in Figure 5.5 axial ($\Delta T_z/H$) and circumferential ($\Delta T_\theta/p$) temperature gradients are almost one order of magnitude lower than the radial gradient ($\Delta T_r/th$), therefore only the efects of the radial stress, in the three directions, have been considered in this study. Thereby, the governing thermal stress equation for radiant tubes (Irfan & Chapman, 2009) is:

$$\sigma_{eff,max} = \frac{\Delta T_r \alpha E}{2(1-\varsigma) ln\left(\frac{d_o}{d_i}\right)} \left(1 - \frac{2d_i^2}{d_o^2 - d_i^2}\right) \simeq \frac{E\alpha}{2(1-\varsigma)k_t} q_{t,j} th \qquad (5.14)$$

Is commonly accepted that the maximum thermal stress in the tubes ($\sigma_{eff,max}$) must be lower than 40% to 50% of the ultimate tensile strength (UTS) to pre-

vent failure due to fatigue. Figure 5.9 shows the evolution of the ratio of thermal stress to ultimate tensile strength in the representative receiver. The trend of this parameter is similar to the wall and film temperature evolutions; being symmetrical respect to the axial direction with the maximum at the middle of the tubes, except for the south panel. The highest thermal stress occurs in the east/west side of the receiver, but always is lower than 0.35 times UTS. In this case the thermal stresses never surpass the fatigue limit and therefore the film temperature is the critical parameter in the receiver designs considered in this study. In addition, the maximum wall temperature and the maximum thermal stress take place in the same tubes.

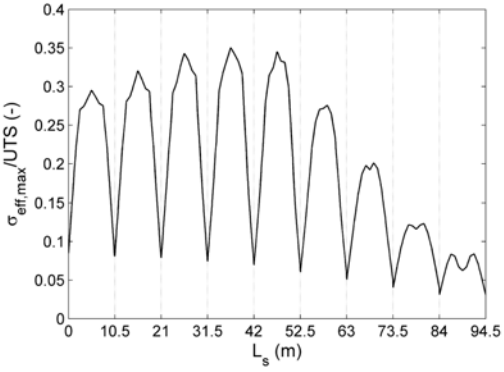

Figure 5.9: Evolution of ratio maximum thermal stress - ultimate tensile strength in the representative receiver.

Figure 5.10 represents the ratio maximum thermal stress to UTS as a function of the number of panels (from 16 to 26) and the tube diameters of the receiver (from 1.37 cm to 6.03 cm), in order to analyze the thermal stress behaviour for different receiver designs. As Figure 5.10 shows, $\sigma_{eff,max}$ is mainly a function of the heat flux absorbed by the tubes and then of the effective area of the receiver, which depends on the total number of tubes in the receiver. The highest tube diameter has the highest thermal stress, as in the film temperature analysis.

In all the cases showed in Figure 5.10 the thermal stress is lower than the limit imposed, being this paremeter less restrictive than the film temperature. Therefore, the thermal stresses, are not a critical parameter under the solar radiation conditions used in this work.

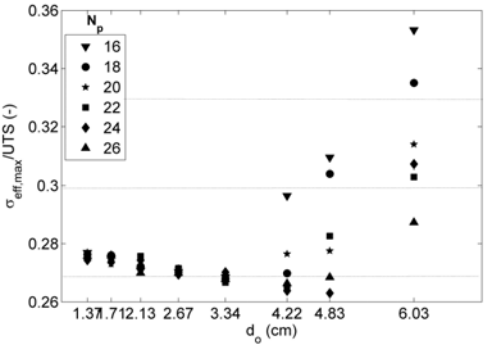

Figure 5.10: Ratio maximum thermal stress - ultimate tensile strength as a function of the number of panels and the diameter of the tubes of the receiver.

5.7 Hydrodynamic analysis.

A receiver is composed of straight, elbows, and abrupt expansions and contractions. For the hydrodynamic analysis, the receiver can be divided into basic units. Figure 5.11 contains an example of a basic unit which includes a tube joined to the inlet and outlet collectors. A panel is created by connecting in parallel several of these tube units. In this section, the whole receiver, and not only one tube per panel, is considered. To assure safety operation of the plant, avoiding overpressure in the manifolds, the maximum pressure drop (ΔP) cannot exceed 20 bar.

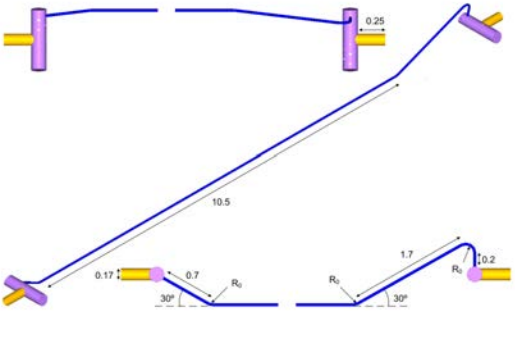

Figure 5.11: Scheme of an exemplificative tube of an external receiver, with the parameters for the pressure drop calculation.

For smooth tubes with elbow curvature radius greater than the tube internal diameter ($R_o = 0.13$ m), the pressure drop of each panel is obtained as the sum of the pressure drop in elbows, tube fitting and straight tubes as follows (Idelchik, 1986):

$$\Delta P = \sum_{straight} f_r \frac{H}{d_i} \frac{\dot{m}_s^2}{2\rho S^2} + \sum_{exp/con} K \frac{\dot{m}_s^2}{2\rho S^2} + \sum_{elbow} \left[\left(1.3 - 0.29 ln \left(\frac{Re}{10^5} \right) \right) 0.21 \left(\frac{R_o}{d_i} \right)^{-\frac{1}{4}} A_1 \right] \frac{\dot{m}_s^2}{2\rho S^2} \tag{5.15}$$

Where A_1 is 0.45, 1 and 1.16 for 30°, 90° and 120° elbows, is the expansion and contraction resistance coefficient (Figure 5.11) (Idelchik, 1986), f_r is the Darcy friction factor, which can be calculated explicitly for smooth and rough tubes using the correlations proposed by **?**. S is the flow area of each section. The fluid properties are calculated at bulk temperature of the molten salt in each Δz.

Figure 5.12 shows the pressure drop as a function of the number of panels of the receiver (from 16 to 26) and the diameter of the tubes (from 1.37 cm to 6.03 cm). Additionally three isothermal lines are represented to assist with the design of the receiver. They indicate the maximum temperature available for the three main materials that could be used in the receivers. The pressure drop, in Figure 5.12, increases with the number of panels, because a higher number of panels means a higher number of tube passes, and decreases with the diameter of the tubes, since higher diameters prodecure a reduction of the salt velocity. Therefore, the behaviour of the pressure drop is opposite to the film temperature and thermal stresses. Then, a compromise between the different variables is needed for a proper design of the configuration.

For example, for tubes of 6.03 cm diameter the pressure drop is the lowest (Figure 5.12), but this diameter cannot be used due to the high film temperature. Diameters of 1.37 and 1.71 cm, suitable for all the materials, are not recommended due to the high pressure drop. Therefore, the best design, taking into account both, pressure drop, film temperature and thermal stress, seems to be a high number of panels and tube diameter of 4.83 and 4.22 cm using Incoloy 800H as tube material, or low number of panels with diameters of 3.34 and 2.67 cm using Incoloy 800H or Inconel 625-LCF.

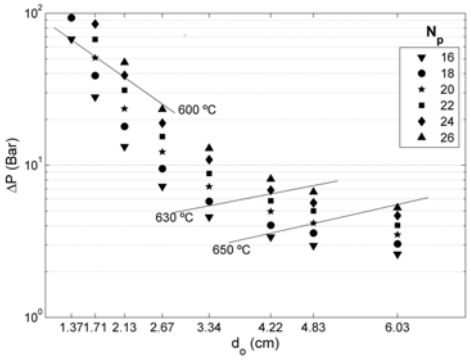

Figure 5.12: Pressure drop as a function of the number of panels and the diameter of the tubes of the receiver.

5.8 Receiver configuration selection.

The optimal receiver design, from a viewpoint of the thermal and mechanical point of view, would have a reduced number of panels and tubes of small diameters. However, small diameter tubes produces a great pressure drop and an extremely large number of tubes and clips, which means a high number of welded zones that increase the posibility of damage in the tubes (corrosion spots). Besides, an elevated number of panels means high pressure drop and a high number of headers and structural elements. Therefore, a compromise between the different variables is necesary in order to find the optimal receiver configuration.

Once thermal, mechanical and hydrodinamical variables fulfil the restrictitions, the decisive factor to find the best receiver design, would be to maximize thermal efficiciency of the receivers in order to reduce the number of heliostats and therefore decrease the initial capital cost. Another strategy could be the minimization of the number of tubes and clips with the aim of reducing the price of the receiver and the posibility of damage in the tubes. Nevertheless, a detailed economical study should be done to find which is the best strategy for the design of the optimal receiver based on a combination of thermal, mechanical, hydrodinamical and economical reasons.

Finally, Figure 5.13 shows the efficiency of the receiver as a function of the number of panels (from 16 to 26) and the diameter of the tubes (from 1.37 cm to 6.03 cm). In this figure, the limiting film temperature has been additionally

indicated for the different materials, the total number of tubes and the pressure drop in the receiver for several relevant designs. The efficiencies are in a range from 74% to 78%. And the smallest efficiencies are found for diameters of 4.83 and 6.03 cm.

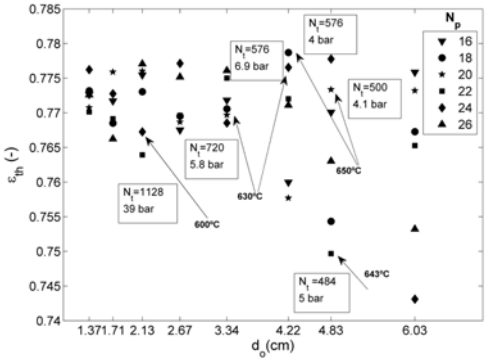

Figure 5.13: Receiver efficiency as a function of the number of panels and the diameter of the tubes of the receiver.

According to Figure 5.13, the receiver efficiency is a function of the total number of tubes and is nearly independent of the tube diameter and number of panels.

Taking into account the maximum receiver thermal efficiency and the restrictions of the other variables analyzed, the best receiver design for the nominal condition is a receiver of 18 panels and 4.22 cm of tube external diameter, which fulfil the maximmum film temperature for Incoloy 800H (Figure 5.8). This design counts on a total of 576 tubes and 10 tons of Incoloy 800H, and leads to a thermal efficiency close to 78% and a pressure drop of 4 bar.

5.9 Conclusions.

A simple method to analyze the thermal behaviour of a molten salt central receiver was presented in this work. The method takes into account the circumferential and axial vatiations of tube wall temperature and it involves low computational cost.

The results show that the wall temperature variations have an important influence on the heat losses of the receiver given by radiation. The effective wall

temperature for radiation is higher than the mean wall temperature, specially if the rear temperature of the tubes is taken into account. Higher thermal losses imply a lower thermal efficiency of the receiver. This explains why the thermal efficiency obtained with the method proposed in this work is smaller than the thermal efficiencies reported in the literature.

Besides, both thermal and mechanical critical points of the receivers are located in the east/west panels of the receiver. Therefore, these panels have to be controlled to avoid damages and assure their lifetime. Other important variables to consider in the receiver design are the number of panels and the diameter of the tubes, because their variations have an apreciable effect on the thermal, mechanical and hydrodynamic parameters of the receiver.

Finally, from the thermal and mechanical point of view, the results show that the optimal design of the receiver would require a reduced number of panels and tubes of small diameters. However, small diameter tubes and a high number of panels mean high pressure drops. Therefore, a compromise between the different variables is needed in order to find an optimal receiver configuration.

Nomenclature

B	Tube pitch [m]
C_p	Salt specific heat [J/kg° C]
D	Receiver diameter [m]
d	Tube diameter [m]
E	Modulus of elasticity [Pa]
F	View factor [-]
f_r	Darcy friction factor [-]
H	Receiver/ Tube length [m]
h	Convective coefficient [W/m^{2}K]
K	Expansion and contraction resistance coefficient [-]
L	Length [m]
$\dot{m}_s$	Salt mass flow rate [kg/s]
N	Number of elements [-]
P	Pressure [Pa]
P_t	Distance between tube centres [m]
p	Perimeter [m]
Q	Heat power [W]

Q_{th}	Thermal power of the plant [W]
q	Heat flux [W/m^2]
q_j	Heat flux absorbed by the tubes without convection losses [W/m^2]
q_t	Heat flux absorbed by the salt[W/m^2]
R_{foul}	Fouling resistance [m^2K/W]
S	Flow surface [m^2]
T	Temperature [° C]
T_j	Effective tube outer wall temperature for radiation [° C]
th	Tube thickness [m]
U_o	Global heat transfer coefficient [W/m^{2}K]
UTS	Ultimate tensile strength [Pa]
v	Wind velocity [m/s]

Greek letters

α	Coefficient of thermal expansion [° C$^-$1]
α_i	Solar absorptivity [-]
β	Gas volumetric expansion coefficient [K$^-$1]
ΔP	Pressure drop [Pa]
δ	Kronecker delta [-]
ϵ	Emissivity [-]
ϵ_{th}	Thermal efficiency of the receiver [-]
ϕ	Relative humidity [%]
η_t	Correction factor [-]
μ	Absolute viscosity [Pas]
ρ	Salt density [kg/m^3]
σ	Stefan-Boltzmann constant [W/m^{2}K^4]
$\sigma_{eff,max}$	Maximum thermal stress [Pa]
ς	Poisson coefficient [-]

Subscripts

amb	Ambient
c	Convection
fc	Forced convection
fp	Flow path
gr	Ground

h	Heliostat
i	Internal wall
in	Inlet
k	Conduction
nc	Natural convection
l	Heat losses
o	Outer wall
out	Outlet
p	Panel
ref	Reflection
s	Molten salt
salt	Bulk
t	Tube
0	Radiation losses

Abbreviattions

HTF	Heat transfer fluid
SCC	Stress corrosion cracking
SPT	Solar power tower

References

Allen, C.B. & Janz, G.J. 1980 Molten-salts safety and hazards an annotated-bibliography. *Journal of Hazardous Materials* 2, 145–175.

ASME 2011 ASME Boiler and Pressure Vessel Code, Section II - Materials. *Tech. Rep.*. American Society of Mechanical Engineers, New York.

Berger, X., Buriot, D. & Garnier, F. 1984 About the equivalent radiative temperature for clear skies. *Solar Energy* 32 (6), 725–733.

Boerema, N.; Morrison, G.; Taylor R. & Rosengarten, G. 2013 High temperature solar thermal central-receiver billboard design. *Solar Energy* 97, 356–368.

Bradshaw, R.W. & Goods, S.H. 2001 Corrosion of Alloys and Metals by Molten Nitrates. *Tech. Rep.*. Sandia National Laboratories, Albuquerque, SAND2000-8727.

Burgaleta, J.I., Arias, S. & Salbidegoitia, I.B. 2009 Operative advantages of a central tower solar plant with thermal storage system. In *SolarPACES*, p. n 11720. Berlin, Germany: SolarPACES.

Clausing, A. 1981 Analysis of convective losses for cavity solar central receivers. *Solar Energy* 27, 295–300.

Cui, Haiting, Wang, Zhenhui, Guo, Yanshu, Xu, Weiqiang & Yuan, Xiugan 2006 Thermal performance analysis on unit tube for heat pipe receiver. *Solar Energy* 80 (7), 875–882.

Dehghan, A.A. & Behnia, M. 1996 Combined natural convection conduction and radiation heat transfer in a discretely heated open cavity. *ASME Journal of Heat Transfer* 118, 54–56.

Falcone, P.K 1986 *A handbook for solar central receiver design*. Livermore, California: Sandia National Laboratories.

Fauple, J.H. & Fisher, F.E. 1981 *Engineering design: a synthesis of stress analysis and material engineering*. New York, USA: Wiley.

Garbrecht, Oliver, Al-Sibai, Faruk, Kneer, Reinhold & Wieghardt, Kai 2013 CFD-simulation of a new receiver design for a molten salt solar power tower. *Solar Energy* 90, 94–106.

Gielen, Dolf 2012 Renewable energy technologies: cost analysis series. Concentrating Solar Power. *Tech. Rep.* 2/5. IRENA, Albuquerque.

Idelchik, I.E. 1986 *Handbook of Hydraulic Resistance*, 3rd edn. New York, USA: Begell House.

Incropera, F.K. & Dewitt, D.P. 1990 *Introduction to heat transfer*, 2nd edn. Indiana, USA: John Wiley and Sons, Purdue University.

Irfan, Mohammad a. & Chapman, Walter 2009 Thermal stresses in radiant tubes due to axial, circumferential and radial temperature distributions. *Applied Thermal Engineering* 29 (10), 1913–1920.

Jianfeng, Lu, Jing, Ding & Jianping, Yang 2010 Heat transfer performance of an external receiver pipe under unilateral concentrated solar radiation. *Solar Energy* 84 (11), 1879–1887.

Kennedy, C.E. 2002 Review of mind-to-high-temperature solar selective absorber materials. *Tech. Rep.*. NREL, Colorado, USA, NREL 2002/TP-520-31267.

Kolb, G.J.; Ho, C.K.; Mancini T.R. & Gary, J.A. 2011 Power Tower Technology Roadmap and Cost Reduction Plan. *Tech. Rep.* April. Sandia National Laboratories, Sandia National Laboratories, Albuquerque.

Lata, Jesús M., Rodríguez, Manuel & Álvarez de Lara, Mónica 2008 High Flux Central Receivers of Molten Salts for the New Generation of Commercial Stand-Alone Solar Power Plants. *Journal of Solar Energy Engineering* 130 (2), 1–5.

Li, Xin, Kong, Weiqiang, Wang, Zhifeng, Chang, Chun & Bai, Fengwu 2010 Thermal model and thermodynamic performance of molten salt cavity receiver. *Renewable Energy* 35 (5), 981–988.

Liao, Zhirong, Li, Xin, Xu, Chao, Chang, Chun & Wang, Zhifeng 2014 Allowable flux density on a solar central receiver. *Renewable Energy* 62, 747–753.

Lim, Sehwa, Kang, Yongheack, Lee, Hyunjin & Shin, Seungwon 2014 Design optimization of a tubular solar receiver with a porous medium. *Applied Thermal Engineering* 62 (2), 566–572.

Mar, R.W. & Kramer, C.M. 1980 Pressure-temperature-composition relationships for heated draw salt systems. *Solar energy materials* 5, 71–79.

Miliozzi, A., Giannuzzi, G.M., Tarquini, P. & La Barbera, A. 2001 Fluido termovettore: dati di base della miscela di nitrati di sodio e potassio. *Tech. Rep.*. ENEA, Italy, ENEA/SOL/RD/2001/07.

Modest, F Michael 2003 Radiative Heat Transfer. In *Radiative Heat Transfer*, Second edi edn. (ed. Elsevier Science), chap. 5. RADIATI, pp. 162–197. New York, San Francisco, London.

Nissen, D. a. & Meeker, D. E. 1983 Nitrate/Nitrite Chemistry in NaN03-KN03 Melts. *Inorg. Chem.* 22 (June 1980), 716–721.

Pacheco, J.E. 2002 Final Test and Evaluation Results from the Solar Two Project. *Tech. Rep.* January. Sandia National Laboratories, Albuquerque, SAND2002-0120.

Persky, M.J. & Szczesniak, M. 2008 Infrared, spectral, directional-hemispherical reflectance of fused silica, Teflon polytetrafluoroethylene polymer, chrome oxide ceramic particle surface, Pyromark 2500 paint, Krylon 1602 paint, and Duraflect coating. *Applied Optics* 47, 1389–1396.

Siebers, D L & Kraabel, J S 1984 Estimating Convective Energy Losses From Solar Central Receivers. *Tech. Rep.*. Sandia, Livermore.

Singer, C.; Buck, R.;, Pitz-Paal, R. & MuÌĹller-Steinhagen, H. 2010 Assessment of Solar Power Tower Driven Ultrasupercritical Steam Cycles Applying Tubular Central Receivers With Varied Heat Transfer Media. *Journal of Solar Energy Engineering* 132 (4), 041010: 1–12.

Wade, W.R. & Slemp, W.S. 1962 Measurements of total emittance of several refractory oxides, cements, and ceramics for temperatures from 600 °F to 2000 °F. *Tech. Rep.*. NASA, USA, Technical Note D-998.

Xu, Chao, Wang, Zhifeng, Li, Xin & Sun, Feihu 2011 Energy and exergy analysis of solar power tower plants. *Applied Thermal Engineering* 31 (17-18), 3904–3913.

Yang, M.; Yang, X.;, Yang, X. & Ding, J. 2010 Heat transfer enhancement and performance of the molten salt receiver of a solar power tower. *Applied Energy* 87 (9), 2808–2811.

Yang, X.; Yang, X.; Ding J.; Shao Y. & Fan, H. 2012 Numerical simulation study on the heat transfer characteristics of the tube receiver of the solar thermal power tower. *Applied Energy* 90 (1), 142–147.

Zavoico, A.B. 2001 Solar Power Tower: Design Basis Document. *Tech. Rep.* July. Sandia National Laboratory, San Francisco, SAND2001-2100.

CHAPTER
SIX

Design of external solar receivers for the whole range of operation: Flow patterns selection

Contents

Scientific Contributions

- M.R. Rodríguez-Sánchez, A. Sánchez-González, C. Marugán-Cruz, D. Santana. Flow patterns of external solar receivers. Submitted for publication to Solar Energy.

6.1 Abstract

The design of flow paths of solar-central external-receiver with molten salt as heat transfer fluid is crucial to increase the solar plant availability and for the

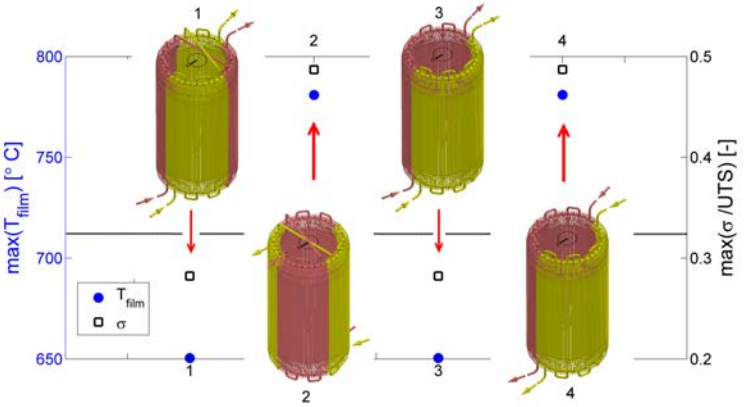

secure receiver operation with respect to the material failure. The parameters that most affect the start-up and shut-down of the receiver are the direct normal irradiance, the sun elevation angle, and the ambient conditions. In addition, the limits of the feed-pump system and the minimum turbulent Reynolds number also limit the hours of operation to avoid receiver damage. Under nominal conditions of operation the most influential factors are the film temperature, the thermal stresses and the pressure drop.

In this study, a whole year range of operation has been analysed. Different flow pattern configurations have been simulated including simple or multiple flow paths. In the latter case it has been also studied configurations including crossover between flow paths. The analysis of the different configurations has been done based on thermal, mechanical and hydrodynamics limits in order to increase the global efficiency of the power plant. In view of the results special attention has to be paid to the crossover to equalise the solar flux that reaches both flow paths in the start-up and shut-down. However, to maintain good levels of thermal efficiency close to midday it is more important a good distribution of the solar flux than get a flux balance between paths.

The configuration that maximizes the thermal efficiency includes two flow paths in which the flow configuration varies along the day: one crossover just before the middle of the path in the sunrise and sunset, and none crossover for high solar flux. If the configuration of crossovers cannot be varied, it is recommended to avoid the use of crossovers in the receiver.

6.2 Introduction

In Solar Power Tower (SPT) the solar direct irradiation is concentrated on the receiver by thousands of individually sun-tracking mirrors to reach peak solar flux, up to 1 MW/m^2 Lata *et al.* (2008). In the receiver the radiation energy is transferred by conduction and convection to the heat transfer fluid (HTF) reaching high temperatures that allows to generate electricity in a power block.

The external central receiver is placed at the top of a tower, configured as a 360° cylindrical tubular receiver, formed by panels made of thin walled tubes. The HTF follows a serpentine path, passing through adjacent panels. The flow pattern of each receiver can vary with the ambient conditions and operation requirements (see Figure 6.1). Wagner (2008) analysed eight simple flow configurations, that later have been employed in the design software System Advisor Model of NREL Golden (2015). Figure 6.1 shows different configurations, notice that Figures 6.1.5 to 6.1.8 are composed by a single flow path in which the whole HTF flows through all the panels of the receiver (note that the inlet and the outlet of the receiver are in adjacent panels of the northern or southern side), whereas Figures 6.1.1 to 6.1.4 have two symmetric flow paths, and half HTF mass only flows through one half of the panels, from north to south or from south to north. In addition, both paths could be crossed one time (Figures 6.1.1 and 6.1.2) or none (Figures 6.1.3 and 6.1.4).

Figure 6.2 shows the top view of a receiver formed by 18 panels divided in two flow paths without crosses. The panels have been named from north to south and considering west and east orientation; this notation has been used from now on along the study.

Wagner (2008) studied the different flow configurations based on the thermal losses of the receiver. He showed that configurations with only one flow path have higher pressure drop and increase the parasitic consumption. Hence to reach higher thermal efficiency of the receiver the panels must be arranged in two parallel paths (configurations 1 to 4). Of the four multiple flow patterns analysed the most efficient configurations, in the northern hemisphere, are south-to-north flow with none or one crossover (configurations 4 and 2, respectively). This is so because the solar peak flux is maximum in the north side of the receiver. Wagner claimed that if the cold HTF enters by the northern panels its temperature increases rapidly, and the hot HTF that travels to the west-south/east-south panels contributes to elevate the tube wall temperature of the receiver, increasing unnecessary the heat losses by radiation and convection.Wagner also claimed that thermal stress is highest in the panels where the

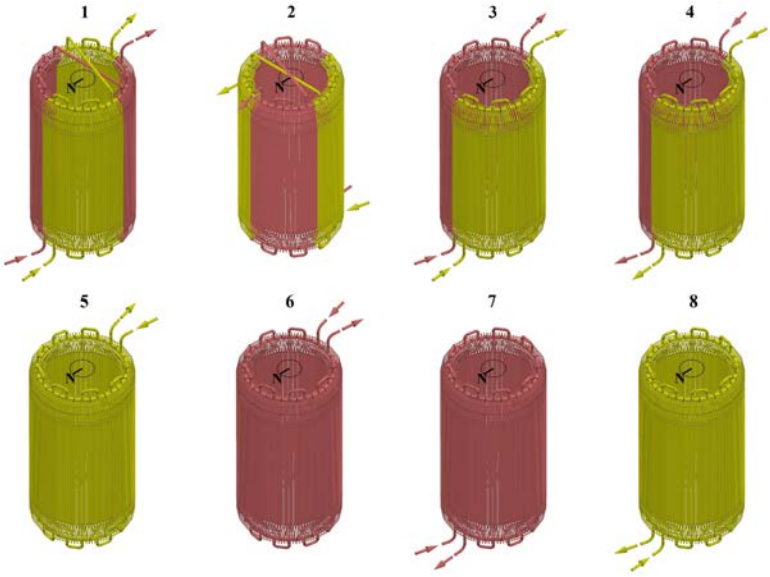

Figure 6.1: Receiver scheme for the eight flow pattern configurations proposed.

flux on the receiver surface is highest regardless of fluid temperature. At solar noon the incident flux in the last panels of the south-to-north flow is maximum and the salt temperature is elevated causing problems of thermal stress.

The solar-noon of the spring equinox is usually used as design point of SPT Kistler (1986); Winter *et al.* (1991). Collado (2009) studied the heliostat field efficiency for different layouts; he showed that at the solar-noon the efficiency of a circular heliostat field is symmetric with respect to the north-south axis. In addition, Augsburger & Favrat (2013) proved that the 12 solar time presents a symmetric flux radiation map on the receiver with respect to the north-south axis for a heliostat field like Gemasolar, locating the peak flux in the northern panels of the receiver, in the northern hemisphere. Hence, for a two flow path receiver configuration the solar flux absorbed in solar-noon by both flow paths is the same, and the crossover configuration is in the background. Nevertheless, in the northern hemisphere during the sunrise and sunset the maximum solar radiation is displaced to the western and eastern panels of the receiver, respectively; producing an energy asymmetry between both flow paths. At these moments the crossovers are particularly important.

Kolb & Gary (2011) predicted an availability of 90% for commercial plants

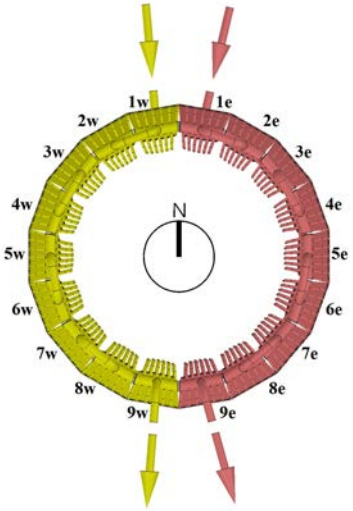

Figure 6.2: Top view of a receiver scheme with panel numeration.

in 2020, however until the moment only 85% has been achieved Dhyia Aidroos & Saeed Obaid (2015). They identified the receiver system as one the most important causes of SPT unavailability. In this paper the optimal flow configuration has been analysed taking into account thermal, mechanical, and hydrodynamic factors to increase the receiver availability during a whole year, as well as to increase the overall efficiency of the SPT.

Firstly, the critical operational limits which assure the receiver service have been established. The operation limits of the receiver are the minimum mass flow rate, which determines the start-up and shut-down of the receiver; the maximum film temperature to avoid tube material corrosion and molten salt decomposition; and maximum thermal stresses to avoid fatigue and cracking. Once the operational limits have been defined, it is possible to determine the most adequate receiver flow configuration of the eight proposed, for the design-point. In this step an optimum receiver design formed by tubes of 4.22 cm of diameter arranged in 18 panels,and previously obtained by Rodríguez-Sánchez & Santana (2014*a*) has been usedas particular case of study.

Secondly, the possible hours of operation during a whole year for the selected configuration have been analysed, and the relation between the direct normal

irradiation (DNI) and the elevation angle of the sun (by means of the flux density on the receiver) that indicates the hour at which the receiver could start/stop to operate has been calculated. At the same time it is possible to determine the critical hours of operation of a receiver:

- First hours in the morning and last hours in the afternoon. During these hours the most critical parameters are the flux asymmetry between flow paths, and the internal convective heat transfer coefficient (defined by the molten salt velocity).

- Hours in which the flux peak is high but the flux is non-symmetrically distributed between paths. In these hours the most critical factors are the film temperature and the thermal stresses.

Finally, an example of each critical hour has been analysed in order to find the crossover position that optimizes the whole range of operation of the receiver and increases the receiver availability, increasing also the annual power generated for the SPT and its global efficiency.

6.3 Receiver and field description

Rodríguez-Sánchez & Santana (2014*a*) studied the optimum receiver design based on thermal, mechanical, and hydrodynamic analysis for a SPT of 120 MWt with molten salt as HTF, located in Seville (Spain). The design point of that receiver was the solar-noon of the spring equinox. The receiver consists of 10 m of height and 8.4 m of diameter of Incoloy 800H, formed by 18 panels of 32 tubes each. The external tube diameter is 4.22 cm and the internal 3.89 cm. The receiver has a total weight of 10 tons of stainless steel. In addition, the receiver is divided in two flow paths from north to south, and at nominal conditions it fulfils the maximum film temperature for Incoloy 800H. However, in the previous work neither the detailed analysis of the flow pattern nor the number of hours in which the receiver could work under safety operation were considered.

In this paper the flow pattern configuration of the receiver has been optimized. To calculate the flux density incident on the receiver, the computational optical model developed by Sánchez-González & Santana (2015) based on the analytic function at the image plane Collado & Turégano (1986) has been

employed. The heliostat field has been configured as Gemasolar, whose 2650 heliostat coordinates were retrieved from a scaled aerial photograph. Square heliostat mirrors are 10.95 m side with 0.88 reflectivity and 0.95 cleanliness. Sun, slope and tracking errors are 2.51, 2.6 and 2.1 mrad, respectively.

In the absence of specific aim-point information, a previously reported multi-aiming strategy Sánchez-González & Santana (2015) has been applied in the computational model. The aiming factor has been adjusted for the different days and hours, in order to reduce the tube wall temperature as much as possible with an acceptable level of receiver efficiency. In addition, the number of heliostats aiming at the receiver has been reduced in days of high insolation.

6.4 Operation limits

The operational strategy in SPT is to drain the molten-salt each night and turn-off the heat trace in order to reduce the parasitic power consumption of the plant Pacheco *et al.* (1995). In the early morning the panels of the receiver are preheated with the heliostats before they are filled with molten salt. Vant-Hull (2002) showed that this preheating process is typically accomplished in 15 minutes using a maximum flux density of 36 kW/m^2. Consequently, the external receivers could start-up as early as the blocking and shadowing factors (caused by low elevation angles of the sun) allow it.

After sunrise, the receiver starts-up when the heat absorbed by the receiver is enough to assure the proper operation of the receiver. There are authors that claims that the receiver starts to operate at 10° of sun elevation angle Falcone (1986), 1986) , while others say that the limiting elevation angle is 15° Collado & Guallar (2013). Delay the start-up to a sun elevation angle of 10° or 15° represents a loss of 0.7 or 1hours of possible operation per day, respectively.

In this research, it has been studied the hour at which the receiver could start to operate, as long as the sky is free of cloud and haze, and taking into account that there are certain thermal, mechanic and hydrodynamic limits that the receiver must not overpass. The operational limits has been calculated with the receiver thermal model developed by Rodríguez-Sánchez & Santana (2014*a*). It has been imposed that in both paths the salt enters at 290 °C and exits at 565 °C, at the expense of the mass flow rate variation.

To carry out the analysis only an averaged representative day per month has been studied since the solar angle variation between two consecutive days is negligible, and the hourly DNI of a whole year is impossible to predict.

The hourly statistics for direct normal solar radiation and the average hourly statistics for dry bulb temperature in Seville have been obtained from IWEC data**?**. Each of them corresponds to the most representative month of a sample of years from 1982 to 1993.

6.4.1 Minimum mass flow rate

The operational range of the bulk temperature of the salt is limited by its freezing point and by its decomposition rate. The typical work range of a molten salt receiver is from 290 ° C at the inlet to 565 °C at the outlet. Hence, it is possible to calculate the nominal mass flow of the receiver for a given receiver power. The nominal mass flow for a receiver of 120 MWt is 290 kg/s .Where corresponds to the average specific heat of the salt at mean work temperature, 1516.5 J/kgK Zavoico (2001). In this study the minimum allowable mass flow rate has been chosen paying attention to the feed pumps operation range but also to the conditions of turbulent flow regime required.

Authors as **?** fixed the minimum operation range of the molten salt receiver in 10% of the nominal mass flow rate. Whereas, Falcone (1986) planned the control system of Solar 100 to maintain the mass flow rate of each circuit at a minimum of 20% of the nominal case under low power conditions. The feed pump system of a SPT is usually compounded by one or more long-shafted pumps working in parallel. In the case of Solar Two, the circulation pump is a single vertical pump of 14 m of shaft length Zavoico (2001). In the planned plant Solar 100, the design counts three half-capacity receiver feed pumps, each of them has a 50% capacity of the nominal flow, keeping one pump in reserve. In this research it has been considered different pump systems configurations with variable minimum allowable mass flow rate.

The dependence of the heat transfer coefficient on the velocity and therefore on the mass flow rate must be taken into account since forced convective heat transfer is influenced by the flow regime Pugh & Garvey (1993). The flow regime depends on the DNI and the flux density on the receiver. To obtain a homogeneous bulk temperature in the tubes of a solar receiver the flow must be under turbulent regime.

The Nusselt number (Nu) for laminar flow is very low ($Nu_l = 4.36$), and hence a laminar flow causes failure in the receiver by corrosion and thermal stress due to the lack of cooling of the tube walls. The accurate prediction of Nusselt number in the transition flow region is difficult, Cheesewright *et al.* (2001) recommended a linear interpolation of the values of Nusselt number for

laminar and turbulent (Nu_t) flow over a transition region (see Equations 6.1 and 6.2). The worst scenario for the Reynolds number are the inlet of the cold salt, if in the first panel has high solar flux, the molten salt under the transition region could damage the receiver by tube overheating. On the other hand, if this panel has low solar flux the salt could freeze inside the tubes. To avoid damages in the receiver it has been imposed the turbulent region as the lower operational limit, Re >4000. The turbulent Nusselt number can be calculated by the correlation of Petukhov (1970), (see Equations 6.3 and 6.4).

$$Nu = \epsilon Nu_l + (1 - \epsilon)\, Nu_t \tag{6.1}$$

$$\epsilon = 1.33 \frac{Re}{6000} \tag{6.2}$$

$$Nu_t = \frac{f/2RePr}{1.07 + 12.7\sqrt{f/2}\left(Pr^{2/3} - 1\right)} \tag{6.3}$$

$$f = \frac{1}{4\left(1.82\log[10]Re - 1.64\right)^2} \tag{6.4}$$

Note that the limit of the pure turbulent limit found in the bibliography for other authors is at Reynold 10,000 Aicher & Martin (1997). It makes that when the receiver start-up at first hours in the morning could operates in mixed turbulent flow, it is not the most favourable operation condition for the receiver but the convective coefficient at that velocity is enough to avoid overheating in the tubes. It has been taken into account that the convective coefficient varies a 10% with respect the pure turbulent regime, although it is compensate between down-flow and up-flow panels.

Using the geometry defined in Rodríguez-Sánchez & Santana (2014*a*) it is possible to calculate the thermal and mechanical behavior of the receiver using a 2D thermal model previously depicted. This receiver model is a 2D simplified thermal model of the receiver that considers temperature variations in both axial and circumferential directions.

Known the solar flux density, obtained with the heliostat model of Sánchez-González & Santana (2015), the heat flux absorbed by the tubes have been calculated by means of the Net Radiation Method Modest (2003), the cross-string method view-factors, and the Siebers and Kraabel correlation for the

external convective losses Siebers & Kraabel (1984). Fixed the outlet temperature of the salt and applying an energy balance to the tubes in which the Petukhov correlation for internal convection Petukhov (1970) it is used, it is possible to determine the mass flow rate in the receiver, the bulk temperature of the salt, and the tube surface temperature.

Then, for the optimal design the velocity limit for turbulent regime (Re = 4000) in the receiver tubes is v_{min} = 0.19 m/s (see Equation 6.5). It has been assumed that the salt flow is regulated by control valves to maintain 565 °C as outlet temperature in both flow paths, and then the mass flow rate of each path is only a function of the total solar flux received. That supposes a minimum allowable mass flow rate ($\dot{m}_{min}$) of 13.77 kg/s when only one flow path is implemented or 27.37 kg/s when the receiver is formed by two flow paths (see Equation 6.6). Therefore, if the pump system limit is lower than 5% or 10% of the nominal mass flow rate, for one and two flow path configurations respectively, the turbulent regime is the most restrictive criteria.

$$v_{min} = \frac{Re_{min}\mu}{\rho dt_{int}} \tag{6.5}$$

$$m_{min} = v_{min}\rho\frac{\pi}{4}dt_{int}^2 N_{tubes}N_{fp} \tag{6.6}$$

In Equations 6.5 to 6.6 μ corresponds to the dynamic viscosity of the salt at the inlet temperatures of the salt (0.0035 Pa/s), ρ represents the density of the salt at 290 °C (1905.7 kg/m^3), N_{tubes} represents the number of tubes per panel, and N_{fp} is the number of flow paths in the receiver.

Note that the limit for turbulent regime calculated is valid for any tube diameter configuration if the number of receiver panels is constant. When the diameter of tubes decreases, the number of tubes per panel increases, and the Reynolds number remains almost constant. For example, using tube diameters of 2.5 cm the Reynolds number increases only 2%, nevertheless the pressure drop increases 67.5%. Therefore, to reduce the tube diameter does not assure turbulent regime during the start-up and shut-down. However, modifying the number of panels of the receiver the Reynolds number varies as the ratio of number of tubes per panel and the pressure drop increment is the Reynold ratio raised to the second power. Increasing the number of panels to 20 the Reynold number increases 12.5% and the problems in the start-up and shut-down disappear, although other properties of the receiver get worse Rodríguez-Sánchez & Santana (2014*a*).

The minimum incident power on the receiver to start to operate can be calculated using Equation 6.7, where the power absorbed by the salt is calculated using the specific heat of the salt at the inlet of the receiver (Cp_{in} = 1493 J/kgK), $\sum C$ corresponds to the sum of the solar flux intercepted by the receiver surface. S is the surface area of each cell in the receiver defined in the optical model, and η_{rec} represents the receiver efficiency, which is calculated with the receiver thermal model that strongly depends on the incident power flux on the receiver and its distribution, the ambient temperature, and the flow pattern.

$$\dot{Q}_{rec} = \frac{\dot{Q}_{salt}}{\eta_{rec}} = \sum CDNISN_{tubes} \tag{6.7}$$

6.4.2 Maximum film temperature and thermal stress

Salt at temperature above the stability limit is in contact with common materials such as stainless steels and nickel alloys, there is an extensive corrosion with the release of nitrogen oxides due to the reaction between the solar salt and chromium to form chromates Nissen & Meeker (1983).In addition, up to 620 °C there is a thermal decomposition of the solar salt that increases the tube corrosion Abe *et al.* (1984). The maximum allowable film temperature is defined as the parameter that drastically increases the corrosion rate. Slusser *et al.* (1985) performed corrosion tests of several metals in molten nitrate-nitrite salts for a range of temperatures between 570 °C and 705 °C. In their tests nickel based alloys, such incoloy 800H, were resistant to corrosion up to 650 °C.

In addition, the admissible thermal stress in the tubes of the receiver is delimited by ASME nuclear code: ASME Boiler and Pressure Vessel Code, Section III, Division 1-subsection NH: Rules for construction of nuclear facility components (American Society of Mechanical Engineers ASME (2011), which is more conservative and specific for the stress and fatigue calculations than those used for boilers. The maximum thermal stress allowed by this code is one third of the ultimate tensile strength.

6.5 Receiver flow path selection

In this section the optimal receiver flow pattern configuration for the nominal conditions of the design point has been obtained based on thermos-mechanical

and hydrodynamic limitations. The cases studied are the eight flow path configurations proposed by Wagner (2008) shown in Figure 6.1.

Figure 6.3 shows the thermal efficiency of the receiver, the total pressure drop, the maximum film temperature and the maximum thermal stress of each one of the eight proposed configurations for the solar noon of the spring equinox. For all the cases the same aiming strategy has been employed: one aiming point to the centre of the receiver with an opening radius corresponding to a normal of standard deviation 2.5, see Sánchez-González & Santana (2015). It can be seen that the maximum thermal efficiency is obtained for configurations 2 and 4, two paths with south to north flow, as Wagner predicted. However, the receiver efficiency is 77.2% instead of Wagnerś 95%. This difference is caused by taking in consideration circumferential variations of the tube wall temperature Rodríguez-Sánchez & Santana (2014*b*).

For configurations 2 and 4 the tube film temperature and the thermal stresses are over the allowable value, producing corrosion and fatigue in the tubes, therefore it is not secure to use them. As Wagner claimed, configurations 5 to 8 (one flow path configurations), are discarded due to the elevated pressure drop that produces a high power consumption of the feed pumps. This increment of the parasitic consumption of the SPT has to be analysed in detail for configurations 5 and 6, which reach safe values of film temperature and thermal stresses. Configurations 1 and 3 (with two flow paths north-to-south configurations), fulfil film temperature, thermal stress and pressure drop restrictions necessary to assure the receiver lifetime. However, these configurations have the worst receiver efficiency, even though it is only around 1% lower than configurations 2 and 4.

Therefore, it can be seen that the worse configurations -regarding film temperature and thermal efficiency- are those in which the outlet is at the northern panels. From the four configurations with the outlet at the southern face, the most favourable are those with two flow paths. Such configurations mean 0.5% less efficiency than one path, but this reduction is lower than the reduction in the SPT global efficiency caused by an increment of 5 bars in the pressure drop. Consequently, configurations 1 and 3 have the most adequate flow pattern to be used for the proposed operational conditions.

At solar-noon the behaviour of configuration 1 and 3 are identical, however at hours with non-symmetric solar flux the behaviour of these configurations is different. It has been studied which of them is the most appropriate configuration for the whole annual range of the receiver operation. In addition,

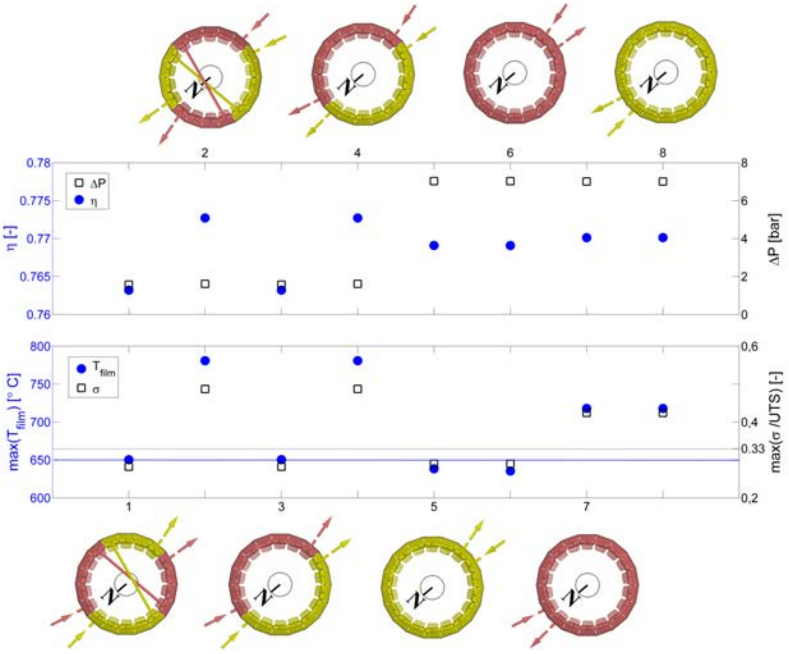

Figure 6.3: Receiver thermal efficiency, pressure drop, maximum film temperature and maximum thermal stress of the eight proposed flow path configurations.

for configuration 1 the position in the crossover has been modified in order to increase the annual availability of the receiver.

6.6 Results

Once the optimal configuration is chosen, the possible hours of operation of a receiver with two flow paths north-to south during a whole year have been determined. There are certain hours in which the correct operation of the receiver cannot be assured, these hours have been identified and carefully analysed.

The simplest flow pattern is the absence of crossovers between the receiver flow paths. However, far from the solar-noon the solar flux intercepted is asymmetric between both flow paths. For the critical hours of operation, it has been analysed if the asymmetric solar flux between flow paths causes damages in the receiver, and if crossover between flow paths must be implemented. Or on the contrary if the solar flux asymmetry could be supported, and it is preferable not

to cross the flow. In addition, modifications in the crossover position have been tested in order to increase the availability and annual efficiency of the receiver. For all the analysed cases, it has been assumed that only flow limitation that must be taken into account is the turbulent flow regime, $Re \geq 4000$.

6.6.1 Possible hours of operation along a year

The hours of the year, in which the solar radiation is not enough to start-up the receiver, although the sun is above the horizon, have been determined using the DNI, the ambient temperature, and the solar flux concentration ratio. The flux density has been calculated using the solar field model proposed by Sánchez-González & Santana (2015). It must be taken into account that the DNI, at a given instant of time, represents the typical value of a representative day of a month, but it can vary along the month, or include haze and cloudy days in which the receiver cannot work (see Figure 6.4(a)).

Using the receiver modelling of Rodríguez-Sánchez & Santana (2014*a*)without the implementation of crossovers, the thermal efficiency of the receiver and the power absorbed by the salt have been calculated. At first hours of operation the receiver has efficiencies near to 50%, but it grows quickly and when, the radiation is close to the nominal value, the efficiency of the receiver reaches 77%, as can be observed in Figure 6.4(b).

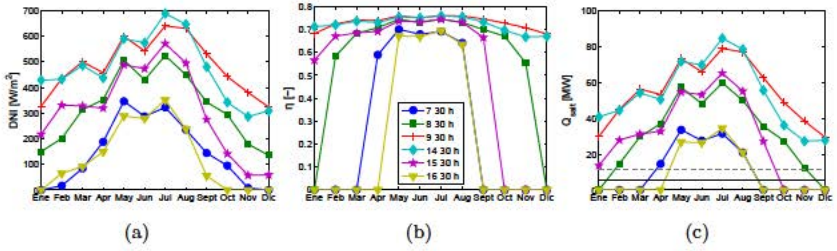

Figure 6.4: a) Average hourly statistics direct normal solar radiation. b) Average thermal efficiency of the receiver. c) Average heat absorbed by the salt. All data corresponds to Seville (Spain) for a representative year.

Figure 6.4(c) represents the total power absorbed by the salt at each hour. The horizontal solid black line delimits the turbulent flow regime ($Q_{salt} = 19.98$ MW). When the power is under that value the flow is under transient regime. At these hours the receiver integrity could be compromised, and therefore it

has been assumed that the receiver is not working. In addition, the grey dotted line shows the limit of operation of a SPT when the pump system is unable to operate at mass flow rate lower than 20% of the nominal flow, as happen in Solar 100 Falcone (1986). In this case, the hours of operation of the receiver decrease 660 h per year respect to the turbulent regime limit. Then, a proper design of the pump system is a key to keep at maximum the availability of SPT. In Figure 6.4(c) it can be also observed that due to the difference in the flux density between summer and winter, in winter months the minimum DNI to start to operate the receiver is 170 $\mathrm{W/m^2}$, while in summer is enough a solar direct irradiance of 100 $\mathrm{W/m^2}$.

Figure 6.5 depicts the average hours of sun of each month, the hours in which the radiation flux is enough to heat the salt, and the hours at which the receiver can operate at turbulent regime. It can be observed that the receiver starts-up at least one hour after the sunrise ($\sim 15°$ of solar elevation), time enough to preheat the tube walls; while the shut-down are at least one hour before sunset, reducing the stress cycles of cooling. In addition, depending on the season the start-up varies from 7:00 h to 9:00 h and the shut-down from 15:00 h to 17:00 h, all respect to solar time, modifying the panel which receives the peak flux in the start-up and shut-down along the year.

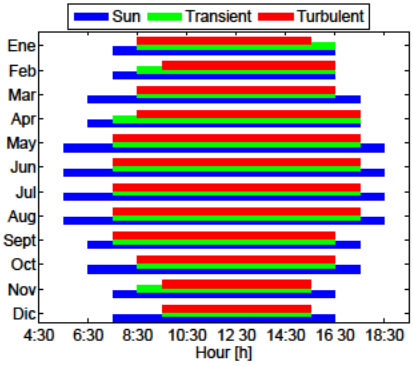

Figure 6.5: Average hours of sun per month and hours of possible operation of the receiver.

6.6.2 Critical hours of operation

The optimal flow pattern configuration must fulfil the operational limits of the receiver for the whole operational range. In addition, it has to maximise the

annual availability and efficiency of the SPT.

Therefore, it is necessary to analyse the first hours in the morning and the last hours in the afternoon, in which problems associated with salt velocity can appear. During the sunrise and sunset the receiver operation restrictions are the limits of the feed pumps and the turbulent regime. In addition, the periods of high peak flux with not symmetric distribution with respect to the north-south axis must be studied to avoid excessive film temperature and thermal stresses. In case of big feed pump systems the start-up and shut-down analysis is not crucial, because there is enough flux concentration. Nevertheless, the hours with high solar irradiation but non-symmetrically distributed continue being critical.

Figure 6.6 shows the solar flux distribution on the receiver for the design point and for three examples of critical hours: first hour in the morning, last hour in the afternoon, and high peak flux non-symmetrically distributed between paths. Where x axis corresponds to the circumferential perimeter of the receiver counter-clockwise from the south, as can be seen in the panel numeration, and y axis represents the receiver height.

In spring equinox at solar-noon the solar flux is totally symmetric with respect both flow paths (see first line Figure 6.6). Coming back to Figure 6.4(c) the most limiting hours analysed for turbulent flow 7:00 h and 17:00 h of August, Figure 6.6 lines 2 and 3 respectively. Both hours are mirrored images with respect to the solar-noon. Then, they receive the same total solar flux, but it is distributed symmetrically with respect to the north-south axis. Consequently, the results of the east side for 7:00 h are equivalent to the results of the west side for 17:00 h and vice versa. As first hours in the morning and last hours in the afternoon are symmetrical, only one hour has been studied in detail choosing 7:00 h as reference. Furthermore, it can be seen that they have very low flux concentration compared to the design point. Finally, the last line of Figure 6.6 depicts May at 9:00 h. It is a clear example of high peak flux non-symmetrically distributed between paths. At this hour the peak flux is more centred to north than the case of august at 7:00/17:00 h, but less than the spring equinox at 12:00 h.

In Figure 6.6 the maximum solar flux ranges go from 0.24 MW/m^2 at first/last hours of August, to 0.65 MW/m^2 at 9:00 h of May, and to 0.8 MW/m^2 at the solar noon of the spring equinox.

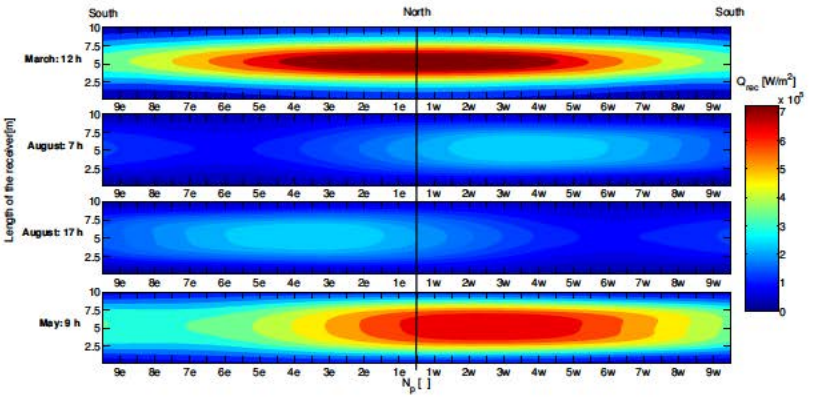

Figure 6.6: Radiation map distribution on the receiver. From top to bottom: Design point (spring equinox at 12:00 h); Start-up (7:00 h of August); Shut-down (17:00 h August); and Non-symmetric high peak flux (9:00 h of May).

6.6.3 Optimal crossover position

The asymmetric solar flux between flow paths can reduce the receiver operational hours when the solar flux is non-homogeneously distributed between paths and the solar flux is low. Under these conditions, the convective heat transfer coefficient in one of the paths might not able to refrigerate the tube wall. Implementing crossovers the energy absorbed by both paths could be equalised. However, reaching the same quantity of flux could be undesirable if the solar flux distribution with the crossovers has the peak at the outlet of the receiver. High solar flux in panels in which the salt is too hot could increase the tube wall temperature and the thermal stresses. Then, the film temperature of the path could overpass the limit established by the receiver material accelerating the corrosion process and diminishing the lifetime of the receiver.

In this section has been chosen which of the two selected flow patterns it is the most adequate configuration for a whole year operation range. The behaviour of receivers have been analysed for the critical hours of operation. Remember that the selected receivers are composed by two flow paths north-to-south with none (configuration 3 of Figure 6.3) or one crossover in the middle of the panel (configuration 1 of Figure 6.3). In the case of configuration 1 different crossover positions have been implemented in order to find the most adequate flow configuration.

The selection of the best receiver flow path configuration has been done

following the procedure showed in Figure 6.7. It starts with a known heliostat field, receiver geometry, and location. Firstly, different path crossover configurations for start-up and shut-down are analysed in order to find the optimal configuration that increase the receiver availability. After that, it is proved if the optimal path configuration for start-up and shut-down is valid for those hours of high peak flux but non-symmetric flux distribution between paths.

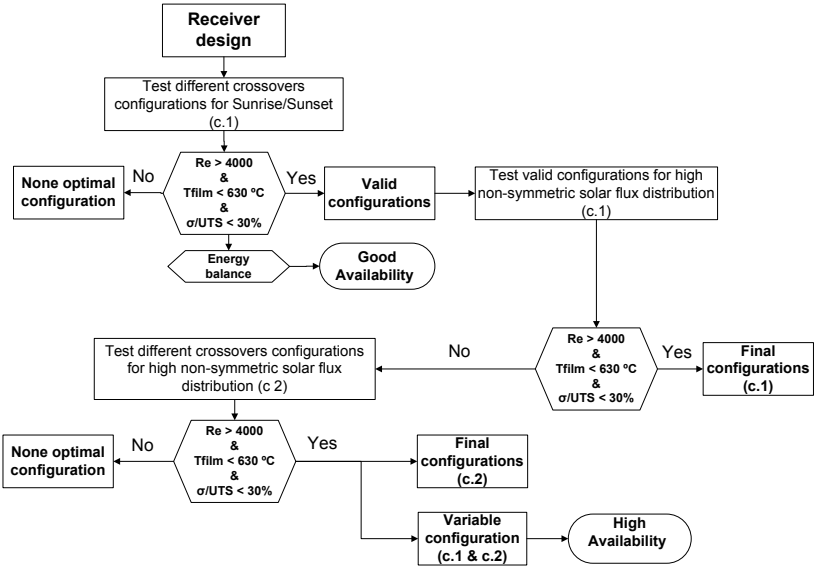

Figure 6.7: Scheme procedure to optimize the flow pattern configuration of a solar external receiver.

Start-up and shut down (August at 7:00 h)

Figure 6.8 shows the variation of the solar radiation distribution over the two flow paths of the receiver when one crossover is applied at 7:00 solar hour of August (configuration 1). Vertical axis represents the height of the receiver, and horizontal axis the panel number of each flow path, from 1 to 9 east and west. There are 8 possible combinations of crossovers, but for clarity only have been plotted the configurations with crosses at the even panels of each path. In addition, the flow pattern without crosses (configuration 3) has been represented to observe the differences. It can be seen that in absence of crossovers the maximum heat flux is not in the western panels, else it is slightly displaced to

the north.

When there is a cross in the receiver the flow path goes from north to south changing the side from west to east and vice versa; it means that if the radiation map it is not symmetric, as happens at 7:00 solar time, the incident flux could have step variations. For example, for a crossover in the fourth panel the west flow path starts in the first panel sited in the north of the receiver, it continues by the west panels until the west fourth panel, and in the fifth panel the flow path is crossed and the radiation flux of the fifth panel corresponds to the east fifth panel instead of the west fifth panel.

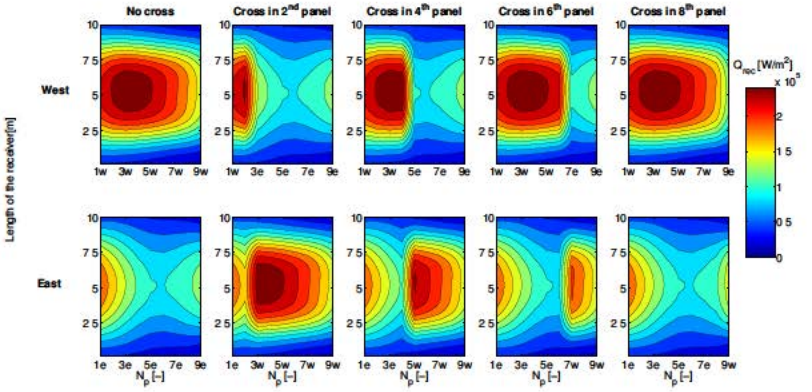

Figure 6.8: Radiation map distribution on the receiver at 7:00 h of August with none or one crossover between flow paths.

In the ideal configuration both flow paths must absorb the same energy, and the maximum solar radiation has to be in the first panels of the receiver, what reduces the thermal stresses and the tube wall temperature. The total solar flux received by both flow paths is equal when the cross is implemented in the 4^{th} panel (see Figure 6.9). However, this configuration is not the most adequate because the maximum solar radiation is close to the western and eastern panels, affecting to the film temperature (see Figure 6.6). To obtain the ideal configuration is not possible using only one crossover in the receiver, but varying the crossover position the receiver behaviour can be improved.

Figure 6.10 represents mechanic, thermal and hydrodynamic variables when one crossover is applied to the receiver flow paths. The position 0 corresponds to the nominal case in which none crossovers in the receiver is installed, the followings data from 1 to 8 correspond to the variation of the crossover position,

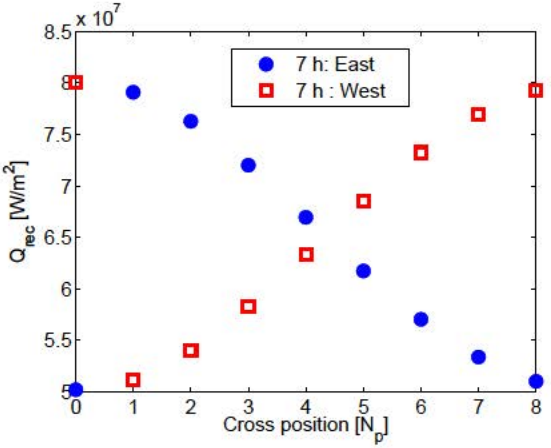

Figure 6.9: Solar flux received by each flow path, for one crossover in different positions at 7:00 h of August.

from the outlet of the first panel to the outlet of the 8 panel of each path. For the different crossover positions the efficiency of the receiver is almost constant and equal to 64.2%, because the receiver is not working in its nominal conditions.

Figure 6.10(a) portrays the minimum salt velocity in the tubes; it takes place at the inlet of the receiver, when the salt is cold and the density reaches the highest value. It is possible to observe that without crossovers the salt velocity in the east side is lower than the turbulent regime limit. Similar results are obtained crossing in the first or last panel of the path (asymmetric solar flux between paths). An allowable salt velocity can be achieved crossing in any positions from the 2^{nd} panel to the 7^{th} panel. However, apply the cross at the ending of the 4^{th} or 5^{th} panel are the best configurations.

The total pressure drop, showed in Figure 6.10(b), is lower than the pressure drop limit imposed by the power consumption of the pump system. Hence, pressure drop does not present any problem during the receiver start-up. It can be seen that velocity and pressure drop only depend on the total flux that reach each path but not on the solar flux distribution. However, thermal stresses and film temperature depend on both variables.

The maximum film temperature of the receiver increases drastically with the position of the flow path crossover (see Figure 6.10(c)). However, it never overpasses the allowable limit of the alloy 800H. To cross in the last panels is not adequate due to the peak solar flux is displaced to the last panels of the

paths. Therefore, during the start-up of the receiver it is not recommendable to cross the flow paths after the middle of the path. In this specific day the best option to minimise the film temperature is to cross in the 3^{rd} panel. The thermal stress is also below the allowable limit (see Figure 6.10(d)); it reaches the minimum value crossing in the 3^{rd} or 4^{th} panel.

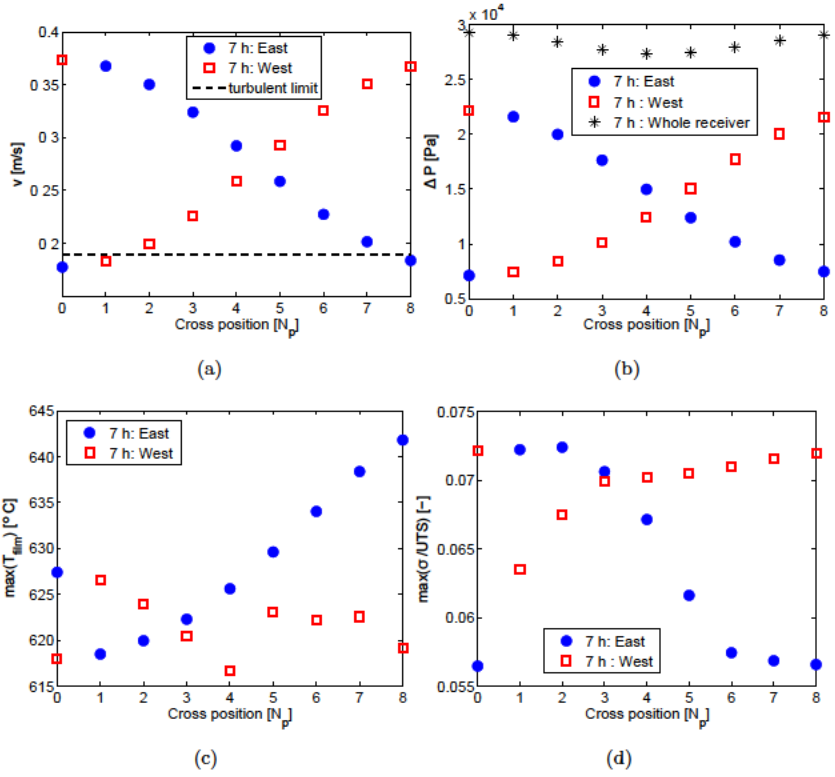

Figure 6.10: Implementation of one crossover in the receiver for 7:00 solar hour of August. a) Minimum salt velocity. b) Total pressure. c) Maximum film temperature. d) Maximum thermal stress.

Therefore, when the solar flux is low and not-symmetric between paths it is necessary to cross the flow path to equalise the flux between paths and increase the receiver availability. The maximum value of the solar flux is displaced several degrees to the north respect to the west side of the receiver, then it is necessary to cross before the middle of the path. The problem of cross in the

first panels is that the flux that reaches to each path is not similar. In the light of the results, the best option seems to cross in the 4^{th} panel, which means equal heat flux in both paths and low film temperatures.

To complete the analysis, a configuration with two crossovers between paths has been implemented. High number of crossovers between the receiver flow paths homogenise the solar flux distribution between flow paths. However, it makes more complex the receiver operation, especially by the heat losses and pressure drop in the pipe that change the flow direction. In addition, the solar flux distribution continues being high in the last panels and the improvement obtained with respect one crossover are negligible. Then, one crossover is the preferable design in the sunrise and sunset, and implement higher number of crosses between paths has been rejected.

High peak flux non-symmetrically distributed (March at 9:00 h)

In this section, it has to be taken into account hours in which solar flux is high and not totally symmetric whit respect to north-south axis. In these moments the thermal stresses and the film temperature could cause damages in the receiver. To avoid efficiency reduction it has been tested if in hours in which the film temperature is close to the limit a modification of the heat flux distribution, by means of crossovers between paths, can reduce the temperature to allow the receiver to operate with high peak flux. It is the case of May at 9 h. In that moment the solar irradiation and the flux density are elevated, but the flux distribution is not symmetric between both flow paths (see Figure 6.6).

In this date the radiation map distribution is still non-symmetric with respect to the north-south axis. In this case the receiver is operating close to the nominal point, and the receiver efficiency is 75.9%. Figure 6.11 shows that at 9:00 h of May the total solar flux is equal for both paths crossing in the 5^{th} panel. However, it is not possible to cross the flow paths after the 2^{nd} panel without increasing out of limits the film temperature and the thermal stresses on the receiver. Then, the solar flux in both flow paths must be different to avoid causing damages in the receiver.

Then, as the day passes the position of the optimal crossover approach the inlet of the flow path, and closer to the first panel the crossover has to be implemented. It made that the optimal crossover configuration for the start-up and shut-down is harmful for the receiver when it received high peak flux non-symmetric distributed between paths. Then, in moments as 9:00 h of May, it is more important to get a well distributed solar flux than to have the same solar

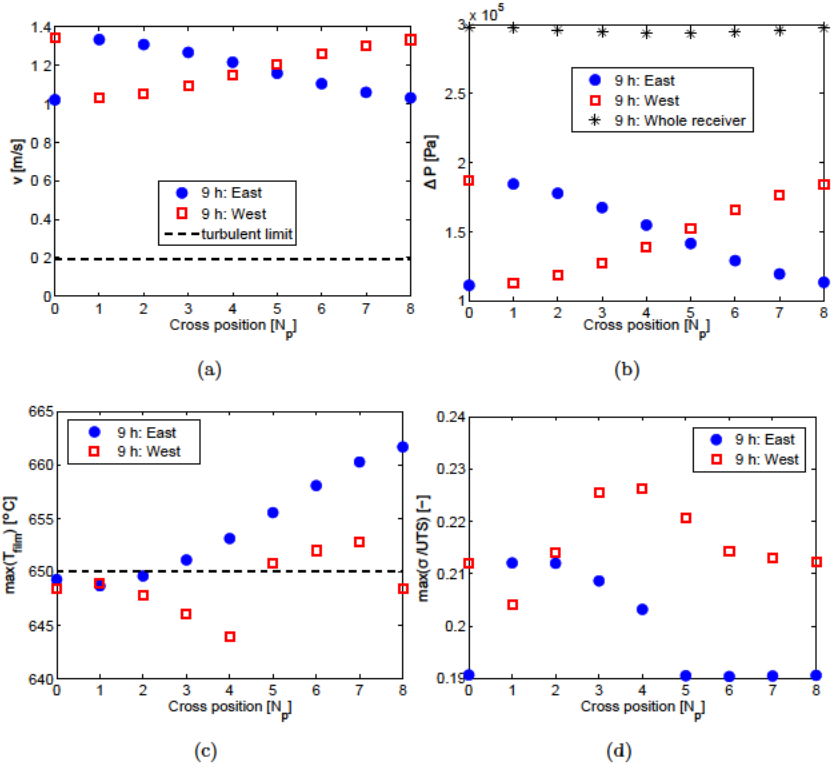

Figure 6.11: Implementation of one crossover in the receiver for May at 9:00 h solar time. a) Minimum salt velocity. b) Total pressure. c) Maximum film temperature. d) Maximum thermal stress.

flux in both paths.

Therefore, the most adequate flow pattern is to employ a variable receiver crossover configuration. Implementing a crossover just before of the middle of the panel (in this case 4^{th} panel) at first hours of the morning and last hours of the afternoon to increase the availability of the receiver. And remove the crossover when the receiver operates close to nominal conditions. If a variable configuration is not possible, it is recommendable not to implement any crossover in the receiver to assure the correct operation during hours of high efficiency, at the expenses of reducing the receiver availability. In nominal conditions the power obtained is higher than in the start-up and shut-down.

6.7 Conclusions

In this study different flow pattern configurations on molten-salt central receivers have been studied in order to assure the secure conditions of operation of the receiver in its whole range of work. Thermal, mechanical and hydrodynamic behaviour of the receiver at the design point have been analysed. It has been obtained that the best flow path configurations are those in which the flow exits by the south side of the receiver: it reduces the maximum film temperature and assures that the maximum solar flux is in the cooler side of the path, achieving a reduction of the thermal stress in the tubes. In addition, it is more desirable a configuration formed by two parallel flow paths to reduce the pressure drop for a given load. Then, the cold HTF must enter into the receiver at the panels that are exposed to higher solar flux and exits at the panels with lower solar radiation (from north to south in the northern hemisphere). The optimal flow path configuration can have none or one crossover between paths.

At the design point, receiver flow configurations with or without crossover have an identical behaviour. The critical hours of operation have been identified: the first hours in the morning, the last hours in the afternoon when the solar radiation is low and non-symmetric with respect north-south axis, and hours in which the peak flux is high but the radiation is not-symmetrically distributed between paths. The most important restriction to assure the correct operation of the receiver are the film temperature, the thermal stress, the pressure drop, the pump system and the convective heat transfer coefficient.

In order to absorb the same flux in both flow paths when the heat flux is not symmetric with respect to north-south axis, one crossover has been implemented in the receiver. The salt velocity and the pressure drop of both paths equalise when the solar flux in both paths is the same. However, the film temperature and thermal stresses depend on the solar flux received and its distribution. As sun moves to the midday the allowable positions of the crossover approach the inlet of the flow path, and it must be as close as possible to the first panel, although the solar flux sum is not always the same in both paths.

Although in this study the receiver geometry is fixed, it has been tested that the tube diameter does not modify the Reynolds number. Nevertheless, increasing the number of panels in the receiver also increases the Reynolds number, and the problems of transient regime in the sunrise and sunset disappear. However the pressure drop is strongly augmented.

To improve the heat flux distribution, receiving similar solar flux in both flow paths, during the start-up and shut-down of the receiver the best option is to

implement one crossover in the 4^{th} panel of each flow path for a Gemasolar like receiver and heliostat field, in this way the mass flow per path is becomes equal, and there is no problems of transient regime flow. However, this configuration is not valid as the morning progresses. For these cases are recommended not to cross the flow paths. Consequently, the best receiver design will be that in which the flow path configuration can vary along the day; implementing one crossover before the middle of the path during the sunrise and sunset, and removing the crossover when the solar irradiation is elevated. If this variation is not possible the most appropriate configuration is not to cross the flow paths. Since, it is more important a safe operation in the hours of maximum peak flux than during the starts-up and shuts-down.

Finally, in order to distribute more homogeneously the solar flux on the receiver and obtain a better behaviour of the receiver two crossovers have been implemented. The results are similar to the previous case and the improvement is not compensated by the complexity added to the receiver design. It has been recommended not making more than one crossover in the receiver.

Nomenclature

C	Flux density rate on the receiver [-]
Cp	Specific heat [J/kg° C]
DNI	Direct normal irradiance [W/m^2]
dt	Tube diameter [m]
f	Petukhov coefficient [-]
$\dot{m}$	Mass flow rate [kg/s]
N	Number of elements [-]
Nu	Nusselt number [-]
Pr	Prandtl number [-]
$\dot{Q}$	Heat power [W]
Re	Reynolds number [-]
S	Surface area [m^2]
T	Temperature [° C]
UTS	Ultimate tensile strength [Pa]
v	Molten salt velocity [m/s]

Greek letters

ΔP	Pressure drop [Pa]
ϵ	Nusselt coefficient for transition regime [-]
η	Receiver thermal efficiency [%]
μ	Dynamic viscosity [Pa/s]
ρ	Molten salt density [kg/m^3]
σ	Thermal stress [Pa]

Subscripts

amb	Ambient
fp	Flow path
in	Inlet
int	Internal
l	Laminar
min	Minimum
p	Panel
rec	Receiver
t	Turbulent
we	External wall

Abbreviattions

HTF	Heat transfer fluid
SPT	Solar power tower

References

Abe, Osami, Utsunomiya, Taizo & Hoshino, Yoshio 1984 The thermal stability of binary alkali metal nitrates. *Thermochimica Acta* 78 (1-3), 251–260.

Aicher, T. & Martin, H. 1997 New correlations for mixed turbulent natural and forced convection heat transfer in vertical tubes. *International Journal of Heat and Mass Transfer* 40 (15), 3617–3626.

ASME 2011 ASME Boiler and Pressure Vessel Code, Section II - Materials. *Tech. Rep.*. American Society of Mechanical Engineers, New York.

Augsburger, Germain & Favrat, Daniel 2013 Modelling of the receiver transient flux distribution due to cloud passages on a solar tower thermal power plant. *Solar Energy* 87, 42–52.

Cheesewright, R., Heggs, P.J., Martin, B.W., Parry, W.J. & Ralston, T. 2001 Forced convection heat transfer in straight tubes. Part 2: laminar and transitional flow. *Tech. Rep.* 93018. ESDU: Chemical Engineers and Mechanical Engineers, London.

Collado, F.J.; Gómez, A. & Turégano, J.A. 1986 An analytic function for the flux density due to sunlight reflected from a heliostat. *Solar Energy* 37, 215–34.

Collado, F.J. 2009 Preliminary design of surrounding heliostat fields. *Renewable Energy* 34 (5), 1359–1363.

Collado, F.J. & Guallar, J. 2013 A review of optimized design layouts for solar power tower plants with campo code. *Renewable and Sustainable Energy Reviews* 20, 142–154.

Dhyia Aidroos, B.; Hasimah Abdul, R.; Wan Zaidi Wan O; & Saeed Obaid, F. 2015 Historical development of concentrating solar power technologies to generate clean electricity efficiently - A review. *Renewable and Sustainable Energy Reviews* 41, 996–1027.

Falcone, P.K 1986 *A handbook for solar central receiver design*. Livermore, California: Sandia National Laboratories.

Golden, C. 2015 System advisor model (sam). sam.nrel.gov/content/downloads.

Kistler, B.L. 1986 A User's Manual for DELSOL3: A Computer Code for Calculating the Optical Performance and Optimal System Design for Solar Thermal Central Receiver Plants. *Tech. Rep.*. Sandia National Laboratories, Albuquerque.

Kolb, G.J.; Ho, C.K.; Mancini T.R. & Gary, J.A. 2011 Power Tower Technology Roadmap and Cost Reduction Plan. *Tech. Rep.* April. Sandia National Laboratories, Sandia National Laboratories, Albuquerque.

Lata, Jesús M., Rodríguez, Manuel & Álvarez de Lara, Mónica 2008 High Flux Central Receivers of Molten Salts for the New Generation of Com-

mercial Stand-Alone Solar Power Plants. *Journal of Solar Energy Engineering* 130 (2), 1–5.

Modest, F Michael 2003 Radiative Heat Transfer. In *Radiative Heat Transfer*, Second edi edn. (ed. Elsevier Science), chap. 5. RADIATI, pp. 162–197. New York, San Francisco, London.

Nissen, D. a. & Meeker, D. E. 1983 Nitrate/Nitrite Chemistry in NaN03-KN03 Melts. *Inorg. Chem.* 22 (June 1980), 716–721.

Pacheco, J.E., Ralph, M.E. & Chavez, J.M. 1995 Investigation of Cold Filling Receiver Panels and Piping in Molten-Nitrate-Salt Central-Receiver Solar Power Plants. *Journal of Solar Energy Engineering* 117 (NOVEMBER), 282.

Petukhov, B.S. 1970 *Heat Transfer and Friction in Turbulent Pipe Flow with Variable Physical Properties*, , vol. 6. Moscow (USSR).

Pugh, S. J & Garvey, S. J 1993 Forced convection heat transfer in straight tubes. *Tech. Rep.* August. ESDU 92003, London, ESDU 92003.

Rodríguez-Sánchez, M.R.; Soria-Verdugo, A.; Almendros-Ibáñez J.A; Acosta-Iborra A. & Santana, D. 2014*a* Thermal design guidelines of solar power towers. *Applied Thermal Engineering* 63 (1), 428–438.

Rodríguez-Sánchez, M.R.; Marugán-Cruz, C.; Acosta-Iborra A. & Santana, D. 2014*b* Comparison of simplified heat transfer models and CFD simulations for molten salt external receiver. *Applied Thermal Engineering* 73, 991–1003.

Sánchez-González, A. & Santana, D. 2015 Solar flux distribution on central receivers: A projection method from analytic function. *Renewable Energy* 74, 576–587.

Siebers, D L & Kraabel, J S 1984 Estimating Convective Energy Losses From Solar Central Receivers. *Tech. Rep.*. Sandia, Livermore.

Slusser, J. W., Titcomb, J. B., Heffelfinger, M. T. & Dunbobbin, B. R. 1985 Corrosion in Molten Nitrate-Nitrite Salts. *Journal of Metals* 37 (7), 24–27.

Vant-Hull, Lorin L. 2002 The Role of Allowable Flux Density in the Design and Operation of Molten-Salt Solar Central Receivers. *Journal of Solar Energy Engineering* 124 (May), 165.

Wagner, M. J. 2008 Simulation and Predictive Performance Modeling of Utility-Scale Central Receiver System Power Plants. PhD thesis, University of Wisconsin, Madison.

Winter, C J, Sizmann, R L & Vant-Hull, L L 1991 *Solar Power Plants*. Berlin, Heidelberg: Springer Berlin Heidelberg.

Zavoico, A.B. 2001 Solar Power Tower: Design Basis Document. *Tech. Rep.* July. Sandia National Laboratory, San Francisco, SAND2001-2100.

CHAPTER
SEVEN

Possible next generation of molten salt solar power tower

Contents

Scientific Contributions

- M.R. Rodríguez-Sánchez, A. Sánchez-González, C. Marugán-Cruz, D. Santana. Evaluation of subcritical, supercritical and ultra-supercritical solar power tower. Submitted for publication to Solar Energy.

7.1 Abstract

The increment of the solar power towers efficiency is one of the main goals of the industry and the scientist community. The implementation of a new generation of solar power towers with higher heat transfer fluid temperature seems to be one of the best options. It could allow the implantation of supercritical and ultra-supercritical power blocks, more efficient than nowadays subcritical cycles.

It has seen that the increment of the power block efficiency is against the efficiency of the heliostat field and receiver efficiency, which have higher heat losses. In this paper it has been studied the viability of implement molten

salt solar power towers with higher outlet temperature of the salt. In this study three different bulk temperature power towers have been studied: 565 °C (subcritical power-block), 600 °C(supercritical power-block), and 650 °C (ultra-supercritical power-block). For a better comparison the three plants have the same heliostat field, but different receiver. The receiver design is an optimization based on the main thermal, mechanical and hydrodynamic limits of the tube materials, and its efficiency has been studied in combination with the heliostat field efficiency.

It has seen that for nominal conditions the new generation of solar plants have better efficiencies than subcritical plants. However, taking into account that a solar plant is subjected at numerous cycles and different power loads, the global plant efficiency improvement using ultra-supercritical plants is negligible or null with respect to subcritical plants. The relative cost of the three plants have been also analysed and a big reduction of the ultra-supercritical power block cost is necessary to do the new generation of power plants advantageous.

7.2 Introduction

One of the main goals of the latest researches about solar power tower (SPT) is to increase the overall efficiency of the plant. The efficiency optimization could be focus in one of the three main subsystems of the plant: heliostat field, receiver, or power block. The power block is usually formed by a Rankine turbine, and its efficiency could be obtained with confidence measuring the input and output data. However, the solar flux reflected by the heliostats and intercepted by the receiver cannot be measured, they only can be estimated. In the last decades numerous models have been developed in order to obtain a good estimation of the phenomena that happens in both systems. It has been shown that the heliostat field and the receiver behaviours are coupled, and they have to be studied together.

Several studies are focused on modify different aspects of the SPT in order to increase the plant efficiency. For example, Boerema & Rosengarten (2013) studied the possible implementation of new receiver designs, **?** tested new tube materials with different thermal and mechanical properties, Boerema *et al.* (2012) also made test to substitute the solar salt for a ternary salt called Hitec, and McGovern & Smith (2012) studied the effects of increasing the outlet temperature of the heat transfer fluid (HTF) in order to use supercritical power blocks.

Modern steam turbines work at higher pressure and temperature increasing the efficiency of the power block with respect to the traditional subcritical one. This development could be integrated in SPT with central receiver technology (Singer *et al.*, 2014). There are several studies related to CO_2 SPT at high pressure and temperature, but also it is possible to find researches based on this modern power blocks using molten salt as HTF in the receiver.

At the present time, molten salt SPT reach bulk temperatures of 565 °C (Litwin & Park, 2002). One of the most promising conceptual way to increase the plant efficiency is a new generation of SPT that increases the temperature level of the HTF until 650 °C to generate electricity in supercritical and ultra-supercritical Rankine power blocks (Kolb, 2011).

This research is focus on analyze the viability of elevating the work temperature of an external cylindrical receiver that works with molten salts as HTF. It has been calculated the optimum receiver design for each of the three levels of Rankine power block temperature (565 °C, 600 °C, and 650 °C) using for the three cases the same heliostat field. The design point chosen is the spring equinox at 12 solar time. For each temperature level different tube materials have been proposed to be used in order to avoid corrosion and prompt failure of the receiver (Kolb, 2011).

The plant efficiency increment using the evolved power blocks has been detailed studied for nominal and partial power loads; at the same time the relative investment cost of these power plants have been evaluated in order to give an idea of the cost necessary to elevate the global efficiency of the plant using the new generation of SPT.

7.3 Heliostat field and receiver configuration

The receiver and heliostat field efficiencies are connected and they have to be studied together in order to increase as much as possible the global SPT efficiency. In this section has been described the heliostat field-receiver model. It allows controlling the solar flux intercepted by the receiver, calculating the wall and bulk temperatures of the receiver, and obtaining the field and receiver efficiencies.

The reference heliostat field used in this study has been Gemasolar, whose 2650 heliostat coordinates were retrieved from a scaled aerial photograph. Each heliostat is a square 10.95 m side with 0.88 reflectivity and 0.95 cleanliness. Sun, slope and tracking errors are 2.51, 2.6 and 2.1 mrad, respectively.

According to the heliostat field the baseline receiver is sited on a tower 120 m height. It is a molten-salt 360° cylindrical external receiver formed by vertical tubes arranged in panels. It has been assumed that the receiver aspect ratio is 1.25, value inside the range recommended by Lovegrove & Stein (2012). The receiver flow pattern is formed by two flow paths north-to-south without crossover between paths, see Figure 7.1. This configuration was pointed as the best north hemisphere receiver flow pattern by Rodríguez-Sánchez *et al.* (2015).

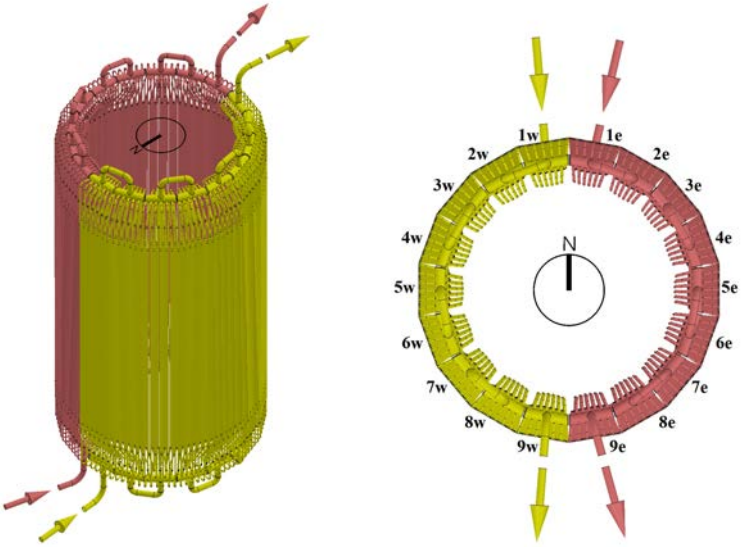

(a) (b)

Figure 7.1: Receiver configuration scheme a) profile view. b) plant view.

In addition, throughout the variation of the aiming strategy, the number of panels, the tube diameter, and the tube thickness it is possible to design the most adequate receiver for each power block level studied: subcritical (565 °C), supercritical (600 °C) and ultra-supercritical (650 °C). Table 7.1 shows the different aiming strategy and receiver configurations analysed in this study.

Olivares (2012) showed that solar salt, in an air atmosphere and at temperature lower than 650 °C is in equilibrium maintaining almost constant its nitrite-nitrate ratio; but 650 °C is the maximum allowable bulk temperature. At higher temperatures the weight loss increases quickly, and up to 747 °C

there is an important bulk decomposition of the salt. Mar & Kramer (1980) claimed that the molten salt decomposition increase from 0.05% at 565 °C to 0.17% at 650 °C. For a plant similar to Gemasolar, which contain close to 8500 tons of molten salts, it means a increment of the salt replacement from 5 to 16 tons, assuming a plant whole service life of 30 years.

The optimal design must maximize the heliostat-receiver efficiency, reach the expected outlet bulk temperature of the salt, and also fulfil the mechanical, thermal and hydrodynamic limits of the receiver materials. The main limits of operation for an external receiver are described below:

- Solar peak flux: to avoid overheat and damage the tube material it must not overpass 1.2 MW/m^2, hence the aiming strategy must be carefully controlled.

- Internal convective transfer coefficient: to assure an appropriate convective heat transfer between the salt and the tube wall the flow regime must be turbulent , Re>4000, (Petukhov, 1970). It homogenises the bulk temperature, and avoids tube overheating.

- Pressure stress: to avoid failure of the tubes it has to be under the limits specified in theASME (2011). Note that the pressure stress is related with the pressure inside the tubes, then it decreases with the tube thickness, see Equation 7.1.

$$th_p \geq \frac{Ps_{max} dt_{ext}}{2S_{max}} \tag{7.1}$$

  Where dt_{ext} is the external tube diameter, S_{max} correspond to the maximum allowable stress of the tube material, and $Ps_{max} = Ps_H + \Delta Ps$ represents the maximum pressure in the receiver and it is calculated as the sum of the hydrostatic pressure and the pressure drop, which has been obtained with the equation proposed by Rodríguez-Sánchez & Santana (2014).

- Thermal stress: it is related with the mechanical properties of the tube materials (ASME, 2011), it must be lower than 33% of the ultimate tensile strength (UTS) of each material. Elevated values cause damages by fatigue and cracking.

- Film temperature: it depends of the tube material. High film temperature produces tube corrosion and changes in the material properties.

- Pressure drop: it must be as minimum as possible to reduce the feed pump consumption and the parasitic power of the SPT. It should not be higher than 20 bars.

Table 7.1: Variation of parameter for the different SPT studied. The combination of these parameters sums a total of 3150 receiver configurations.

Material	**Aiming strategy (k)**	**Number of panels**	**Tube diameter [mm]**	**Tube thickness [mm]**
Inconel 625	3	14	73	1.245
Alloy 800H	2.5	16	60.3	1.651
Haynes 230	2	18	48.3	2.108
	1.5	20	42.2	2.769
	1	22	33.4	3.048
		24	26.7	
			21.3	

Table 7.1 shows the three different materials employed in the different SPT levels. Higher bulk temperature of the salt requires more resistant material to corrosion, that usually is a function of the nickel content. Inconel 625 was selected because is extensively study in the industry and has the best mechanical and thermal properties, but the high temperature vessel code (American Society of Mechanical Engineers (ASME, 2011) does not recommend to use this material at film temperatures higher than 600 °C, then only has been employed in subcritical SPT. Alloy 800H was used in Solar One project and in a Sandia salt receiver tests (Kolb, 2011). Bradshaw (1987) established with several test that the maximum film temperature of alloy 800H in 630 °C, then it is not valid for ultra-supercritical SPT. Haynes 230 is promoted to become in an important candidate material for solar tower receivers, its properties are a little bit worse than the Inconel 625 properties, but it can work at temperatures up to 650 °C thanks to the percentage of tungsten in its composition.McConohy & Kruizenga (2014) test the Haynes 230 at film temperature of 680 °C and they concluded that it could be used at this temperature despite the elevated corrosion rate.

The solar flux density incident on the different receiver configurations has been calculated using the computational optical model developed by Sánchez-González & Santana (2015) based on the analytic function at the image plane (Collado & Turégano, 1986). Sánchez-González & Santana (2015) pointed that

for a fixed day an hour (solar noon of the spring equinox) the field efficiency is a function of the number of panels of the receiver and of the aiming strategy.

The aiming strategy has been modified assuming that the solar flux on the receiver is a 3D Gaussian like. In this way varying the typical deviation (k) from 3 to 1, on half to half point, the variance of this normal distribution is reduced from 99.7% to 84.13%. It reduces the heliostat field efficiency but allows to the receiver fulfil the materials limits. Figure 7.2 show the solar flux intercepted by a receiver of 14 panels for different typical deviation values, in y axis it is possible to see the length of the receiver, and x axis corresponds to the receiver perimeter from south to south. The colour-bar indicates the value of the flux density. It can be seen that for lower values of k the peak flux decreases and the flux becomes more homogeneous.

In Table 7.1 the number of panels is even, it is due it has been assumed two flow paths in the receiver. It makes symmetric heat flux in both paths of the receiver. The tube diameter and thickness also affect to the thermal efficiency of the receiver. Nominal diameters from 7.3 to 2.13 cm, and thickness from 3.048 to 1.245 mm have been tested in order to find the best receiver design.

7.4 Whole receiver thermal model

The behaviour of the different receiver configurations has been calculated with the thermal model proposed by Rodríguez-Sánchez & Santana (2014) whose main characteristic is to take into account the circumferential variations of the tube wall temperature. Furthermore, in the model have been included all the tubes of the receiver and not only one per panel, see the results of a simulation of Solar Two receiver in Figure 7.3), in order to calculate major details in the receiver and determine the most critical tubes of each receiver.

The whole receiver model requires as inlet data a first approximation of the wall temperature of every tube. It has been calculated including in the initial version of the thermal model the incident flux of each tube, but assuming that the adjacent tubes have the same tube wall temperature than the tube under study. However, in the whole receiver model there is not symmetry between one tube and the following, and the view factors matrix is more complex than for the initial model, having a matrix that includes the last half tube of the previous panel, all the tubes divides in half, and the first half tube of the following panel, see Figure 7.4. The view factors only depends of the theta angle (Equation 7.4), therefore only have to be calculated once. There is only an exception with the

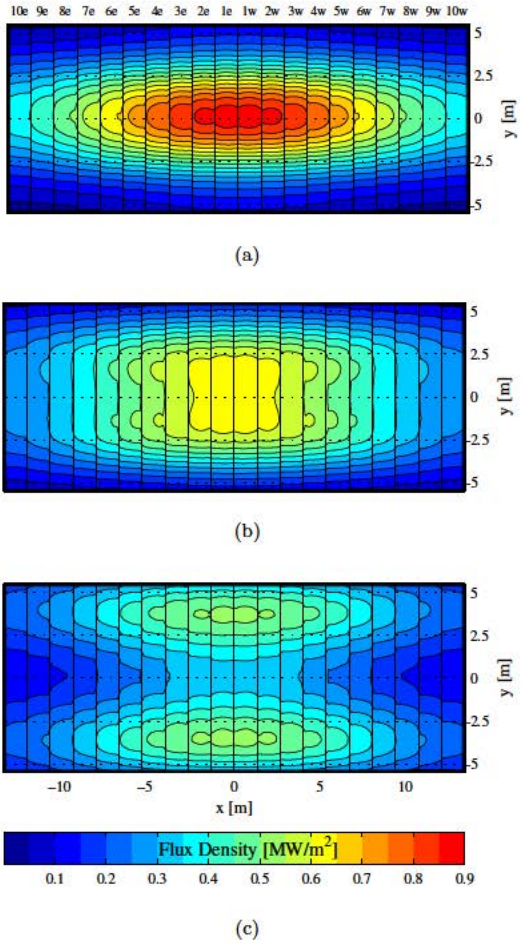

Figure 7.2: Solar flux density intercepted by a receiver formed by 14 panels and for different aiming strategy: a) k=3, b) k= 2, and c) k=1.

first half tube of each panel that is in front of the last half tube of the previous panel, and vice-versa. In these cases the different distance between tubes has to be taken into account.

The whole receiver has to be solved panel by panel, and some iteration is needed. As all the tubes of a panel have not the same solar incident flux the bulk temperature at the outlet of each tube of the same panels can vary, see Equation 7.8. Figure 7.5 represents the salt temperature evolution for the first

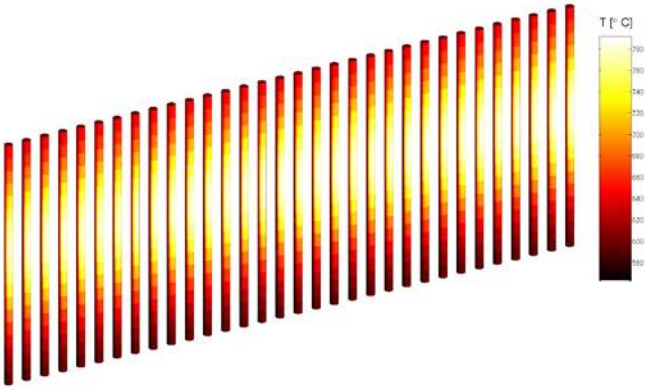

Figure 7.3: Front part view of the tube wall temperature for all the tubes of the first panel for a receiver Solar Two like (24 panels with 32 tubes per panel).

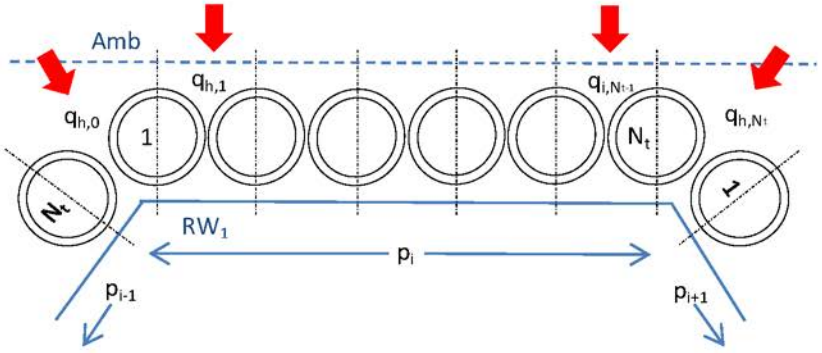

Figure 7.4: Scheme of calculation for the panel i of the receiver.

and last tube of the ninth panel of Solar Two receiver. It is necessary to test if the outlet bulk temperature difference between tubes is negligible or if it modifies enough the properties of the salt to change the pressure drop and the mass flow rate per each tube. In Solar Two receiver, which has large number of narrow panels, the maximum outlet temperature difference found is 1.8 °C, then there is not problems with the properties variation. Note that it has been assumed that the fulfilled of the tubes is only affected by the pressure drop and not by the manifold. Once one panel is solved, the average outlet salt temperature of all the tubes of this panel is used as the inlet temperature for all the tubes of the following panel (see Equation 7.3).

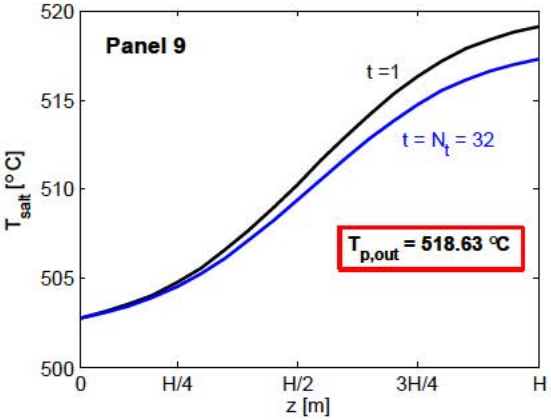

Figure 7.5: Salt temperature distribution for the first and last tubes of the ninth panel of the Solar Two receiver.

To solve the radiative heat transfer of each panel it has employed the net radiation method (Modest, 2003). In addition it is necessary to take into account that the flow direction between panels is opposed. Moreover, for the first panel it has been assumed symmetry between the first tubes of both flow paths. As the first tube of the following panel is not solved yet it has been assumed the values of the first approximation or of the previous iteration. Figure 7.6 and the following equations help to a better understanding of the problem.

$$T_{in}(p) \Rightarrow \text{From the previous panel or data fro } 1^{st} \text{ panel.} \tag{7.2}$$

$$T_{out}(p) = \frac{\sum_1^{N_t} T_{salt}(p,t,Nz)\dot{m}(t)Cp}{\sum_1^{N_t} \dot{m}(t)Cp} \tag{7.3}$$

$$F_v(\theta) \Rightarrow \text{Crossed string method.} \tag{7.4}$$

$$T_{amb} = \sqrt[4]{\frac{\epsilon_{sky}T_{sky}^4 + \epsilon_{ground}T_{ground}^4}{\epsilon_{sky} + \epsilon_{ground}}} \Rightarrow \text{Constant} \tag{7.5}$$

$$q_h''(p,t,z) \Rightarrow \text{From the heliostat field.} \tag{7.6}$$

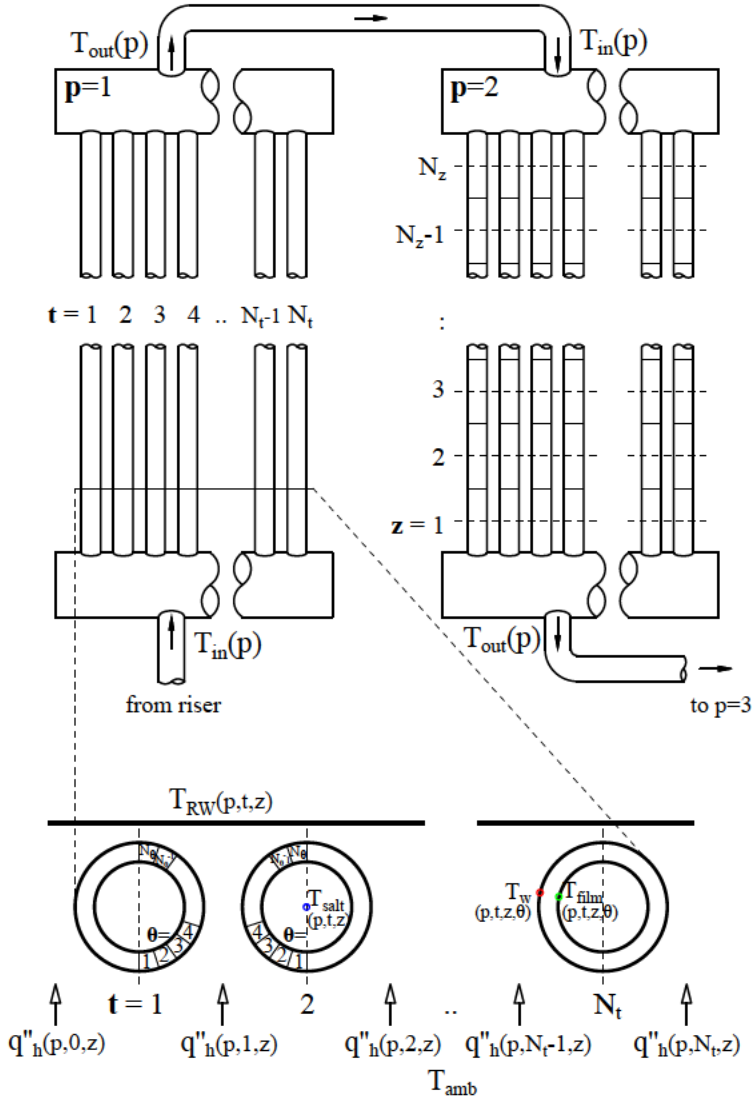

Figure 7.6: Scheme of the receiver flow path and the main variables of calculation.

$q''_t(p,t,z,\theta) = f(q''_h, Fv(\theta), \alpha_t, \epsilon_t) \Rightarrow$ From net radiation method (Modest, 2003).

(7.7)

$$T_{salt}(p,t,z) = T_{in}(p) + \frac{z}{\dot{m}(t)Cp}\sum_{1}^{N_\theta} q_t''(p,t,z,\theta)pr(\theta) \tag{7.8}$$

$$T_w(p,t,z,\theta) = T_{salt}(p,t,z) + \frac{q_t''(p,t,z,\theta)}{U(z)} \tag{7.9}$$

$$T_{film}(p,t,z,\theta) = T_w(p,t,z,\theta) - \frac{1}{2}q_t''(p,t,z,\theta)\frac{dt_{ext}ln\frac{dt_{ext}}{dt_{int}}}{k_t(p,t,z)} \tag{7.10}$$

$$T_{RW}(p,t,z) = f(q_h'', Fv(\theta), \alpha_t, \epsilon_{RW}) \Rightarrow \text{From net radiation method (Modest, 2003).} \tag{7.11}$$

Where parameters panel (p), tube (t), z and θ go as $p = 1, 2, \ldots N_p$; $t = 1, 2, \ldots N_t$; $z = 1, 2, \ldots N_z$; and $\theta = 1, 2, \ldots N_\theta$. T_{in} and T_{out} correspond to the inlet and outlet temperature of the salt in each panel. Cp is the specific heat flux of the salt, $\dot{m}(t)$ the salt mass flow rate per tube, and $U(z)$ the global heat transfer coefficient. $Fv(\theta)$ corresponds to the view factors, dt_{int} represents the internal diameter of the tubes, $pr(\theta)$ is the perimeter of a section of tube, $k_t(p,t,z)$ depicts the conductive coefficient of the tubes, α_t represents the tube absorptivity, ϵ_t is the tube wall emissivity as a funtion of the temperature, and ϵ_{RW} is the emissivity of the refractory wall. T_{salt} is the bulk temperature of the salt, T_{amb} the ambient temperature, T_w the external wall temperature of the tubes, T_{film} the internal temperature of the tube wall, and T_{RW} the temperature of the refractory wall. On the other hand, q_h'' represents the solar flux density on the receiver from the heliostat field, and q_t'' the heat flux absorbed by each tube section.

Finally, to complete the analysis new terms have been included in the thermal model to take into account the increment of pressure in the receiver when the bulk temperature increases. First of all, it is necessary to calculate the minimum allowable tube thickness, th_{min}. It is a function of the maximum pressure in the receiver, th_p (Kolb, 2011), plus an extra thickness that take into account the expected corrosion during the whole service life of the receiver, th_{corr} , see Equation 7.12.

$$th_{min} = th_p + th_{corr} \tag{7.12}$$

The corrosion rate of the different materials at the corresponding work temperature has been obtained from literature: 16.8 μm/year for Inconel 625 (McConohy & Kruizenga, 2014), 20 μm/year for alloy 800H (Bradshaw, 1987), and 688 μm/year for Haynes 230 based on 1025 hours data (McConohy & Kruizenga, 2014). A corrosion rate of 688 μm/year for Haynes 230 means a th_{corr}= 2 cm during the whole service life of the SPT that it is not allowable. Therefore, it has been assumed that this value is only for the first hours of contact and after that there is a diminishing in the corrosion rate, using an acceptable corrosion rate of 53.6 μm/year. In addition, the maximum pressure stress in the three directions has been added to the model. They have been calculated with the equations developed by Neises & Gray (2014), see Equation 7.13. Being Ps_{in} the internal pressure of the tube.

$$\begin{cases} \sigma_{p,r} = \frac{Ps_{in} dt_{in}^2}{dt_{ext}^2 - dt_{in}^2} \left(1 - \frac{dt_{ext}}{dt_{in}^2}\right) \\ \sigma_{p,\theta} = \frac{Ps_{in} dt_{in}^2}{dt_{ext}^2 - dt_{in}^2} \left(1 + \frac{dt_{ext}}{dt_{in}^2}\right) \\ \sigma_{p,z} = \frac{Ps_{in} dt_{in}^2}{dt_{ext}^2 - dt_{in}^2} \end{cases} \tag{7.13}$$

7.5 Results

In this section has been selected the optimal receiver design for each of the three SPT: subcritical (565 °C), supercritical (600 °C), and ultra-supercritical (650 °C) based on the limiting thermal, mechanical and hydrodynamic criteria exposed above, and maximizing the thermal heliostats-receiver efficiency.

The optimum receivers and the whole SPT efficiencies obtained have been compared between them. In addition, it has been calculated the efficiency of the SPT for different loads, to observe the main differences between the three plants during their whole range of operation. To complete the comparison between the different SPT studied the relative cost of the three SPT has been estimated in order to evaluate the main economical and technical advantages and disadvantages of each plant.

7.5.1 Optimum receiver

Figure 7.7 shows different sub-graphs that represent the heliostat-receiver thermal efficiency for the three bulk temperature levels and materials studied (rows): Inconel 625 (565 °C), Alloy 800H (600 °C) and Haynes 230 (650 °C). The graph columns depict different aiming strategies, k, whose values are 2.5, 2, and 1.5.

Each sub-graph of Figure 7.7 includes the thermal efficiency for 210 receiver configurations resulting of the combination of the three last columns of Table 7.1: number of panels, tube diameter, and tube thickness. The x-grid separations define the receiver configurations with same number of panels but different tube diameter and tube thickness (35 different designs: 7 x 5). The x axis from 0 to 42 defines the different possible configurations combining the tube diameter and the number of panels (7 x 6). Per each x data five points are plotted corresponding to the five possible thickness of each tube diameter. Inside the graphic, the tube diameter is portrayed by symbols and the tube thickness by colours as the legends indicate.

In Figure 7.7, it can be observed that the level of temperature of the SPT and the properties of the different materials affect to the heliostat-receiver thermal efficiency. At higher bulk temperature, larger heat losses and lower thermal efficiency. To increase the thermal efficiency the most influent parameter is the aiming factor, k, for each 0.5 reduction in the aiming strategy the heliostats-receiver efficiency decreases close to 2%. Then, the aiming factor has to be as higher as possible allowed by the mechanical and thermal limitations of the materials. The number of panels, the tube diameter and the tube thickness do not influence with a clear pattern in the efficiency. However, the efficiency is function of the absorbance surface. Hence, the efficiency is lower with configurations less compact, for example use 18 or 20 panels with 73 mm diameter is not recommend for the studied receiver geometry.

Figure 7.8 illustrates the maximum film temperature for the different receiver configurations showed in Figure 7.7. It can be seen that the tube film temperature decreases with the number of panels. Higher number of panels means narrower panels with less number of tubes, increasing the salt velocity and the convective coefficient.

The tube diameter has two contrary effects, reduction of the number of tubes per panel and increment of the flow surface. The last factor is the most important, then higher tube diameters means larger film temperatures. The tube thickness reduces the film temperature, although its effect is negligible compared with the tube diameter and the number of panel variations. Using the same arguments the pressure drop evolution has to be contrary to the film temperature increment.

The aiming strategy is also a decisive factor in the increment of the film temperature; higher peak flux means larger maximum film temperature. It can be seen that due to the elevated film temperature it is impossible to use aiming

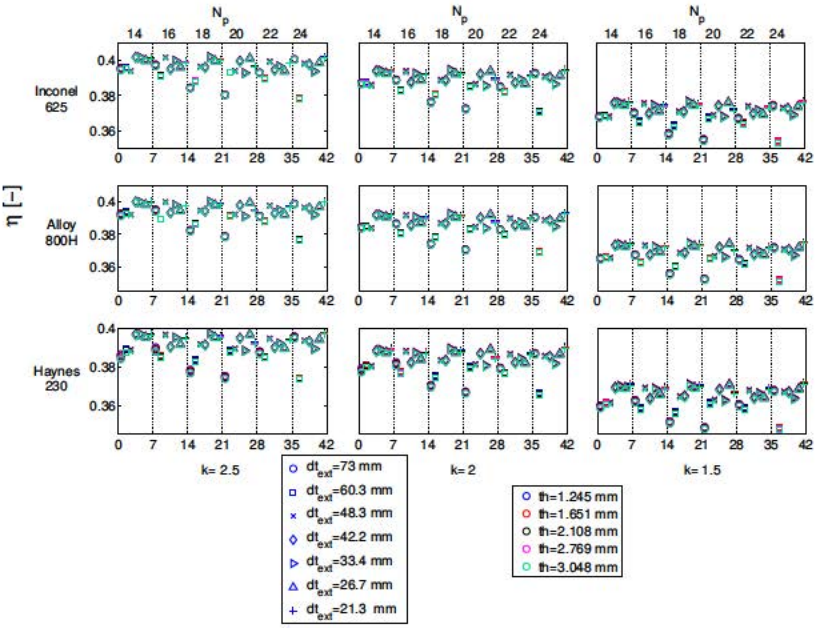

Figure 7.7: Heliostats-receiver thermal efficiency for the different aiming strategy and receiver configurations studied.

strategies, k, higher than 2. Hence, higher values of k has not been represented due to they are out of range of receiver operation; Figure 7.8 shows that film temperature is one of the most decisive factors to take into account to design a receiver. In addition, for lower aiming factors most of the configurations have to be also excluded like possible receiver configurations.

Figure 7.8 does not show the position of the maximum film temperature. But it is varies in function of the aiming strategy, and the receiver configuration.

Figure 7.9 depicts the minimum allowable tube thickness for each receiver configuration as a function of the pressure obtained inside the tubes, the thermal stress of the tubes, and the safety corrosion thickness. Minimum allowable tube thickness evolves as film temperature. It can be seen that Inconel 625 is the most safety material and need lower tube thickness; therefore all the thickness studied for this material could be valid. Haynes 230 behaves worse than Inconel 625 instead of their similar mechanical properties; it is mainly cause by the corrosion effects. Haynes 230 presents similar allowable thickness than Alloy 800H, with worse mechanical properties but better behaviour to corrosion.

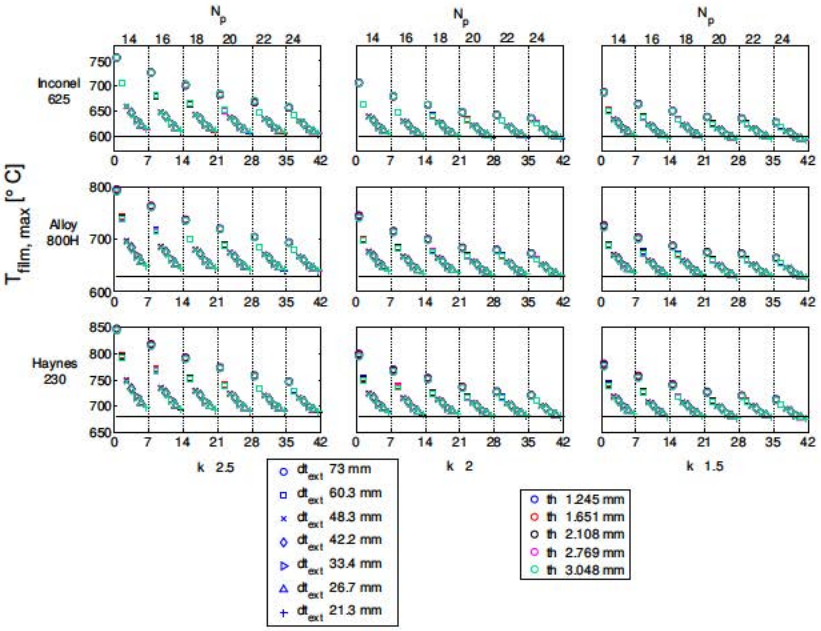

Figure 7.8: Maximum film temperature for the different aiming strategy and receiver configurations studied.

Paying attention to the configurations that fulfil the film temperature and maximize the efficiency it can be seen that Inconel 625 has not lower thickness limit, Alloy 800H cannot be used for tube thickness lower than 1.651 mm, and Haynes 230 has to be used for tube thickness of at least 2.108 mm.

Figure 7.10 portrays the total stress in the receiver. The thermal stress increases with the tube thickness and with the tube diameter, and decreases with the number of panels. It can be seen that for Inconel 625 and Haynes 230, the stress is not a critical factor, and for $k \leq 2$ all the receiver configurations can be used. Alloy 800H has worse mechanical properties and the receiver selection is more critical, being its maximum allowable thickness 2.769 mm.

Although it is not showed in Figure 7.10, it is necessary to highlight that the thermal stresses are higher than the pressure stresses. In addition, the maximum tube stresses are always located on the panel with the highest solar flux (first panel for the design point).

Figure 7.11 depicts the total pressure drop results for the different receiver configurations studied. It takes into account the hydrostatic pressure and the

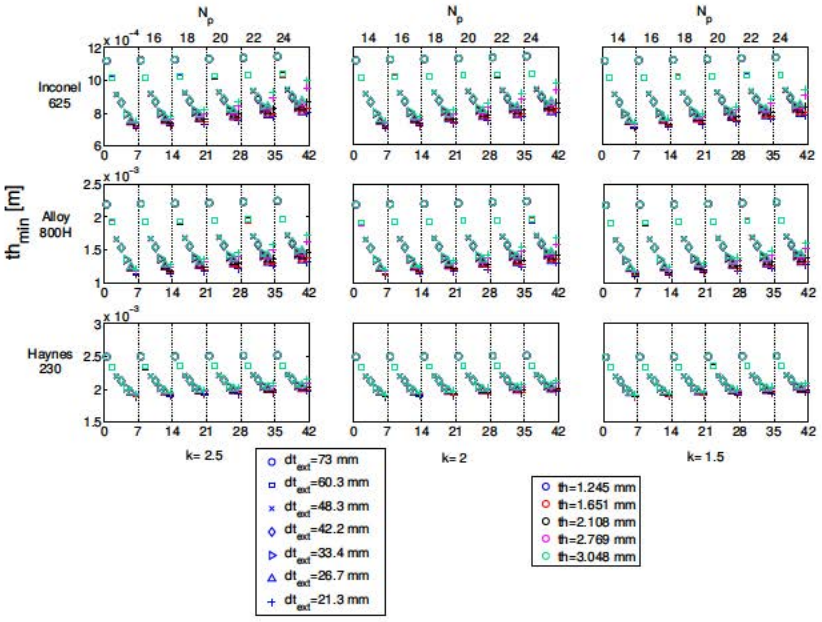

Figure 7.9: Minimum allowable tube thickness for the different aiming strategy and receiver configurations studied.

receiver thermal losses. The pressure drop clearly increases with the number of panels and the tube thickness, and decreases with the tube diameter. Pressure drops higher than 20 bars is not recommendable because it increases the parasitic consumption of the plant.

The optimal receiver designs have been chosen evaluating all the factors explained above. It is necessary to look for a solution of compromise between the maximum pressure drop and the film temperature, trying to maximizing the heliostat-receiver efficiency, but without penalise in excess the parasitic consumption of the plant.

After a first analysis the preliminary optimal receiver design for each SPT level has been selected, see Table 7.2. It can be seen that the aiming strategy, the number of panels, the tube diameter and the tube thickness vary depending on the material properties and the expected final bulk temperature. In all the cases the number of panels in the receiver is elevated, it could change using an optimized aiming strategy capable to adapt to the receiver behaviour.

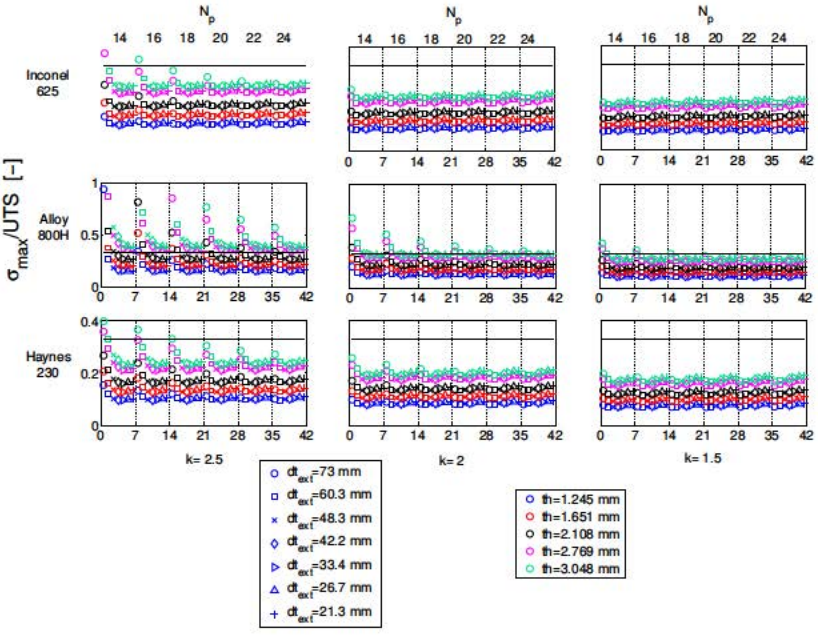

Figure 7.10: Maximum stress for the different aiming strategy and receiver configurations studied.

Table 7.2: Optimal receiver design geometry for the three levels of SPT.

	Sub	**Super**	**Ultra**
Material	Inconel 625	Alloy 800H	Haynes 230
Bulk temperature [°C]	565	600	650
k	2	1.5	1.5
$\mathbf{N}_p$	24	20	24
$\mathbf{N}_t$	48	57	38
$\mathbf{dt}_{ext}$ **[mm]**	21.3	21.3	26.7
th [mm]	1.245	1.651	2.108

7.5.2 Whole thermal model vs. Simplified thermal model

The optimal receiver design must have temperatures and stresses close to the allowable limits in order to maximize the power generated by the SPT without suffers damages. However, there are small differences between the whole ther-

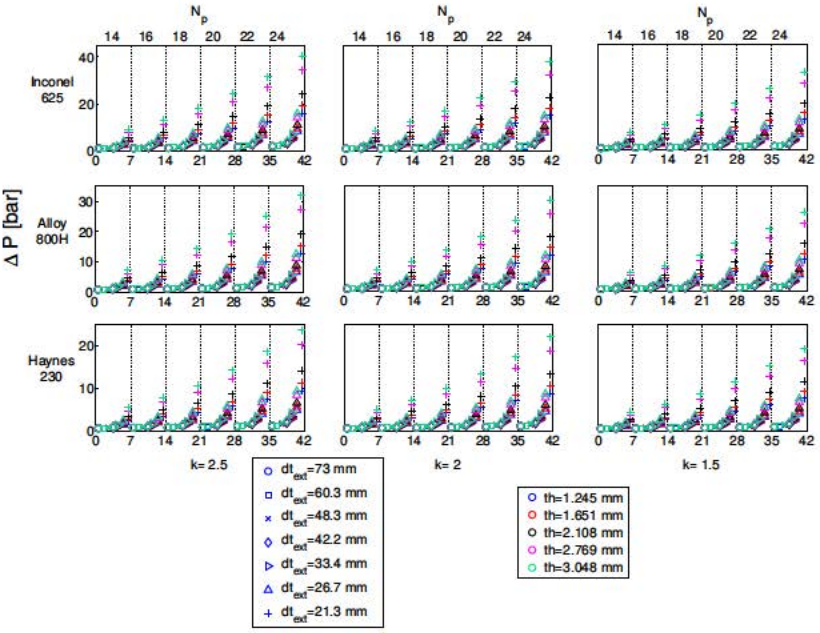

Figure 7.11: Total pressure drop for the different aiming strategy and receiver configurations studied.

mal model and the simplified one, which could mark the difference between an optimum receiver and a receiver that fails before to finish the planned lifetime.

The simplified thermal model is useful to do a sweep of parameters and to select a serial of preliminary designs. Nevertheless, once the preliminary optimal receiver design has been selected, it is necessary to study this design with the full thermal model in order to assure that all the tubes of the receiver fulfil the limiting thermal and mechanical criteria. In addition, the whole receiver thermal model permit to know where are located the most critical tubes in the receiver, allowing to pay special attention to those tubes during the receiver service.

Figure 7.12 shows the main differences found between the simplified thermal model and the whole receiver model for the optimal receivers. The values for film temperature and thermal stresses are always higher for the whole receiver model, due to it does not operates with the panel average. Maximun differences of 4.2 °C in T_{film} have been found; they are in the supercritical model due to it has the lower number of panels and then the widest. Then in the design of

receiver with low number of panels we have to pay attention to the limits of the simplified model. It can be seen that the whole receiver model for supercritical and ultra-supercritical model overpass in 1 °C the film temperature, but it can be considered negligible.

Paying attention to the thermal stresses supercritical receiver has again the maximum differences. They are higher than for film temperature, 16%. It means that the tube stresses estimated with simplified thermal model are the half of the true stress; therefore much attention has to be paid in thermal stresses, that seem not critical for the simplified models, and now are close to the 33% allowable. Pressure drop with the full model is also higher, and in all cases is close to 20 bars, it is unavoidable due to elevated number of panels in the receiver.

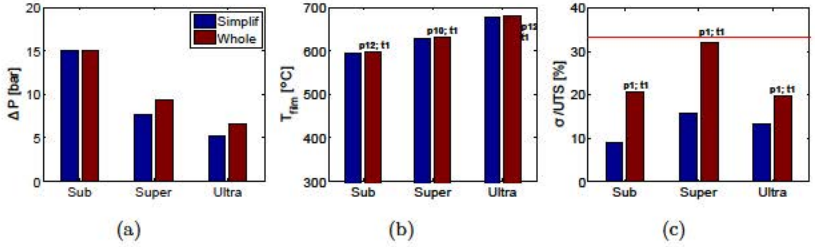

Figure 7.12: Main thermal and mechanical results for the three levels of SPT using the simplified model and the whole receiver model. a) Pressure drop comparison. b) Maximum film temperature comparison. c) Maximum normalized thermal stress comparison.

Comparison

The efficiencies obtained from the main system of the SPT using the optimal receiver configurations are shown in Figure 7.13. The power block efficiencies have been obtained from bibliography, and they correspond to dry cooled SPT (Kolb *et al.*, 2007).

Although, the power block efficiency of supercritical plants is 5.5% higher than subcritical power block, the global SPT efficiency is only 1% higher. It is caused by the lower bulk temperature of subcritical SPT that reduces the thermal losses and increases the thermal efficiency of the receiver; it is also caused by the better mechanical properties of the Incoloy 625 that allows to increase the flux concentration rate (higher k value), enlarging the heliostat

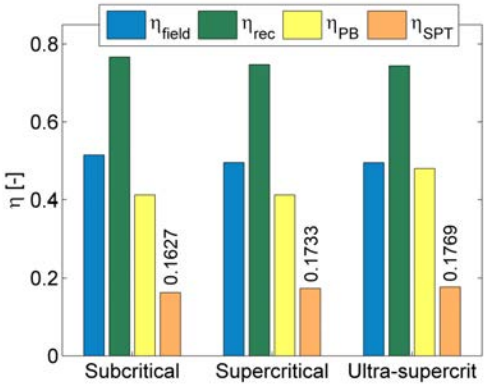

Figure 7.13: Efficiencies at nominal load for the different elements of a SPT, for the three Rankine power blocks studied.

field efficiency. In the same way ultra-supercritical plants have a global SPT efficiency 1.4% higher than subcritical plant, instead of 7% difference of the power block efficiency. In this analysis the parasitic consumption of the plant due to the pressure drop has not been taken into account, and it must be highlighted that for subcritical SPT the pressure drop is 3 times the pressure drop of ultra-supercritical SPT. Despite that the relative global efficiency increment between subcritical and supercritical SPT due to parasitic consumption can be considered negligible.

Different power loads

In this subsection, the authors want to find the real difference between real subcritical, supercritical and supercritical SPT. To do that, it is necessary to forget the nominal conditions of the receiver and apply the thermal cycles typical of a receiver under operation. It has been assumed that the SPT has not got thermal storage, and then both the receiver and the power block always work each other at same power load.

The procedure follows to obtain the efficiency of the main system of the SPT at different loads is to calculate the SPT at half power, putting out of order one half of the heliostats of the field as Pacheco (2002) did for Solar Two pilot plant.

Once the receiver efficiency at 100% and 50% load is known it is possible to calculate the thermal efficiency of the receiver for every power load. Rodríguez-

Sánchez & Santana (2015) developed a model to estimate the receiver efficiency at partial power load as a function of the receiver thermal losses. The receiver thermal losses have a linear relation with the incident power, see Equation 7.14 7.157.16.

Where L_{th} are the thermal losses of the receiver at nominal power load, L'_{th} represent the thermal losses at the desired load. P'_{inc}/P_{inc} corresponds to the ratio of incident power in the receiver between the desired power load and the nominal one. a and b are typical parameters of each solar receiver.

$$L'_{th}/L_{th} = y = aP'_{inc}/P_{inc} + b \tag{7.14}$$

$$\eta_{rec} = \frac{P_{abs}}{P_{inc}} = \frac{P_{inc} - L_{th}}{P_{inc}} \tag{7.15}$$

$$\frac{\eta'_{rec}}{\eta_{rec}} = \frac{(P'_{inc} - L'_{th})\, P_{inc}}{(P_{inc} - L_{th})\, P'_{inc}} \tag{7.16}$$

The efficiency of the heliostat field is constant for the different power loads, due to the aiming strategy used for all the power load is the same. However, the availability of the field decreases with the thermal load, and also the solar flux concentration rate. To calculate the Rankine turbine efficiency at different power load, it has been assumed that the evolution is identical for the three SPT levels. In addition, the power block efficiency is assumed to be only a function of the mechanical efficiency of the turbine. Erhart & Infield (2011) obtained the mechanical efficiency of a turbine at different loads.

Figure 7.14(a) shows the receiver thermal losses evolution as a function of the incident power. These relations are only valid for turbulent regime of the HTF, it means until 50% of load in the ultra-supercritical receiver studied and until 40% of load for the supercritical receiver. For higher and powerful SPT, that is the tendency in this kind of plants, these relations will be valid for the whole range of operation of the SPT. Figure 7.14(b) depicts the SPT efficiency for the three SPT levels as a function of the incident power. It can be seen that the efficiency difference between the subcritical plant and the others is lower for partial loads than in nominal conditions; there is a critical load in which

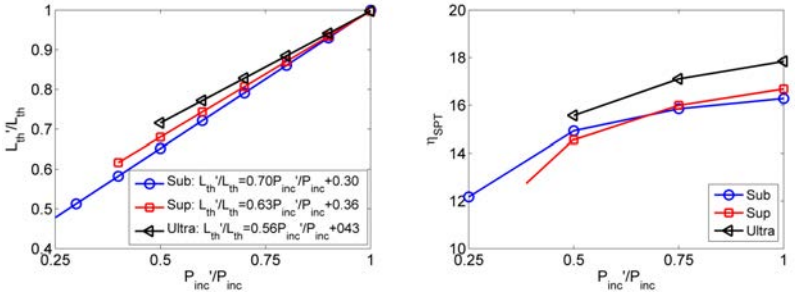

(a) (b)

Figure 7.14: a) Receiver thermal losses ratio for different power loads as a function of the incident power. b) SPT efficiency for different power loads as a function of the incident power.

the SPT efficiency of the subcritical load becomes higher than the others two SPT levels: 70% for supercritical SPT, and 55% for supercritical SPT.

Kolb *et al.* (2007), based on the experimental data of Solar One pilot plant, realised that the solar receiver power level varies each day and on each cloud passage. They concluded that a SPT during 30 years of service made a total of 98,900 cycles of different loads (see Table 7.3). Applying the results of Figure 7.14 to the cycles showed in Table 7.3 it has been obtained the average efficiency along 30 years for the three different SPT studied. To calculate cycles at low power load the data obtained in Figure 7.14 have been extrapolated, forgotten the laminar regimen of the salt. The mean global SPT efficiency its whole service plant is 13.74% for subcritical SPT, 12.68% for supercritical SPT, and 13.58% for ultra-supercritical SPT. It means that the SPT subcritical plants have 1% more efficiency than supercritical and 0.2% more than ultra-supercritical considering the whole range of operation of a SPT.

Cost

To complete the SPT comparison, it seems to be interesting to analyse the relative investment cost of the three level s of SPT studied.

The heliostat field cost for the three plants is the same, although the cost of the field does not represent the same percentage of the final cost for the three plants. Table 7.4 shows the relative cost of each SPT system as a function of the whole SPT investment cost for subcritical, supercritical and ultra-supercritical

Table 7.3: Cycle range and number for a whole service SPT

Cycle range	Number of cycles
10%	41,100
20%	15,300
30%	8,900
40%	6,900
50%	4,900
60%	4,000
70%	4,200
80%	4,800
90%	8,000
100%	800

SPT, the data has been obtained from Singer *et al.* (2014). It can be seen that the relative cost increment will be mainly a function of the power block and the receiver material.

Table 7.4: Relative cost of the different systems of a SPT with respect the whole SPT.

	Sub	**Super**	**Ultra**
Relative cost with respect the whole SPT [%]			
Field	38	35.51	38.47
Receiver	17.8	16.35	17.71
Power block	18.8	23.51	25.47

Table 7.5 shows the relative cost of the main system of a SPT. To calculate the receiver cost, the tube material properties (ASME, 2011) have been used to obtain the receiver mass. In addition, the price of each tube material has been acquired from the supplier (Alibaba, 2015). And the power block relative cost has been obtained from Singer *et al.* (2014).

In Table 7.5 it is possible to observe that the investment cost of a supercritical SPT is twice the price of a subcritical SPT, and that an ultra-supercritical SPT is 3.6 times more expensive than a subcritical plant.

Table 7.5: SPT relative cost difference between subcritical, supercritical and ultra-supercritical SPT.

	Sub (Inconel 625)	**Super (Alloy 800H)**	**Ultra (Haynes 230)**
Tube density [kg/m^3]	8440	8030	8970
Tube cost [$/kg]	20-25	30-60	40-80
Receiver volume [m^3]	10.02	13.12	16.80
Receiver cost [M$]	2.114	6.322	12.055
Receiver relative cost [%]	100	300	570
Rankine relative cost [%]	100	118	145
Heliostat field relative cost [%]	100	93.44	101.23
SPT relative cost [%]	**100**	**200**	**362.5**

7.6 Conclusions

In this research it has been study the viability of introducing a new generation of SPT with higher bulk temperatures that allows to use supercritical and ultra-supercritical Rankine power blocks. The power block efficiency of the new SPT generation is a 7% higher than the subcritical power block efficiency. However, the heliostat field and receiver efficiencies of these new plants are worse. The deterioration of the heliostat-receiver efficiency has been studied in order to decide which plant has more possibilities of remain in a future.

Three different SPT have been studied with outlet temperature of the salt of 565 °C, 600 °C, and 650 °C. The heliostat field for the three plants is the same; however the receiver design and tube materials are different. The first thing that could be observed is that the heliostat efficiency for the supercritical and ultra-supercritical SPT is around 2% worst than the subcritical heliostat field efficiency due to the thermal limitations of the new receiver material. The receiver efficiency it is also worse due to higher thermal losses. Therefore, for nominal conditions the global plant efficiency for ultra-supercritical plants is only 1.4% higher than for subcritical plants, and 0.4% than supercritical SPT.

Going into detail about SPT, they do not work always in nominal conditions, else if SPT are subjected to numerous cycles at different power loads. It is possible to appreciate that the new generation of SPT have a drastic decrement

of the plant efficiency at low power loads. Therefore, using a typical number of load cycles for the whole service of the solar plants, it has been obtained that the subcritical power plant global efficiency is 1% higher than supercritical SPT efficiency, and 0.2% higher than ultra-supercritical SPT efficiency. Hence, for normal operation of a SPT it is recommended to use current subcritical SPT that implement a new generation of SPT with higher bulk temperatures.

Another factor to take into account at the time of design a SPT is the investment cost. This factor is also unfavourable to the building of supercritical and ultra-supercritical SPT; they cost respectively 2 and 3.6 times the price of a subcritical SPT.

Therefore, it is needed the birth of new materials that resist the high requirements of the molten salt receivers, and a decrease in the cost of the advanced power blocks to implant a viable new generation of supercritical and ultra-supercritical SPT.

Nomenclature

dt	tube diameter [m]
k	Aiming strategy factor [-]
L	Heat losses [W]
N	Number of elements [-]
P	Power [W]
p	panel [-]
Ps	Pressure [Pa]
q	Heat flux [W/m^2]
Re	reynolds number [-]
S	Maximum allowable stress [Pa]
T	Temperature [° C]
th	Tube thickness [m]
UTS	Ultimate tensile strength [Pa]
z	Tube length coordinate [m]

Greek symbols

η_t	Efficiency [-]
σ	Mechanical stress [Pa]

Subscripts

abs	Absorbed
corr	Corrosion
ext	External
H	Hydrostatic
hel	Heliostat field
inc	Incident
int	Internal
l	Longitudinal
max	Maximum
min	Minimum
p	Pressure
p	Panel
PB	Power block
r	Radial
rec	receiver
SPT	Solar power tower
t	Tube
th	Thermal
θ	Azimuthal

Abbreviattions

HTF	Heat transfer fluid
SPT	Solar power tower

References

Alibaba 2015 Alibaba Group www.alibaba.com/product-detail/high-temperature-alloy-inconel-625-seamless_1988810062.html?s=p.

ASME 2011 ASME Boiler and Pressure Vessel Code, Section II - Materials. *Tech. Rep.*. American Society of Mechanical Engineers, New York.

Boerema, N.; Morrison, G.; Taylor R. & Rosengarten, G. 2013 High temperature solar thermal central-receiver billboard design. *Solar Energy* 97, 356–368.

Boerema, N.;, Morrison, G.;, Taylor, R. & Rosengarten, G. 2012 Liquid sodium versus Hitec as a heat transfer fluid in solar thermal central receiver systems. *Solar Energy* 86 (9), 2293–2305.

Bradshaw, R.W. 1987 Thermal Convection Loop Study of the Corrosion of Incoloy 800 in Molten $NaNO_3$-KNO_3. *Corrosion-Nace* 43 (3), 173–178.

Collado, F.J.; Gómez, A. & Turégano, J.A. 1986 An analytic function for the flux density due to sunlight reflected from a heliostat. *Solar Energy* 37, 215–34.

Erhart, T.; Eicker, U. & Infield, D. 2011 Part-load characteristics of Organic-Rankine-Cycles. *2nd European Conference on Polygeneration* pp. 1–11.

Kolb, G.J. 2011 An Evaluation of Possible Next-Generation High-Temperature Molten-Salt Power Towers. *Tech. Rep.* December. Sandia National Laboratories, Alburquerque and Livermore, SAND20011-9320.

Kolb, G.J.; Jones, S.A.; Donnelly M.W.;, Gorman, D, ; Thomas R.; Davenport R. & Lumia, R. 2007 Heliostat Cost Reduction Study. *Tech. Rep.* June. Sandia National Laboratories, Albuquerque, SAND2007-3293.

Litwin, R.Z. & Park, C. 2002 Receiver System: Lessons Learned from Solar Two Receiver System. *Tech. Rep.* March.

Lovegrove, K & Stein, W 2012 *Concentrating solar power technology: principles, developments and applications*. Cambridge (U.K.).

Mar, R.W. & Kramer, C.M. 1980 Pressure-temperature-composition relationships for heated draw salt systems. *Solar energy materials* 5, 71–79.

McConohy, G. & Kruizenga, A. 2014 Molten nitrate salts at 600 and 680 °C: Thermophysical property changes and corrosion of high-temperature nickel alloys. *Solar Energy* 103, 242–252.

McGovern, Ronan K. & Smith, William J. 2012 Optimal concentration and temperatures of solar thermal power plants. *Energy Conversion and Management* 60, 226–232.

Modest, F Michael 2003 Radiative Heat Transfer. In *Radiative Heat Transfer*, Second edi edn. (ed. Elsevier Science), chap. 5. RADIATI, pp. 162–197. New York, San Francisco, London.

Neises, T.W.; Wagner, M.J. & Gray, A.K. 2014 Structural Design Considerations for Tubular Power Tower Receivers Operating at 650 °C. *Tech. Rep.* April.

Olivares, R.I. 2012 The thermal stability of molten nitrite/nitrates salt for solar thermal energy storage in different atmospheres. *Solar Energy* 86 (9), 2576–2583.

Pacheco, J.E. 2002 Final Test and Evaluation Results from the Solar Two Project. *Tech. Rep.* January. Sandia National Laboratories, Albuquerque, SAND2002-0120.

Petukhov, B.S. 1970 *Heat Transfer and Friction in Turbulent Pipe Flow with Variable Physical Properties*, , vol. 6. Moscow (USSR).

Rodríguez-Sánchez, M.R.; Sanchez-Gonzalez, A.;, Marugan-Cruz, C. & Santana, D. 2015 Flow patterns of external solar receivers. *Solar Energy* Submitted for publication.

Rodríguez-Sánchez, M.R.; Sánchez-González, A. & Santana, D. 2015 Revised receiver efficiency of molten-salt power towers. *Renewable and Sustainable Energy Reviews* Submitted for publication.

Rodríguez-Sánchez, M.R.; Soria-Verdugo, A.; Almendros-Ibáñez J.A; Acosta-Iborra A. & Santana, D. 2014 Thermal design guidelines of solar power towers. *Applied Thermal Engineering* 63 (1), 428–438.

Sánchez-González, A. & Santana, D. 2015 Solar flux distribution on central receivers: A projection method from analytic function. *Renewable Energy* 74, 576–587.

Singer, Cs., Giuliano, S. & Buck, R. 2014 Assessment of Improved Molten Salt Solar Tower Plants. *Energy Procedia* 49, 1553–1562.

CHAPTER
EIGHT

General conclusions and future works

Solar power tower (SPT) technology with molten salt as heat transfer fluid is positioned as one of the most important renewable energy sources to produce electricity in a near future. However, this technology is not totally mature and some improvements are needed to reduce the levelized energy cost (LEC) of the plants and to assure reliable and safe operation during at least the 30 years of service recommended. This PhD thesis presents the guidelines to design a solar external receiver that assures the safety operation of the plant and maximizes its thermal efficiency.

First, to reduce the LEC it is necessary to increment the whole SPT efficiency. In chapter 2 the use of Potencial Energy Recovery System (PERS) has been proposed. The PERS reduces the parasitic consumption of the SPT, recovering part of the potential energy of the hot fluid that goes from the receiver (top of the tower) to the storage tanks (bottom of the tower). Currently this energy is dissipated and wasted. At high molten salt flow rates the PERS saves up to 75% of the feed pump energy consumption.

In chapter 3 a 2-D simplified model has been developed and compared with CFD simulations. Under turbulent regime, slight differences have been found. Moreover the simplified model needs lower computational cost, becoming a very useful tool for the initial design of solar external receivers.

In chapter 4 it was depicted that the 2-D simplified receiver model leads to receiver thermal efficiencies around 10% lower than other numerical calculations find in the literature. The heat losses, calculated with the model presented in this thesis, are higher due to the consideration of circumferential variations of the temperature of radiation. In addition, the Biot number influence is typically neglected, however, it has been demonstrated that the Biot number in the receivers is not small and plays an importance role on the receiver efficiency. In relation to this, it has been shown that the heat losses cannot be considered constant with the incident power in the receiver, but rather they vary linearly.

Regarding the optimum design of the solar receivers, in chapter 5 different receivers geometries have been studied. The number of panels and the diameter of the tubes have been varied. Mechanical, thermal and hydrodynamic limits have been imposed as a function of the tube material and pump specifications. It has been seen that the most critical factors in the receiver operation are the mechanical stresses and the film temperature of the tubes. The mechanical stresses can cause the failure of the tubes by fatigue or stress corrosion cracking (SSC). They are located in the panels with higher flux density (north panels at solar noon). The maximum film temperature is responsible for the tube corrosion. In this case the extreme conditions are not necessarily placed in the same panels that the mechanical stresses. The maximum film temperature is even more critical than the thermal stress and it is located at eastern/western panels at solar-noon, where the molten salt has already reached a high temperature and the solar flux density is elevated.

Besides, it is important to take into account the flow path configuration in the receiver. In chapter 6 of this dissertation it has been proved that in the north hemisphere the most adequate receiver flow path configuration is when the flow exits by the south side of the receiver to reduce the thermal stresses. In addition, it is more desirable a configuration formed by two parallel flow paths to reduce the pressure drop for a given load. The peak flux on the receiver is displaced along the day from west to east passing by the north side. The possibility of implementing crossovers between the flow paths to balance the sum of energy flux in both flow paths has been also studied in chapter 6. However, it has been shown that it is more important to obtain a flux distribution with the peak flux far of the southern panels than to fulfil the energy balance between paths. Therefore, the best receiver design would be a varying flow configuration along the day, which consists on one crossover before the middle of the path during the sunrise and sunset, and no crossover when the solar flux is elevated and not symmetric with respect to north-south axis. If this variation is not possible, the most appropriate configuration is not crossing, since it is more important a safe operation in the hours of maximum peak flux than during the start-up and shut-down.

The SPT efficiency can also be enhanced by increasing the efficiency of one of the three main systems of the plant: the heliostat field, the receiver and the power block. The power block used in this kind of plants is typically the well-known subcritical Rankine cycle. In the chapter 8 of this thesis it has been studied the possibility to increase the inlet temperature of the vapor. To

obtain a better quality of the steam and to employ supercritical and ultra-supercritical Rankine cycles, it is necessary to increase the outlet temperature of the molten salt in the receiver. However, the increment of efficiency in the power block is comparable with the reduction of efficiency in the receiver due to higher heat losses produced by higher temperatures. In addition, these new power blocks are more expensive and complex than subcritical Rankine cycles, and the new receiver would need more resistant materials, that also are more expensive. Therefore, the new generation of SPT will be only recommended when the prices of materials and systems decrease considerably.

Overall, the results of this PhD thesis show that the external receiver of each SPT must be particularly analyzed, but there are some common guidelines for all of them based on thermal and mechanical limitations. In addition, it has been demonstrated the importance of taking into account the circumferential variations of the temperature to improve the estimation of the receiver efficiency. That can help to design a more accurate heliostat field, reducing costs and assuring the generation of the nominal power of the plant.

Alphabetical list of references

Abe, Osami, Utsunomiya, Taizo & Hoshino, Yoshio 1984 The thermal stability of binary alkali metal nitrates. *Thermochimica Acta* 78 (1-3), 251–260.

Abengoa 2014 Khi Solar One. *Tech. Rep.*. Abengoa, Upington (South-Africa).

Aicher, T. & Martin, H. 1997 New correlations for mixed turbulent natural and forced convection heat transfer in vertical tubes. *International Journal of Heat and Mass Transfer* 40 (15), 3617–3626.

Alibaba 2015 Alibaba Group www.alibaba.com/product-detail/high-temperature-alloy-inconel-625-seamless_1988810062.html?s=p.

Allen, C.B. & Janz, G.J. 1980 Molten-salts safety and hazards an annotated-bibliography. *Journal of Hazardous Materials* 2, 145–175.

ASME 2011 ASME Boiler and Pressure Vessel Code, Section II - Materials. *Tech. Rep.*. American Society of Mechanical Engineers, New York.

Augsburger, Germain 2013 Thermo-economic optimisation of large solar tower power plants. PhD thesis.

Augsburger, Germain & Favrat, Daniel 2013 Modelling of the receiver transient flux distribution due to cloud passages on a solar tower thermal power plant. *Solar Energy* 87, 42–52.

Ausra 2014 www.ausra.com/technology.

Baker, Aivin F 1990 Techniques for Processing Experimental Data From a Solar Central Receiver to Evaluate the receiver steady-state efficiency. *Journal of Solar Energy Engineering* 112 (February), 6–11.

Beerbaum, S. & Weinrebe, G. 2000 Solar thermal power generation in India - a techno-economic analysis. *Renewable Energy* 21 (2), 153–174.

Benammar, S., Khellaf, a. & Mohammedi, K. 2014 Contribution to the modeling and simulation of solar power tower plants using energy analysis. *Energy Conversion and Management* 78, 923–930.

Berger, X., Buriot, D. & Garnier, F. 1984 About the equivalent radiative temperature for clear skies. *Solar Energy* 32 (6), 725–733.

Besarati, Saeb M., Yogi Goswami, D. & Stefanakos, Elias K. 2014 Optimal heliostat aiming strategy for uniform distribution of heat flux on the receiver of a solar power tower plant. *Energy Conversion and Management* 84, 234–243.

Bezian, J.J. 1986 Themis solar power plant firs evaluation results. In *Biennial Congress of the International Solar Energy Society* (ed. Intersol Eighty Five), pp. 1408–1412. Elsevier.

Blanco, J, Heller, P, Mehos, M, Meier, A & Meyer, R 2010 Solar Power and Chemical Energy Systems Annual Report. *Tech. Rep.*. International Energy Agency (IEA), DLR.

Boerema, N.; Morrison, G.; Taylor R. & Rosengarten, G. 2013 High temperature solar thermal central-receiver billboard design. *Solar Energy* 97, 356–368.

Boerema, N.;, Morrison, G.;, Taylor, R. & Rosengarten, G. 2012 Liquid sodium versus Hitec as a heat transfer fluid in solar thermal central receiver systems. *Solar Energy* 86 (9), 2293–2305.

Bradshaw, R.W. 1987 Thermal Convection Loop Study of the Corrosion of Incoloy 800 in Molten $NaNO_3$-KNO_3. *Corrosion-Nace* 43 (3), 173–178.

Bradshaw, R.W. & Goods, S.H. 2001 Corrosion of Alloys and Metals by Molten Nitrates. *Tech. Rep.*. Sandia National Laboratories, Albuquerque, SAND2000-8727.

Burgaleta, J.I., Arias, S. & Salbidegoitia, I.B. 2009 Operative advantages of a central tower solar plant with thermal storage system. In *SolarPACES*, p. n 11720. Berlin, Germany: SolarPACES.

Burgaleta, Juan Ignacio, Arias, Santiago & Ramirez, Diego 2011 Gemasolar, the first tower thermosolar commercial plant with molten salt storage. In *Solarpaces*, pp. 1–8.

Cheesewright, R., Heggs, P.J., Martin, B.W., Parry, W.J. & Ralston, T. 2001 Forced convection heat transfer in straight tubes. Part 2: laminar and transitional flow. *Tech. Rep.* 93018. ESDU: Chemical Engineers and Mechanical Engineers, London.

Clausing, A. 1981 Analysis of convective losses for cavity solar central receivers. *Solar Energy* 27, 295–300.

Collado, F.J.; Gómez, A. & Turégano, J.A. 1986 An analytic function for the flux density due to sunlight reflected from a heliostat. *Solar Energy* 37, 215–34.

Collado, F.J. 2008 Quick evaluation of the annual heliostat field efficiency. *Solar Energy* 82 (4), 379–384.

Collado, F.J. 2009 Preliminary design of surrounding heliostat fields. *Renewable Energy* 34 (5), 1359–1363.

Collado, F.J. & Guallar, J. 2012 Campo: Generation of regular heliostat fields. *Renewable Energy* 46, 49–59.

Collado, F.J. & Guallar, J. 2013 A review of optimized design layouts for solar power tower plants with campo code. *Renewable and Sustainable Energy Reviews* 20, 142–154.

Cui, Haiting, Wang, Zhenhui, Guo, Yanshu, Xu, Weiqiang & Yuan, Xiugan 2006 Thermal performance analysis on unit tube for heat pipe receiver. *Solar Energy* 80 (7), 875–882.

Dehghan, A.A. & Behnia, M. 1996 Combined natural convection conduction and radiation heat transfer in a discretely heated open cavity. *ASME Journal of Heat Transfer* 118, 54–56.

Derakhshan, Shahram & Nourbakhsh, Ahmad 2008 Experimental study of characteristic curves of centrifugal pumps working as turbines in different specific speeds. *Experimental Thermal and Fluid Science* 32 (3), 800–807.

Dhyia Aidroos, B.; Hasimah Abdul, R.; Wan Zaidi Wan O; & Saeed Obaid, F. 2015 Historical development of concentrating solar power technologies to generate clean electricity efficiently - A review. *Renewable and Sustainable Energy Reviews* 41, 996–1027.

Dixon, S.L. & Hall, C.A. 2014 *Fluid Mechanics and Thermodynamics of Turbomachinery*, 7th edn. Butterworth Heinemann.

DOE 2015 CSP component research and development. energy.gov/eere/sunshot/csp-component-research-and-development.

DOE, NREL; & Sandia 1998 Solar Two. *Tech. Rep.*. http://www.nrel.gov/docs/fy99osti/24643.pdf, Bradshow, California.

Duffie, J A & Beckman, W A 1991 *Solar engineering of thermal processes*. New York: Wiley.

Erhart, T.; Eicker, U. & Infield, D. 2011 Part-load characteristics of Organic-Rankine-Cycles. *2nd European Conference on Polygeneration* pp. 1–11.

eSolar, Brightsource & Abengoa 2008 Solar Thermal technology on an industry scale. *Tech. Rep.*. eSolar, Brightsource, Abengoa Solar.

Falcone, P.K 1986 *A handbook for solar central receiver design*. Livermore, California: Sandia National Laboratories.

Fauple, J.H. & Fisher, F.E. 1981 *Engineering design: a synthesis of stress analysis and material engineering*. New York, USA: Wiley.

Gallego, Belen & Bial, Marcel 2013 CSP Global MARKETS. *Tech. Rep.*. CSP Today.

Garbrecht, Oliver, Al-Sibai, Faruk, Kneer, Reinhold & Wieghardt, Kai 2013 CFD-simulation of a new receiver design for a molten salt solar power tower. *Solar Energy* 90, 94–106.

Gielen, Dolf 2012 Renewable energy technologies: cost analysis series. Concentrating Solar Power. *Tech. Rep.* 2/5. IRENA, Albuquerque.

Gil, A.; Medrano, M.; Martorell I.; Lázaro A.; Dolado P.; Zalba-B. & Cabeza, L.F. 2010 State of the art on high temperature thermal energy storage for power generation. Part 1 - Concepts, materials and modellization. *Renewable and Sustainable Energy Reviews* 14 (1), 31–55.

Gill, D.D.; Kolb, W.J. & Briggs, R.J. 2013 An Evaluation of Pressure Measurement in the Molten Salt Test Loop (MSTL) System (July), 24.

Gnielinski, V. 2013 On heat transfer in tubes. *International Journal of Heat and Mass Transfer* 63, 134–140.

Golden, C. 2015 System advisor model (sam). sam.nrel.gov/content/downloads.

Hefni, B. & Soler, R. 2015 Dynamic Multi-configuration Model of a 145 MWe Concentrated Solar Power Plant with the ThermoSysPro Library (Tower Receiver, Molten Salt Storage and Steam Generator). *Energy Procedia* 69, 1249–1258.

Hering, W.; Stieglitz, R. & Wetzel, T. 2012 Application of liquid metals for solar energy systems. In *EPJ Web of Conferences*, , vol. 33, p. 03003.

Ho, C.K. & Iverson, B.D. 2014 Review of high-temperature central receiver designs for concentrating solar power. *Renewable and Sustainable Energy Reviews* 29, 835–846.

Ho, C.K., Roderick Mahoney, A., Ambrosini, A., Bencomo, M., Hall, A. & Lambert, T.N. 2013 Characterization of Pyromark 2500 Paint for High-Temperature Solar Receivers. *Journal of Solar Energy Engineering* 136 (1), 4.

Hoffschmidt, B., Alexopoulos, S., Göttsche, J., Sauerborn, M. & Kaufhold, O. 2012 *Comprehensive Renewable Energy*. Elsevier.

Huang, Weidong & Xu, Qian 2014 Development of an analytical method and its quick algorithm to calculate the solar energy collected by a heliostat field in a year. *Energy Conversion and Management* 83, 110–118.

Idelchik, I.E. 1986 *Handbook of Hydraulic Resistance*, 3rd edn. New York, USA: Begell House.

Incropera, F.K. & Dewitt, D.P. 1990 *Introduction to heat transfer*, 2nd edn. Indiana, USA: John Wiley and Sons, Purdue University.

International Energy Agency 2012 CO2 emissions from fuel combustion. *Tech. Rep.*. iea.

Irfan, Mohammad a. & Chapman, Walter 2009 Thermal stresses in radiant tubes due to axial, circumferential and radial temperature distributions. *Applied Thermal Engineering* 29 (10), 1913–1920.

Jianfeng, Lu, Jing, Ding & Jianping, Yang 2010 Heat transfer performance of an external receiver pipe under unilateral concentrated solar radiation. *Solar Energy* 84 (11), 1879–1887.

Keith Lovegrove, Muriel Watt, Robert Passey, Graeme Pollock, Joe Wyder, Josh Dowse 2012 Realising the Potential of Concentrating Solar Power in Australia. *Tech. Rep.* May. Australian Solar Institute.

Kennedy, C.E. 2002 Review of mind-to-high-temperature solar selective absorber materials. *Tech. Rep.*. NREL, Colorado, USA, NREL 2002/TP-520-31267.

Kistler, B.L. 1986 A User's Manual for DELSOL3: A Computer Code for Calculating the Optical Performance and Optimal System Design for Solar Thermal Central Receiver Plants. *Tech. Rep.*. Sandia National Laboratories, Albuquerque.

Kolb, G.J.; Ho, C.K.; Mancini T.R. & Gary, J.A. 2011 Power Tower Technology Roadmap and Cost Reduction Plan. *Tech. Rep.* April. Sandia National Laboratories, Sandia National Laboratories, Albuquerque.

Kolb, G.J. 2011 An Evaluation of Possible Next-Generation High-Temperature Molten-Salt Power Towers. *Tech. Rep.* December. Sandia National Laboratories, Alburquerque and Livermore, SAND20011-9320.

Kolb, G.J.; Jones, S.A.; Donnelly M.W.;, Gorman, D, ; Thomas R.; Davenport R. & Lumia, R. 2007 Heliostat Cost Reduction Study. *Tech. Rep.* June. Sandia National Laboratories, Albuquerque, SAND2007-3293.

Lata, Jesús, Alcalde, Sergio, Fernández, David & Lekube, Xabier 2010 First surrounding field of heliostats in the world for commercial solar power plants - Gemasolar. In *Solarpaces* (ed. Sener), pp. 1–9.

Lata, Jesús M., Rodríguez, Manuel & Álvarez de Lara, Mónica 2008 High Flux Central Receivers of Molten Salts for the New Generation of Commercial Stand-Alone Solar Power Plants. *Journal of Solar Energy Engineering* 130 (2), 1–5.

Li, W., Wei, P. & Zhou, X. 2014 A cost-benefit analysis of power generation from commercial reinforced concrete solar chimney power plant. *Energy Conversion and Management* 79, 104–113.

Li, Xin, Kong, Weiqiang, Wang, Zhifeng, Chang, Chun & Bai, Fengwu 2010 Thermal model and thermodynamic performance of molten salt cavity receiver. *Renewable Energy* 35 (5), 981–988.

Liao, Zhirong, Li, Xin, Xu, Chao, Chang, Chun & Wang, Zhifeng 2014 Allowable flux density on a solar central receiver. *Renewable Energy* 62, 747–753.

Lienhard, J.H. IV & Lienhard, J.H. V 2008 *A Heat Transfer Textbook*, third edit edn., *McGraw-Hill Higher Education*, vol. 82. Cambridge, Massachusetts: Phlogiston Press.

Lim, Sehwa, Kang, Yongheack, Lee, Hyunjin & Shin, Seungwon 2014 Design optimization of a tubular solar receiver with a porous medium. *Applied Thermal Engineering* 62 (2), 566–572.

Lipps, F.W. & Vant-Hull, L.L. 1978 A cellwise method for the optimization of large central receiver systems. *Solar Energy* 20 (6), 505–516.

Litwin, R.Z. & Park, C. 2002 Receiver System: Lessons Learned from Solar Two Receiver System. *Tech. Rep.* March.

López-González, D., Valverde, J.L., Sánchez, P. & Sanchez-Silva, L. 2013 Characterization of different heat transfer fluids and degradation study by using a pilot plant device operating at real conditions. *Energy* 54, 240–250.

Lovegrove, K & Stein, W 2012 *Concentrating solar power technology: principles, developments and applications*. Cambridge (U.K.).

Mar, R.W. & Kramer, C.M. 1980 Pressure-temperature-composition relationships for heated draw salt systems. *Solar energy materials* 5, 71–79.

Martín, Helena, De, Jordi, Velasco, Guillermo, Castilla, Miguel, Luís, José & Vicuña, García De 2015 Promotion of concentrating solar thermal power (CSP) in Spain : Performance analysis of the period 1998 - 2013. *Renewable and Sustainable Energy Reviews* 50, 1052–1068.

McConohy, G. & Kruizenga, A. 2014 Molten nitrate salts at 600 and 680 °C: Thermophysical property changes and corrosion of high-temperature nickel alloys. *Solar Energy* 103, 242–252.

McGovern, Ronan K. & Smith, William J. 2012 Optimal concentration and temperatures of solar thermal power plants. *Energy Conversion and Management* 60, 226–232.

Miliozzi, A., Giannuzzi, G.M., Tarquini, P. & La Barbera, A. 2001 Fluido termovettore: dati di base della miscela di nitrati di sodio e potassio. *Tech. Rep.*. ENEA, Italy, ENEA/SOL/RD/2001/07.

Modest, F Michael 2003 Radiative Heat Transfer. In *Radiative Heat Transfer*, Second edi edn. (ed. Elsevier Science), chap. 5. RADIATI, pp. 162–197. New York, San Francisco, London.

Neises, T.W.; Wagner, M.J. & Gray, A.K. 2014 Structural Design Considerations for Tubular Power Tower Receivers Operating at 650 °C. *Tech. Rep.* April.

Nissen, D. a. & Meeker, D. E. 1983 Nitrate/Nitrite Chemistry in NaN03-KN03 Melts. *Inorg. Chem.* 22 (June 1980), 716–721.

Noone, Corey J., Torrilhon, Manuel & Mitsos, Alexander 2012 Heliostat field optimization: A new computationally efficient model and biomimetic layout. *Solar Energy* 86 (2), 792–803.

NREL 2011 http://www.nrel.gov/csp/solarpaces/by_project.cfm.

Okoye, Chiemeka Onyeka & Atikol, UÄ§ur 2014 A parametric study on the feasibility of solar chimney power plants in North Cyprus conditions. *Energy Conversion and Management* 80, 178–187.

Olivares, R.I. 2012 The thermal stability of molten nitrite/nitrates salt for solar thermal energy storage in different atmospheres. *Solar Energy* 86 (9), 2576–2583.

Pacheco, J.E. 2002 Final Test and Evaluation Results from the Solar Two Project. *Tech. Rep.* January. Sandia National Laboratories, Albuquerque, SAND2002-0120.

Pacheco, J.E., Ralph, M.E. & Chavez, J.M. 1995 Investigation of Cold Filling Receiver Panels and Piping in Molten-Nitrate-Salt Central-Receiver Solar Power Plants. *Journal of Solar Energy Engineering* 117 (NOVEMBER), 282.

Pacio, J. & Wetzel, T. 2013 Assessment of liquid metal technology status and research paths for their use as efficient heat transfer fluids in solar central receiver systems. *Solar Energy* 93, 11–22.

Pavlović, T.M.; Radonjić, I.S.; Milosavljević D D. & Pantić, L.S. 2012 A review of concentrating solar power plants in the world and their potential use in Serbia. *Renewable and Sustainable Energy Reviews* 16 (6), 3891–3902.

Perini, Katia & Rosasco, Paolo 2013 Cost - benefit analysis for green façades and living wall systems. *Building and Environment* 70, 110–121.

Persky, M.J. & Szczesniak, M. 2008 Infrared, spectral, directional-hemispherical reflectance of fused silica, Teflon polytetrafluoroethylene polymer, chrome oxide ceramic particle surface, Pyromark 2500 paint, Krylon 1602 paint, and Duraflect coating. *Applied Optics* 47, 1389–1396.

Petukhov, B.S. 1970 *Heat Transfer and Friction in Turbulent Pipe Flow with Variable Physical Properties*, , vol. 6. Moscow (USSR).

Pitz-Paal, R.; Dersch, J. & Milow, B. 2005 European concentrated solar thermal road-mapping. *Tech. Rep.*. ECOSTAR, WP3 Deliverable N7, Cologne, (Germany) SES6-CT-2003-502578.

Price, H. 2003 Assessment of Parabolic Trough and Power Tower Solar Technology Cost and Performance Forecasts. *Tech. Rep.* October. NREL, Chicago.

Pugh, S. J & Garvey, S. J 1993 Forced convection heat transfer in straight tubes. *Tech. Rep.* August. ESDU 92003, London, ESDU 92003.

Radosevich, L.G. 1988 Final Report on the Power Production Phase of the 10MWe Solar Thermal Central Receiver Pilot Plant. *Tech. Rep.*. Sandia National Laboratories. SAN087-8022, Livermore, California.

Re, Munichc 2012 http://www.munichre.com/en/group/focus/climate-change.

Richter, C.; Teske, S. & Short, R. 2009 Concentrating solar power global outlook 09 - why renewable energy is hot. *Tech. Rep.*. Greenpeace International, SolarPACES, ESTELA, Amsterdam.

Rodríguez-Sánchez, M.R.; Sanchez-Gonzalez, A.;, Marugan-Cruz, C. & Santana, D. 2015 Flow patterns of external solar receivers. *Solar Energy* Submitted for publication.

Rodríguez-Sánchez, M.R.; Sánchez-González, A. & Santana, D. 2015 Revised receiver efficiency of molten-salt power towers. *Renewable and Sustainable Energy Reviews* Submitted for publication.

Rodríguez-Sánchez, M.R.; Soria-Verdugo, A.; Almendros-Ibáñez J.A; Acosta-Iborra A. & Santana, D. 2014*a* Thermal design guidelines of solar power towers. *Applied Thermal Engineering* 63 (1), 428–438.

Rodríguez-Sánchez, M.R.; Marugán-Cruz, C.; Acosta-Iborra A. & Santana, D. 2014*b* Comparison of simplified heat transfer models and CFD simulations for molten salt external receiver. *Applied Thermal Engineering* 73, 991–1003.

Romeo, E., Royo, C. & Monzon, A. 200286 Improved explicit equations for estimation of the friction factor in rough and smooth pipes. *Chemical Engineering Journal* pp. 396–374.

Salomé, A.; Chhel, F.; Flamant G.; Ferrière-A. & Thiery, F. 2013 Control of the flux distribution on a solar tower receiver using an optimized aiming point strategy: Application to THEMIS solar tower. *Solar Energy* 94, 352–366.

Sánchez-González, A. & Santana, D. 2015 Solar flux distribution on central receivers: A projection method from analytic function. *Renewable Energy* 74, 576–587.

Schiel, W.J.C. & Geyer, M.A. 1988 Testing an external sodium receiver up to heat fluxes of 2.5 MW/m^2: Results and conclusions from the IEA-SSPS high flux experiment conducted at the central receiver system of the Plataforma Solar de Almeria (Spain). *Solar Energy* 41 (3), 255–265.

Schmitz, M.; Schwarzbözl, P.; Buck R. & Pitz-Paal, R. 2006 Assessment of the potential improvement due to multiple apertures in central receiver systems with secondary concentrators. *Solar Energy* 80 (1), 111–120.

Schwarzbözl, P.; Pitz-Paal, R. & Schmitz, M. 2009 Visual HFLCAL - A Software Tool for Layout and Optimisation of Heliostat Fields. In *SolarPACES*. Berlin, Germany: SolarPACES.

Seia & SolarPACES 2001 Concentrating solar power : Energy from mirrors. *Tech. Rep.*. U.S. Department of energy (DOE), Washington, DOE/GO-102001-1147.

Sener 2015 Gemasolar view.

Serrano, E., Wiesenberg, R., Rayo, D., Barroso, H., Villa, J. & Santana, D. 2011 Solar Power Tower System.

Siebers, D L & Kraabel, J S 1984 Estimating Convective Energy Losses From Solar Central Receivers. *Tech. Rep.*. Sandia, Livermore.

Singer, Cs., Giuliano, S. & Buck, R. 2014 Assessment of Improved Molten Salt Solar Tower Plants. *Energy Procedia* 49, 1553–1562.

Singer, C.; Buck, R.;, Pitz-Paal, R. & MuÌĹller-Steinhagen, H. 2010 Assessment of Solar Power Tower Driven Ultrasupercritical Steam Cycles Applying Tubular Central Receivers With Varied Heat Transfer Media. *Journal of Solar Energy Engineering* 132 (4), 041010: 1–12.

Slemp, W. S. & Wade, W. R. 1962 A method for measuring the spectral normal emittance in air of a variety of materials having stable emittance characteristics. *Tech. Rep.*. NASA, Hampton, VA, United States.

Slusser, J. W., Titcomb, J. B., Heffelfinger, M. T. & Dunbobbin, B. R. 1985 Corrosion in Molten Nitrate-Nitrite Salts. *Journal of Metals* 37 (7), 24–27.

SolarReserve 2014 SolarReserve: Crescent Dunes.

SpainGovernment 2007 Real Decreto 436/2004, de 12 de marzo.

Tenerelli, J. 2000 *Efficiency of the energy conversion*. College of Earth and Mineral Sciences.

Torresol 2010 Torresol Energy: Gemasolar. www.torresolenergy.com/TORRESOL/gemasolar-plant/en.

Towler, G. & Sinnott, R.K. 2013 *Chemical Engineering Design*, 2nd edn. San Diego, California: Elsevier.

Trabish, Herman K. 2013 A Climb Up the SolarReserve Solar Power Tower.

Usaola, Julio 2012 Participation of CSP plants in the reserve markets: A new challenge for regulators. *Energy Policy* 49, 562–571.

USDepartmentEnergy 2013 EnergyPlus Energy Simulation Software.

Vant-Hull, Lorin L. 2002 The Role of Allowable Flux Density in the Design and Operation of Molten-Salt Solar Central Receivers. *Journal of Solar Energy Engineering* 124 (May), 165.

Vignarooban, K.; Xu, X.; Arvay A.; Hsu-K. & Kannan, A.M. 2015 Heat transfer fluids for concentrating solar power systems - A review. *Applied Energy* 146, 383–396.

Wade, W.R. & Slemp, W.S. 1962 Measurements of total emittance of several refractory oxides, cements, and ceramics for temperatures from 600 °F to 2000 °F. *Tech. Rep.*. NASA, USA, Technical Note D-998.

Wagner, M. J. 2008 Simulation and Predictive Performance Modeling of Utility-Scale Central Receiver System Power Plants. PhD thesis, University of Wisconsin, Madison.

Walzel, M.D., Lipps, F.W. & Vant-Hull, L.L. 1977 A solar flux density calculation for a solar tower concentrator using a two-dimensional hermite function expansion. *Solar Energy* 19 (3), 239–253.

Winter, C J, Sizmann, R L & Vant-Hull, L L 1991 *Solar Power Plants*. Berlin, Heidelberg: Springer Berlin Heidelberg.

Xu, Chao, Wang, Zhifeng, Li, Xin & Sun, Feihu 2011 Energy and exergy analysis of solar power tower plants. *Applied Thermal Engineering* 31 (17-18), 3904–3913.

Yang, M.; Yang, X.;, Yang, X. & Ding, J. 2010 Heat transfer enhancement and performance of the molten salt receiver of a solar power tower. *Applied Energy* 87 (9), 2808–2811.

Yang, X.; Yang, X.; Ding J.; Shao-Y. & Fan, H. 2012 Numerical simulation study on the heat transfer characteristics of the tube receiver of the solar thermal power tower. *Applied Energy* 90 (1), 142–147.

Zavoico, A.B. 2001 Solar Power Tower: Design Basis Document. *Tech. Rep.* July. Sandia National Laboratory, San Francisco, SAND2001-2100.

Zhang, H.L.; Baeyens, J.; Degrève J. & Cacères, G. 2013 Concentrated solar power plants: Review and design methodology. *Renewable and Sustainable Energy Reviews* 22, 466–481.

List of publications

As a result of the work of this dissertation, the following papers have been published or submitted for publication:

- The work of chapter 5 resulted in the following publication: M.R. Rodríguez-Sánchez, A. Soria-Verdugo, J.A. Almendros-IbáÃśez, A. Acosta-Iborra, D. Santana. Thermal design guidelines of solar power towers. Applied Thermal Engineering, 63 (2014) 428-438.

- The work of chapter 3 resulted in the following publication: M.R. Rodríguez-Sánchez, C. Marugán-Cruz, A. Acosta-Iborra, D. Santana. Comparison of Simplified Heat Transfer Models and CFD Simulations for Molten Salt External Receiver. Applied Thermal Engineering, 73 (2014) 991-1003.

- The work of chapter 2 resulted in the following publication: M.R. Rodríguez-Sánchez, A. Sánchez-González, C. Marugán-Cruz, D. Santana. Saving assessment using the PERS in solar power towers. Energy Conversion and Management, 87 (2014) 810-819.

- The work of chapter 4 resulted in the following publication: M.R. Rodríguez-Sánchez, A. Sánchez-González, D. Santana. Revised receiver efficiency of molten-salt power towers. Submitted for publication to Renewable & sustainable energy reviews.

- The work of chapter 6 resulted in the following publication: M.R. Rodríguez-Sánchez, A. Sánchez-González, C. Marugán-Cruz, D. Santana. Flow patterns of external solar receivers. Submitted for publication to Solar Energy.

- The work of chapter 7 resulted in the following publication: M.R. Rodríguez-Sánchez, A. Sánchez-González, C. Marugán-Cruz, D. Santana. Evaluation of subcritical, supercritical and ultra-supercritical solar power tower. Submitted for publication to Solar Energy.

The following conference presentations are also an outcome of the thesis:

- The work of chapter 2 resulted in: R. Wiesenberg, M.R. Rodríguez-Sánchez, E. Serrano, J. Villa, H. Barroso, D. Rayo, A. Ruano, D. Santana.

PERS: Potential Energy Recovery System. Proceedings of SolarPaces, Marrakech, Morocco (2012).

- The work of chapter 5 resulted in: M.R. Rodríguez-Sánchez, M. Venegas, C. Marugán-Cruz, D. Santana. Thermal, mechanical and hydrodynamic analysis to optimize the design of molten salt central receivers of solar tower power plants. Proceedings of International Conference on Renewable Energies and Power Quality (ICREPQ), (2013).

In addition, this PhD thesis has transfer technology to industry with a project signed between the Universidad Carlos III de Madrid and the company Beijing Shouhang ihw Resources Saving Technology Co., Ltd. for the design of a solar power tower of 10 MWe with 15 hours storage in Dunhuang (China).

Apart from this work further related papers have also been published in international journals or presented in conferences and a patent has been presented:

- C. Marugán-Cruz, S. Sánchez-Delgado, M.R. Rodríguez-Sánchez, M. Venegas, D. Santana. District cooling network connected to a solar power tower. Applied Thermal Engineering. 79 (2015)174-183

- A. Sánchez-González, M.R. Rodríguez-Sánchez,D. Santana. Aiming strategy model based on allowable flux densities for molten salt central receivers. Submitted for publication to Solar Energy.

- M.R. Rodríguez-Sánchez; M. Venegas; C. Marugán-Cruz; D. Santana. Nuevo diseño de receptores para centrales termosolares tipo torre: receptor bayoneta. Proceeding of CENIT 08, Burgos, Spain, 2013.

- M.R. Rodríguez-Sánchez, A. Sánchez-González, C. Marugán-Cruz, D. Santana. New Designs of Molten-salt Tubular-receiver for Solar Power Tower Plants. SolarPACES 2013, Las Vegas, USA. Energy Procedia 49, 504-513, 2014.

- C. Marugán-Cruz, S. Sánchez-Delgado, M.R. Rodríguez-Sánchez, M. Venegas. District cooling using central tower power plant. SolarPACES 2013, Las Vegas, USA. Energy Procedia 49, 1800-1809, 2014

- R. Wiesenberg, E. Serrano, A. Ruano, D. Santana, M.R. Rodríguez-Sánchez, C. Marugán-Cruz and A. Soria. PCT/ES2012/070308. Receptor Termosolar. Sun to Market Solutions SL and Universidad Carlos III de Madrid.